

Faculty of Physics and Astronomy  
Ruprecht-Karls-University Heidelberg

MASTER'S THESIS

in Physics

submitted by

**David Mazibrada**

born in Freiburg im Breisgau

February 2024



# **Development of a dc-SQUID Multiplexer for a 16×16 Metallic Magnetic Calorimeter Array**

This Master thesis was carried out by David Mazibrada  
at the Kirchhoff-Institute for Physics  
under the supervision of  
**Prof. Dr. C. Enss**



Superconducting quantum interference devices (SQUIDs) are highly sensitive flux-to-voltage converters offering a large readout bandwidth and a near quantum limit noise performance, which make them adequate candidates for the readout of metallic magnetic calorimeters (MMCs). In this thesis a flux ramp modulation (FRM) dc-SQUID multiplexing method was developed for the readout of a  $16 \times 16$  MMC array at cryogenic temperatures. The FRM multiplexing technique allows a simultaneous readout of multiple dc-SQUIDs via a single line, relaxing the requirements on the cryogenic system complexity. In comparison to a single stage flux locked loop readout the number of wires required for the detector readout with our FRM method is reduced by 85 %. New developments include two dedicated dc-SQUID FRM chip designs, which were used to fabricate the microchips in the institute's clean room. These chips are tailored to specifically fit in with the detector and its here invented readout configuration setup. Within the new method an individual flux ramp modulation signal is provided to the SQUIDs read out through a single line, adding an additional degree of freedom in operating the device compared to already existing designs. Important advancements towards the full detector readout with a FRM dc-SQUID multiplexer have been made and on top the functionality of the new FRM SQUID chips was demonstrated successfully.

### Entwicklung einer dc-SQUID Flussrampenmodulations Methode für die Auslese eines $16 \times 16$ Metallischen Magnetischen Kalorimeter Arrays

Supraleitende Quanteninterferenzdetektoren (SQUIDs) sind quantenlimitierte Fluss zu Spannungs Wandler mit einer großen Auslesebandbreite, wodurch sie sich für die Auslesung von metallischen magnetischen Kalorimetern (MMCs) eignen. Im Rahmen dieser Arbeit wurde ein dc-SQUID Multiplexer basierend auf dem Prinzip der Flussrampen-Modulation (FRM) für das Auslesen eines  $16 \times 16$  MMC-Arrays bei kryogenen Temperaturen entwickelt. Durch die frequenzcodierte gleichzeitige Auslese mehrerer dc-SQUIDs über eine einzige Leitung verringert sich die Komplexität des kryogenen Systems. Im Vergleich zu der Detektor Auslesung unter Verwendung einer Flussrückkopplungs-Methode reduziert sich mit der hier implementierten FRM-Methode die Anzahl der erforderlichen Leitungen um 85 %. Basierend auf den beiden innerhalb dieser Arbeit angefertigten dc-SQUID FRM-Chip Designs wurden entsprechende Mikrochips im institutseigenen Reinraum hergestellt. Diese Chips sind speziell auf das MMC und seine hier entwickelte Auslesekonfiguration zugeschnitten. Hierbei erhalten SQUIDs, welche über dieselbe Leitung ausgelesen werden, ein individuelles Flussrampenmodulationssignal, was im Vergleich zu bereits bestehenden Designs einen zusätzlichen Freiheitsgrad beim Betrieb bietet. Insgesamt wurden wichtige Fortschritte auf dem Weg zur vollständigen Detektorauslesung mit Hilfe eines FRM dc-SQUID Multiplexers erzielt. Darüber hinaus wurde die Funktionalität der neuen FRM SQUIDs erfolgreich demonstriert.



# Contents

<b>1</b>	<b>Introduction</b>	<b>1</b>
<b>2</b>	<b>Theoretical Background</b>	<b>3</b>
2.1	Superconductivity . . . . .	3
2.1.1	Superconducting Condensate . . . . .	3
2.1.2	Macroscopic Wavefunction . . . . .	4
2.1.3	Phase Factor of the Macroscopic Wavefunction . . . . .	6
2.2	Josephson Effect . . . . .	9
2.2.1	SIS-Junctions . . . . .	10
2.2.2	RCSJ-Model . . . . .	11
2.2.3	Short Josephson Junction in a Magnetic Field . . . . .	13
2.3	The dc-SQUID . . . . .	14
2.3.1	Self Inductance in the Zero Voltage State . . . . .	15
2.3.2	dc-SQUID Equations of Motion . . . . .	17
2.3.3	Current Sensing dc-SQUIDs . . . . .	19
2.4	Flux Ramp Multiplexing dc-SQUID Readout . . . . .	20
2.4.1	Multiplexing . . . . .	20
2.4.2	Flux Ramp Modulation . . . . .	21
2.5	SQUID Noise . . . . .	23
2.6	Thermal Considerations for a Shunted SQUID at mK-Temperatures . .	25
2.6.1	Thermal Conduction at mK-Temperatures . . . . .	26
2.6.2	Hot-electron Effect . . . . .	26
2.6.3	Thermal System of a Shunted SQUID with Cooling Fin . . . . .	28
<b>3</b>	<b>dc-SQUID Multiplexer Method, Design and Fabrication</b>	<b>31</b>

3.1	dc-SQUID Design . . . . .	32
3.2	dc-SQUID Multiplexer Chip Designs . . . . .	35
3.2.1	General layout and electrical circuit . . . . .	35
3.2.2	Type I design with thermal anchoring possibility . . . . .	36
3.2.3	Type II design with emphasis on a more spread out transmission line schema . . . . .	40
3.3	HDSQ18-Wafer series . . . . .	41
3.3.1	Fabrication . . . . .	41
<b>4</b>	<b>dc-SQUID Flux Ramp Modulation Setups</b>	<b>45</b>
4.1	Transmission Lines . . . . .	45
4.2	Room Temperature Readout Electronics . . . . .	47
4.2.1	FPGA-based dc-SQUID Flux Ramp Multiplexing . . . . .	47
4.3	Signal Processing and Data Analysis . . . . .	49
4.4	Amplifier Chain . . . . .	50
4.5	dc-SQUID Multiplexer Readout Setup . . . . .	50
4.6	Cryostat Setup for the Readout of the maXs20-256-16 . . . . .	54
<b>5</b>	<b>Experimental Results</b>	<b>63</b>
5.1	Characterization of the HDSQ18b single dc-SQUIDs . . . . .	63
5.1.1	PreVAC-Window Type Josephson Junction . . . . .	63
5.1.2	Characteristic quantities of the HDSQ18b dc-SQUIDs . . . . .	65
5.1.3	Noise of the single dc-SQUIDs at mK-temperatures . . . . .	66
5.2	White Noise vs. Temperature Comparing SQUIDs With Au and AuPd Cooling Fins . . . . .	67
5.3	HDSQ18b FRM dc-SQUID Multiplexer . . . . .	69
<b>6</b>	<b>Conclusion and Outlook</b>	<b>73</b>
	<b>Bibliography</b>	<b>75</b>

# 1. Introduction

The research field of physics will always strive for more precise methods of measurement, as the foundations of our knowledge and the validation of theories about nature are based upon measurements conducted with our instruments. Cryogenic refrigerators offer the possibility to reach temperatures near absolute zero, creating very controlled environments for high precision measurements. In order to verify e.g. aspects of quantum electrodynamics, particle detectors can be used. One prominent type of low temperature particle detectors are metallic magnetic calorimeters (MMCs), because they combine an extremely high and energy independent resolution together with a large spectral bandwidth and excellent linearity [Ens05].

An MMC consists of a particle absorber, which is thermally connected to a paramagnetic sensor, where the sensor material is gold or silver doped with a few hundred ppm of Erbium ions. The energy of the particles deposited in the absorber is proportional to the resulting rise in temperature. According to the Curie law, the magnetization of the paramagnetic material changes inversely proportional to temperature. Subsequently, the magnetization change is read out using current sensing superconducting quantum interference devices (SQUIDs). As SQUIDs have a periodic flux-to-voltage characteristics, a method to linearize the SQUID response can be desired requiring the employment of additional circuit elements. These circuits often lead to system constraints. For the readout of direct-current SQUIDs conventionally a flux-locked loop (FLL) method is implemented, where the dynamic range is limited by the finite voltage range and resolution of the digitizer. Additionally, the FLL circuit requires feedback wires routed from room temperature to each dc-SQUID and therefore to each detector, increasing the overall system complexity. Another possible way to linearize the dc-SQUID signal is the implementation of a flux ramp modulation (FRM) technique, where each dc-SQUID is operated in open-loop mode reading out the input signal as a linear phase shift of the periodic SQUID characteristics.

The developments concerning the dc-SQUID FRM multiplexer readout presented in this thesis are based on previous works [Mat08], [Ric21b], [Hoi21]. A new dc-SQUID frequency-division multiplexing method was employed to read out a novel  $16 \times 16$  MMC array [Abe25]. Additionally components for the full operation of a  $4 \times 32$  dc-SQUID flux ramp modulation multiplexing system to read out the MMC detector were conceptualized and built. In the framework of this thesis, the associated dc-SQUID FRM multiplexer chips were designed, fabricated and their functionality was demonstrated.

In the following chapter the theoretical background for this thesis is provided. First the general properties associated with superconductivity are introduced, discussing the macroscopic wave function and the behavior of its phase factor in the presence of an external magnetic field. Thereafter, on the foundation of the Josephson effect, the physics of a superconductor-insulator-superconductor Josephson tunnel junction are discussed. Subsequently, based on the already introduced concepts, the theoretical framework of the dc-SQUID is presented. In order to understand the here developed multiplex technique, the concept of the dc-SQUID flux ramp modulation readout is discussed. Also the theoretical description of white noise in dc-SQUIDs is provided, as it is necessary to interpret some experimental results obtained. At last a thermal model for a dc-SQUID was conceptualized to improve the SQUID operating temperature in future designs and to discuss our current dc-SQUID design.

In chapter 3 the new frequency division multiplexing technique, the design of the new multiplexer chips and their fabrication are discussed. The new method substitutes the rigid modulation configuration of our previous multiplexer design with a more flexible approach, where each dc-SQUID is provided with an individual flux ramp modulation signal. In the framework of this thesis two different multiplexer chip variants were composed. The chip of type I is optimized with regard to the operating temperature of the detector setup, featuring a large gold pad for thermal anchoring. Using the newly designed chip as an example, the expected SQUID operating temperatures with a simple thermal model is calculated. The chips of type II substitute the gold pad in favor of more spread out transmission lines. At last the fabrication of the dc-SQUIDs is discussed.

In chapter 4 two experimental setups for the readout of the multiplexer chips at cryogenic temperatures are showcased. The first setup is built in order to efficiently tests the multiplexer chips in a liquid helium transport dewar at a temperature of  $T = 4.2\text{ K}$ . The second setup presented here is the full maXs20-256-16 detector cryogenic readout setup, including the detector platform and arm circuit board, as well as a description of required adapters. The room temperature readout chain is identical for both setups. Additionally it has to be noted that the first setup is also cryostat compatible.

In chapter 5 experimental results surrounding this thesis are presented. To start with, the *IV*-characteristics of the first window type Josephson junction produced using our PreVAC sputtering system are investigated. Next the results obtained for the characterization of the single dc-SQUIDs produced within this thesis are summarized. Additionally the noise of these SQUIDs at mK-temperatures is discussed whereby the emphasis lies in the investigation of the temperature dependent white noise, which is compared between SQUIDs with different passive cooling structures. Finally a demonstration of the functionality of the developed multiplexer chips is presented.

## 2. Theoretical Background

In this chapter the theoretical background for this thesis is provided. First, we will have a look at superconductivity, whereby the main focus of our discussion is on the associated macroscopic wave function. Subsequently, on the basis of a macroscopic wave function, we will discuss the phenomenon of flux quantization and the Josephson effect. After that, we will discuss some aspects of the dynamics of superconductor-insulator-superconductor tunnel junctions, which are relevant in the context of this thesis. Thereupon we will discuss the basic properties of a dc-SQUID, with regards to the concepts relevant for our application. We will follow it up with the introduction of the frequency division multiplexing for dc-SQUIDs, using the flux ramp modulation technique. Next, we will look into the noise behavior of dc-SQUIDs with regards to its optimization. Finally, we will discuss low temperature heat conduction with special regard towards passive cooling techniques for SQUIDs at mK-temperatures.

### 2.1 Superconductivity

Superconductivity is a phenomenon where after cooling below a critical temperature  $T_c$  the direct current electrical resistance of a material becomes zero. Another important characteristic, discerning superconductors from ideal conductors, is the Meissner-Ochsenfeld Effect [Mei33] describing the complete expulsion of the external magnetic field from a bulk superconductor. Many elements, alloys and compounds can become superconductors [Rob76], which has opened up many possibilities for application. Our superconducting devices mainly consists of niobium, which has the highest critical temperature  $T_c = 9.25\text{ K}$  [Fin66] of all pure elements. When a material, such as Niobium, undergoes a superconducting phase transition, no visual changes occur. The lattice structure of the material is mostly unaffected while there is an obvious change in the conduction properties. Thus the observed phase transition is mainly linked to the change in nature of the electron states.

#### 2.1.1 Superconducting Condensate

A first microscopic description of superconductivity is given by the BCS-theory, named after Bardeen, Cooper and Schrieffer [Bar57]. The BCS-theory suggests that two electrons in the vicinity of the Fermi surface can form a bound state, a Cooper pair, due to an attractive interaction between the two electrons mediated by the atomic lattice. The formation of a Cooper pair lowers the energy of the system, thus

the normal state is unstable and the electrons will group in pairs and transfer energy to the external world. These Cooper pairs are the charge carriers of the supercurrent with charge  $q_s = 2e$  twice the electron charge and mass  $m_s = 2m_e$  twice the electron mass. The main argument for the occurrence of superconductivity is that the Cooper pairs are found in a coherent quantum state with macroscopic occupation of a single quantum energy state. Such a quantum state is named condensate and in the case of a superconducting condensate, this leads to a gap in the continuous electronic energy spectrum. The accurate prediction of the gap energy

$$|\Delta(0)| = 1.76k_B T_c \quad (2.1)$$

at zero temperature is the famous result of the BCS-theory. Here,  $k_B$  is the Boltzmann constant. Although not all superconductors obey the simple BCS relation, most are still well described by a Cooper pair condensate. Single fermions like electrons cannot form condensates, because of the Pauli exclusion principle. The pairing of two fermions results in a new quantum object which has similar properties to bosons. In the case of an interaction-free boson condensate, see [Ann04], we can represent the condensate with a simple macroscopic wavefunction

$$\Psi_{\text{Boson}} = \sqrt{n} e^{i\theta} \quad (2.2)$$

where  $n$  is the particle number density of Cooper pairs and  $\theta$  an arbitrary phase angle. Note that the wavefunction of this form does not represent a valid wavefunction in the context of quantum mechanics as the superposition principle no longer apply. It is therefore more to be understood as a thermodynamic variable. However, a simple interactionless boson condensate does not represent the reality of the superconducting condensate. Nevertheless, the macroscopic wavefunction of the simple form given by (2.2) is used in the field of applied superconductivity. Although one ends up with a simplified representation of real physical quantities, a nearly complete phenomenological description of a superconducting device is possible since the fundamental processes and the interaction with external forces are mainly described by the phase factor  $\theta$ .

### 2.1.2 Macroscopic Wavefunction

A more fundamental representation of the macroscopic superconducting wavefunction is

$$\Psi = \Psi_0 e^{i\theta} \quad (2.3)$$

where  $\Psi_0$  represents a real function of many properties connected to the solid body and  $\theta$  represents the phase of the superconducting condensate. In general, we can only

obtain the function  $\Psi$  under restricting simplifications and numerical calculation. However, just below the critical temperature  $T_c$ , a complete analytical expression for a macroscopic wavefunction representation of a conventional superconductor can be obtained by means of the self consistent field method introduced by Bogoljubov [Bog58] as outlined in [DG18]. The self consistent field method is a generalization of the BCS-theory which includes the treatment of an external magnetic field. First, we can solve the Bogoljubov equations for the gap energy. In the context of the microscopic theory, the energy gap is identified as the real part of the pair potential  $\Delta$ , which is in general a complex function of the solid body properties. After that we construct the free energy  $F$  of a superconductor. For a cubic crystal the perturbation of  $F$  in  $\Delta$  reads

$$F = F_N + A |\Delta|^2 + \frac{B}{2} |\Delta|^4 + C \left| \left( -i\nabla - \frac{2e\mathbf{A}}{\hbar} \right) \Delta \right|^2 + \dots \quad (2.4)$$

where  $F_N$  represents the free energy in the normal state,  $\mathbf{A}$  the magnetic vector potential, the coefficients  $A$ ,  $B$  and  $C$  result from the solved Bogoljubov equations. The three dots indicate terms of higher order, which for our discussion, we assume to be negligible.

The free energy of a superconductor near its phase transition can also be described by the phenomenological Ginzburg Landau theory [Gin50]. The central concept of this theory is, that in the vicinity of a phase transition the free energy depends on a complex order parameter  $\Psi$ , which is small near the transition point. Therefore, we can Taylor expand the free energy in powers of  $|\Psi|$ . For a cubic crystal in an external magnetic field, the perturbation of  $F$  reads

$$F = F_N + \alpha |\Psi|^2 + \frac{\beta}{2} |\Psi|^4 + \frac{1}{2m_e} |(-i\hbar\nabla - 2e\mathbf{A}) \Psi|^2 + \dots \quad (2.5)$$

where the coefficients  $\alpha$  and  $\beta$  are to be determined from experiment. The similarity between these two free energy expressions is eminent. This connection between the successful Ginzburg Landau theory of superconductivity and the microscopic theory was first made by Gorkov [Gor58], he interpreted the thermodynamic variable  $\Psi$  as the macroscopic wavefunction of a superconductor. Comparing the two expression for the free energy we immediately get

$$\Psi = \frac{\sqrt{2m_e C}}{\hbar} \Delta \quad (2.6)$$

where the pair potential  $\Delta = |\Delta| e^{i\theta}$  is given by a complex function of the solid body properties. In the context of the basic BCS-theory  $|\Delta|$  is a constant. The coefficient  $C$  can be given as [DG18]

$$C = \begin{cases} 0.017 D(E_F) \left( \frac{\hbar v_F}{k_B T_c} \right)^2 & \text{for pure metals} \\ \frac{\pi}{24} D(E_F) \frac{\hbar v_F l}{k_B T_c} & \text{for dirty metals} \end{cases} \quad (2.7)$$

where  $D(E_F)$  is the density of state of the material in the normal states at the Fermi energy  $E_F$ ,  $v_F$  is the Fermi velocity and  $l$  the electron mean free path in the normal state. Thus we are able to construct a macroscopic wavefunction from the microscopic theory. Note that there is another way of obtaining an expression for the macroscopic wavefunction from the microscopic theory following the arguments of the off-diagonal-long-range-order, introduced by Penrose [Pen60], as outlined in [Ann04]. Both approaches require a solution of the Bogoliubov equations to obtain  $\Delta$  in the presence of magnetic fields. Since our devices mostly contain niobium, it would be of interest to obtain a full wavefunction representation. However, the situation is even more complicated as niobium the BCS simplifications imposed on the solid body do not hold. A full microscopic derivation of sputtered niobium films is possible following e.g. the arguments outlined in [DG18] and microscopic assumptions fitting the description for niobium as found in [Ale03]. For the remainder of this thesis it shall be sufficient to go with a simple macroscopic wavefunction representation given by (2.3) where  $\Psi_0$  is a function of the energy gap  $|\Delta|$  we find in our niobium films.

### 2.1.3 Phase Factor of the Macroscopic Wavefunction

In the context of the microscopic theory the superconducting wavefunction described by a phase factor, is a consequence of the representation as a quantum coherent state. Another famous quantum mechanical system described by a coherent state is the laser. Therefore, one is inclined to link the existence of a coherent phase factor to the emergence of interference phenomena.

In the case of the superconducting phase factor, the connection to a magnetic field is of special interest. Looking at the vector potential  $\mathbf{A}$ , which describes the magnetic field configuration, we can introduce an arbitrary gradient field  $\chi$  that does not affect the resulting magnetic flux density  $\mathbf{B}$  as

$$\begin{aligned}\mathbf{A}' &= \mathbf{A} + \nabla\chi(\mathbf{r}) \\ \mathbf{B} &= \nabla \times \mathbf{A} = \nabla \times \mathbf{A}'\end{aligned}\tag{2.8}$$

where  $\mathbf{r}$  denotes a position. We demand that real physical measurands do not depend on the special form of our chosen potentials, meaning that our measurement of e.g. the current is not dependent on  $\chi$ . This property is also known as gauge invariance. As we will see, the complex pair potential  $\Delta$  is not gauge invariant. This is one of the central findings of the self consistent field theory and justifies the fact that a phase factor represents our system. The treatment of gauge invariance is identical for the microscopic equations from the self consistent field formalism and the macroscopic wave function, therefore, we will stick to the latter. Performing a variation calculation

of the Ginzburg-Landau equations with respect to the vector potential  $\mathbf{A}$  and the wavefunction  $\Psi$ , we directly obtain an equation for the supercurrent density

$$\mathbf{J}_s = -i \frac{\hbar q_s}{2m_s} \left( \Psi^* \nabla \Psi - \Psi \nabla \Psi^* \right) - \frac{q_s^2}{m_s} \mathbf{A} \Psi^* \Psi \quad (2.9)$$

which must satisfy gauge invariance, since it is a real physical measurand. After inserting our macroscopic wave function given by (2.3) the supercurrent density reads

$$\mathbf{J}_s = q_s \Psi_0^2 \left\{ \frac{\hbar}{m_s} \nabla \theta - \frac{q_s}{m_s} \mathbf{A} \right\} \quad . \quad (2.10)$$

In order for  $\mathbf{J}_s$  to be invariant after gauge transformation, the following condition needs to be fulfilled:

$$\theta' = \theta + \frac{q_s}{m_s} \chi(\mathbf{r}) \quad (2.11)$$

Thus, in contrast to the current density, the phase factor is not a real physical measurand, as it is not gauge invariant. The same applies to the pair potential  $\Delta$ . This gives us a connection between the phase factor of the superconductor and an external magnetic field. Another important connection between the phase factor and external magnetic field is revealed while looking at closed superconducting rings, leading to the discovery of the flux quantum.

## Flux Quantization

If a closed superconducting ring is cooled down in an external magnetic field of flux  $\Phi$ , a magnetic field  $\mathbf{H}$  is trapped inside the ring due to the screening currents expelling the magnetic field out of the bulk superconductor. A schematic depiction of a superconducting ring enclosing a magnetic field is depicted in Fig. 2.1 a). Experiments as [Goo71] have shown that the magnetic flux inside the ring after cooldown below  $T_c$  can only take certain discrete values  $\Phi = n\Phi_0$ , with integer  $n$  and

$$\Phi_0 = \frac{\hbar}{2e} = 2.07 \times 10^{-15} \text{ Tm}^2 \quad . \quad (2.12)$$

The results of the experiment conducted in [Goo71] are shown in Figure 2.1 b) where the trapped flux  $\Phi$  is plotted as a function of external magnetic flux density  $B$ . Note that the measured flux quantum indicates a charge of  $2e = q_s$ , hinting at the possibility that charge carrier in superconductors consist of electron pairs, as predicted by the BCS-theory.

The flux quantization is a consequence of the condition that the wavefunction  $\Psi$  must be a single-valued function. In the following we discuss the origin of the appearance

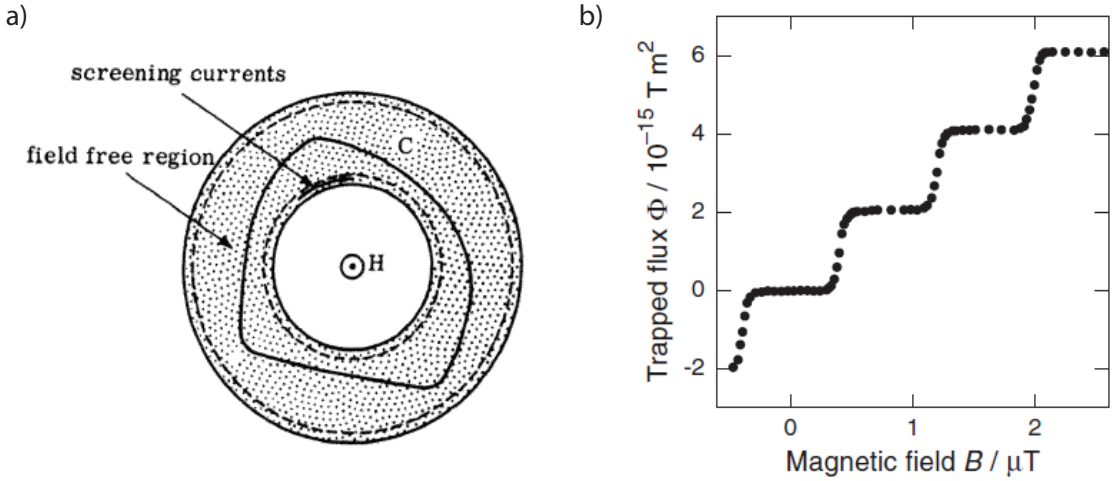


**Figure 2.1:** a) Illustration from [DG18] of a superconducting ring trapping a magnetic field  $H$ , with surface screening supercurrents. An arbitrary integration path  $C$  in a field free inner region is depicted. b) Magnetic flux trapped by a superconducting ring as a function of the magnetic field (density)  $B$  applied while cooling, of measurements conducted in [Goo71], image from [Ens05].

of the flux quantum by solving (2.10) for the charge density of a superconducting ring. Integrating the suprecurrent density  $\mathbf{J}_s$  over a closed contour  $C$  inside the superconducting ring, as e.g. indicated in Fig. 2.1 a), gives

$$\frac{m_s}{q_s^2 \Psi_0^2} \oint_C \mathbf{J}_s \cdot d\mathbf{s} = \frac{\hbar}{q_s} \oint_C \nabla \theta(\mathbf{r}) \cdot d\mathbf{s} - \oint_C \mathbf{A} . \quad (2.13)$$

In the inner regions of the bulk superconductor the suprecurrent density  $\mathbf{J}_s = 0$  vanishes, therefore the left-hand side equals zero. This effect can be measured and is predicted by the microscopic theory [DG18]. The phase  $\theta(\mathbf{r})$  is only uniquely defined in an interval of  $2\pi$ . As the contour starts and finishes at the same point and we demand a single-valued wavefunction, the integral over  $\nabla \theta(\mathbf{r})$  can only take values of  $2\pi n$  where  $n$  is an integer. The last remaining integral over the vector potential  $\mathbf{A}$  is according to Stoke's theorem the enclosed magnetic flux  $\Phi$ , therefore

$$\Phi = n \frac{\hbar}{2e} = n\Phi_0 . \quad (2.14)$$

This gives the aforementioned connection between the phase factor and the external magnetic field. A general interpretation of the phase factor is still somewhat ambiguous, as discussed in [Coo72]. In the following, we want to address the role of the phase factor within the previously hinted interference phenomena discussing the Josephson effect.

## 2.2 Josephson Effect

In this section we want to discuss the properties of a supercurrent between two superconductors with separate phase factors  $\theta_1$  and  $\theta_2$ . One way of realizing such a contact is through a superconductor-insulator-superconductor tunnel junctions (SIS-junction), where a thin insulating barrier separates a superconductor into two regions. Josephson [Jos62], [Jos64] theoretically predicted from the BCS-theory that a supercurrent can flow through a SIS tunnel junction. We are able to obtain a similar result with a static Schrödinger equation approach where we consider the overlap of two macroscopic wavefunctions. For our discussion we assume a thin insulating barrier between two identical superconductors  $S_1$  and  $S_2$ . The two respective macroscopic wavefunctions  $\Psi_1$  and  $\Psi_2$  extend outside of their respective superconducting region and overlap. The potential energy barrier introduced by the insulator separates the two superconducting regions. In consequence, the current through an SIS-junction must depend on the gauge invariant phase difference

$$\varphi = \theta_1 - \theta_2 - \frac{2\pi}{\Phi_0} \int \mathbf{A} \cdot d\mathbf{l} \quad (2.15)$$

between the two superconductors. The coupled Schrödinger equations of such a system are [Fey64]

$$i\hbar\dot{\Psi}_1 = \mu_1\Psi_1 + \kappa\Psi_2 \quad (2.16)$$

$$i\hbar\dot{\Psi}_2 = \mu_2\Psi_2 + \kappa\Psi_1 \quad (2.17)$$

where  $\kappa$  is the coupling constant,  $\mu_1$  and  $\mu_2$  the chemical potential of the respective superconducting region. Solving above system of coupled Schrödinger equations we find two equations known as Josephson equations, which depend mainly on the phase difference  $\varphi$  between the two superconductors:

$$I_S = I_c \sin(\varphi) \quad (2.18)$$

$$\varphi(t) = \frac{2\pi}{\Phi_0} Vt \quad (2.19)$$

where  $V$  is the voltage drop across the junction and  $I_S$  the supercurrent limited by the junction specific critical current  $I_c$ . From the Josephson equations we can infer the behavior of the tunneling supercurrent.

For a constant phase difference  $\varphi$  the Josephson equations (2.18) and (2.19) predict a constant dissipationless supercurrent and zero voltage across the junction. This is referred to as *Josephson direct current effect* or zero voltage state. In order to attain this state, two conditions have to be met. First, we must apply an external generator which supplies the junction with a current  $I < I_c$  below the critical current. The phase difference  $\varphi$  will adjust itself such that exactly the externally applied current

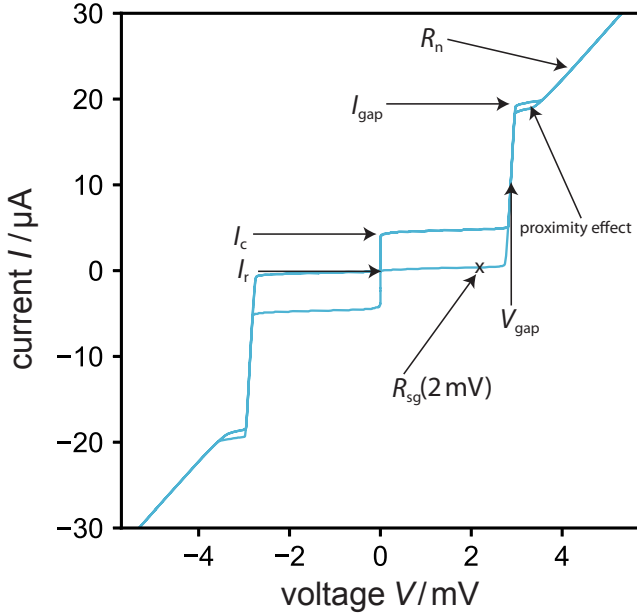


**Figure 2.2:** Hysteretic  $IV$ -characteristics of an underdamped window-type Josephson junction fabricated and measured within the framework of this thesis. Various quality parameters that can be extracted from the  $IV$  - curve are denoted here.

$I$  runs through the junction. Second, there must be no external magnetic flux or other external disturbances.

If the phase difference  $\varphi(t)$  changes with time we measure a voltage  $V$  across the junction as we can deduce from (2.19). In turn, from (2.18) we can predict an alternating current with frequency  $\omega_J = (2\pi/\Phi_0)V$ . This is referred to as the *Josephson alternating current effect* or as voltage state. As the current  $I$ , exceeds the critical current  $I_c$ , the current constitutes of supercurrent and an additional quasiparticle current channel. The quasiparticles are normal conducting charge carriers consisting of a superposition of electron hole pairs found in the superconductor, for reference see e.g. [Ens05]. The tunneling of quasiparticles is a dissipative process and in turn the voltage across the junction can be understood according to Ohm's law  $V = R_N I_q$  with the quasiparticle current  $I_q$  which runs trough the junction with resistance  $R_N$ .

### 2.2.1 SIS-Junctions

Within the framework of this thesis we used  $\text{Nb}/\text{Al-AlO}_x/\text{Nb}$  junctions, where aluminum oxide forms the insulating barrier. In Fig. 2.2 a typical hysteretic junction current voltage ( $IV$ -) characteristics of a junction is shown, which was produced within the scope of this thesis and measured with experimental setup described in [Geh23]. Successively increasing the current from  $I = 0$  no voltage is measured across the junction as long as  $I < I_c$ . If the current exceeds the critical current  $I > I_c$  we measure a voltage, which coincides with the expected gap energy voltage  $V_{\text{gap}} = 2|\Delta|/e$  of the Cooper pairs. Consequently, the current is carried by an additional quasipar-

ticle channel with a normal resistive component with resistance  $R_N$ , which can be obtained from the slope of the ohmic part of the  $IV$ -characteristics. Right before the ohmic part of the characteristics start, an additional artifact appears, which is called proximity effect [McM68] caused by the normal conducting aluminium adjacent to the tunnel contact. Successively decreasing the current again, the zero voltage state with a return current  $I_r \leq I_c$  is reached. However, before reaching the return current, a voltage across the junction given by a small current of thermally excited quasi particles can be measured, which at first glance is not expected looking at the Josephson equations (2.18) and (2.19). This hysteretic behavior stems from the fact that real junctions are three dimensional. Thus we need a model considering these additional effects, which the RCSJ-model offers, for reference see e.g. [Cla04].

### 2.2.2 RCSJ-Model

A complete dynamic description of a real Josephson junction is not possible today, therefore we use the simplifying resistive capacitive shunted junction model, in short RCSJ-model. Within the framework of this model, a Jospehson tunnel junction is considered as a parallel circuit, as depicted in Fig. 2.3 a). It is constituted of an ideal lumped element junction described by the Josephson equations (2.18) and (2.19), a resistive current channel  $I_n$  due to quasiparticle tunneling, a capacitance and subsequent displacement current channel  $I_D$ . Since a tunnel junction can be approximately seen as a parallel plate capacitor  $C = \varepsilon_0 \varepsilon_r A/d$  with area  $A$  and distance  $d$  and a noise current channel  $I_F$ . Accordingly, the total current from all these channels is given by the sum of each individual channel

$$\begin{aligned} I &= I_s + I_n + I_D + I_F \\ &= I_c \sin(\varphi) + \frac{1}{R} \frac{\Phi_0}{2\pi} \frac{d\varphi}{dt} + C \frac{\Phi_0}{2\pi} \frac{d^2\varphi}{dt^2} + I_F \quad . \end{aligned} \quad (2.20)$$

The system can be described by a tilted washboard potential of the form

$$E_{\text{pot}} = E_0 [1 - \cos(\varphi) - i\varphi + i_F \varphi] \quad (2.21)$$

given in units of normalized currents  $i = I/I_c$  and the Josephson energy  $E_0 = \hbar I_c / 2e$ . Using this potential we can rewrite (2.20) to

$$\left( \frac{\Phi_0}{2\pi} \right)^2 C \ddot{\varphi} + \left( \frac{\Phi_0}{2\pi} \right)^2 \frac{1}{R} \dot{\varphi} + \frac{\partial E_{\text{pot}}}{\partial \varphi} = 0 \quad . \quad (2.22)$$

This equation is mathematically equivalent to the equation of motion

$$M \ddot{\varphi} + \eta \dot{\varphi} + \nabla E_{\text{pot}} = 0 \quad (2.23)$$

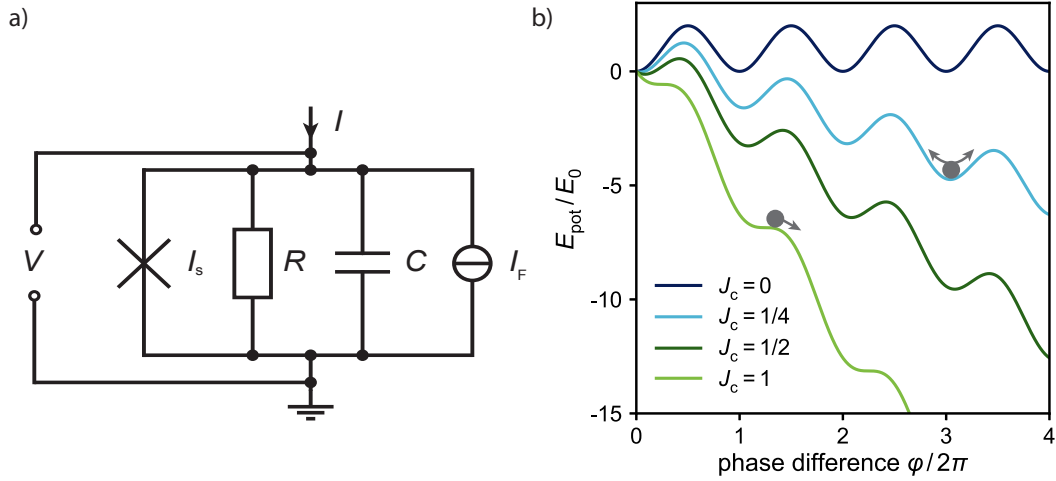


**Figure 2.3:** a) Effective circuit of a Josephson junction, as assumed in the RCSJ model. b) The normalized energy potential  $E_{\text{pot}}/E_0$  is plotted against the phase difference for different values of the normalized current density  $J_c$ . In analogy to a mechanical system the two gray points depict particles in the potential, whereby the arrows indicate the expected dynamics.

of a phase particle moving through a tilted washboard potential  $E_{\text{pot}}$  with mass  $M = C(\Phi_0/2\pi)^2$  and friction coefficient  $\eta = (1/R)(\Phi_0/2\pi)^2$ . With the analogy of a particle rolling down a tilted washboard potential one can derive the qualitative behavior of the  $IV$ -characteristics of a junction. A change in current leads to a change in tilt of the potential and deformation of the potential wells, as illustrated in Figure 2.3 b). Increasing the current from  $i = 0$  the phase particle is bound in a local potential minimum if  $i < 1$ , where the particle is expected to oscillate with the plasma frequency  $\omega_p$  around the potential minimum such that the mean time evolution of the phase difference  $\langle \dot{\phi} \rangle$  is zero. Hence no voltage is measured until  $i > 1$  where the phase particle is not bound by a local potential minimum anymore, figuratively speaking the particle is rolling down the washboard potential, thus the mean time evolution  $\langle \dot{\phi} \rangle \neq 0$ . Decreasing the current again, the kinetic energy of the phase particle can exceed the potential energy barrier to where it was previously bound to, if the friction coefficient is small, leading to a return current which satisfies  $i_r < 1$ . The relationship between mass and friction coefficient can be represented by the Stewart-McCumber parameter

$$\beta_C = \frac{2\pi}{\Phi_0} I_C R_N^2 C \quad (2.24)$$

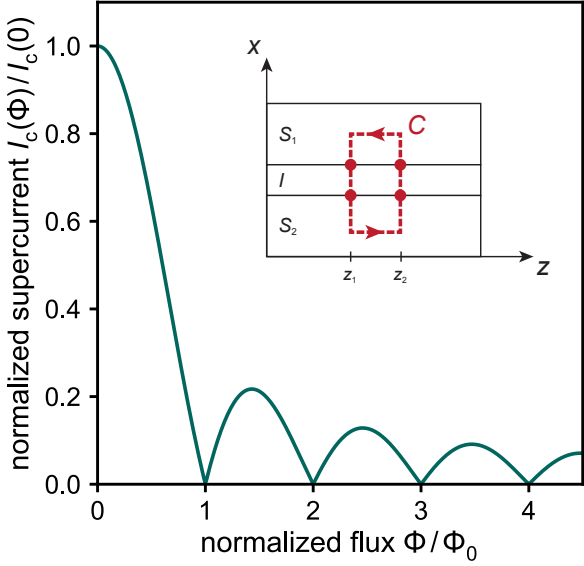


**Figure 2.4:** Normalized maximal supercurrent plotted against the normalized flux. It vanishes at integer flux quanta and shows local maxima for half-integer flux quanta. The inset shows a cross section of a SIS-junction in magnetic field  $H$  in the  $xz$ -plane.  $S_1$  and  $S_2$  indicate superconducting regions and  $I$  an insulator. A closed integration path transversing the junction at two different positions  $z_1$  and  $z_2$  is indicated in red.

effectively describing the damping factor of the junction. For  $\beta_C \ll 1$  the Josephson junction is strongly damped, such that  $i_r = 1$  and no hysteresis occurs. For  $\beta_C \gg 1$  the return current [Lik86] is given as

$$i_r = \frac{4}{\pi R} \sqrt{\frac{\Phi_0}{2\pi C I_c}} = \frac{4}{\pi \sqrt{\beta_c}} \quad (2.25)$$

which describes a hysteretic  $IV$ -characteristics of a junction shown in Figure 2.2.

### 2.2.3 Short Josephson Junction in a Magnetic Field

In a superconductor the external magnetic field penetrates the surface only with a small penetration depth  $\lambda$  as can be derived from the microscopic equation [DG18] and seen in many experiments, e.g. for thin niobium films [Gub05]. Applying a magnetic field through the junction will result in a total magnetic penetration of  $t_B = d + 2\lambda$  with  $d$  the junction thickness. A Josephson junction is classified as short if the side length of the contact is shorter than the Josephson penetration depth [Wei69]

$$\lambda_J = \sqrt{\frac{\Phi_0}{2\pi\mu_0 J_c t_B}} \quad (2.26)$$

where  $J_c = I_c/A$  is the critical current density of a Josephson contact of area  $A$ . The junctions used in this thesis can all be classified as short Josephson junctions. For short junctions the self field is neglected as the external magnetic field in experiments far exceeds it [Wei69]. The phase difference of the two superconductors  $\varphi$  measured

along the three dimensional junction depends on position and external magnetic field. In order to verify this, we can integrate along a closed contour inside the junction, as illustrated in the inset of Fig. 2.4 with a magnetic flux density  $B$ , which is perpendicular to the current flowing across the junction. The position dependent phase difference is then given by [Jos74]

$$\varphi(z) = \frac{2\pi}{\Phi_0} B z t_B + \varphi_0 \quad (2.27)$$

where  $z$  denotes the position in direction as indicated in Fig. 2.4 and  $\varphi_0$  is the phase difference at  $z = 0$ . The consequential maximum supercurrent through the junction, which depends on external flux, is obtained by means of Fourier transformation of the current density (2.18). Utilizing the phase relation (2.27) and setting the integral boundaries representing the junction geometry the maximum supercurrent is given as:

$$I_c(\Phi) = I_c \left| \frac{\sin(\pi\Phi/\Phi_0)}{\pi\Phi/\Phi_0} \right| \quad (2.28)$$

The resulting interference pattern is shown in Fig. 2.4 where the normalized critical supercurrent  $I/I_c$  is plotted against normalized the magnetic flux  $\Phi/\Phi_0$ . This resulting interference pattern is similar to the Fraunhofer pattern obtained when two coherent light waves interfere through a single slit. As magnetic flux inside the junction area is not quantized, it even enables the measurement of nonquantized flux by utilizing this interference effect.

## 2.3 The dc-SQUID

We are now able to discuss direct current Superconducting Quantum Interference Devices (dc-SQUIDs), which are magnetic flux to voltage converters. They combine the flux quantization in superconducting loops with the Josephson effect and are among the most sensitive detectors for magnetic flux. A detailed phenomenological description of SQUIDs can be found in [Cla04], [Tes77]. In Fig. 2.5 the basic schematic of a dc-SQUID is shown. A superconducting loop, we shall refer to as SQUID-loop, is interrupted by two SIS-junctions with a respective maximum supercurrent of  $I_{c1}$  and  $I_{c2}$ . Each junction is shunted with a resistance  $R_S$  connected in parallel providing an additional current channel for the quasiparticles when the bias current exceeds the combined critical current of the junctions  $I_b > (I_{c1} + I_{c2})$ . This suppresses the hysteretic behavior of the junctions as the shunt resistance is chosen much smaller than the resistance of the junction. In turn, the main channel for the quasiparticle current are the shunt resistors. However, they lead to excess noise and heating, which we will address in section 2.5. The dc-SQUIDs are operated in either a current bias or

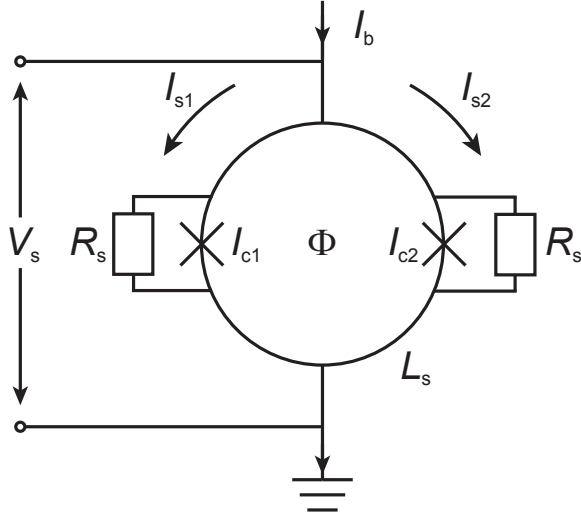


**Figure 2.5:** Sketch of a dc-SQUID. A superconducting ring is interrupted by two Josephson junctions connected in parallel. The SQUID-loop has an inductance  $L_s$  and houses a magnetic flux  $\Phi$ . A bias current  $I_b$  is applied while the voltage drop  $V_s$  is measured. Additionally shunt resistors with resistance  $R_s$  are connected in parallel to the junctions to avoid a hysteretic behaviour in the  $IV$ -characteristics.

in voltage bias. In the following we will only discuss the current bias application, as the SQUIDs used in this thesis are exclusively operated with a current bias. Here, the SQUID is biased with a current  $I_b$  via an external generator and thus only the voltage  $V$  changes with the magnetic flux  $\Phi_s$  enclosed in the SQUID-loop. The SQUID-loop and the resulting self-inductance plays a major role for the sensitivity of the device. Henceforth we will discuss the influence of the self-inductance of a dc-SQUID in the voltage-free state.

### 2.3.1 Self Inductance in the Zero Voltage State

The current of two identical junctions in parallel in the zero voltage stage is given by the sum of the respective current-phase relations

$$I_s = I_c \sin(\varphi_1) + I_c \sin(\varphi_2) \quad (2.29)$$

$$= 2I_c \cos\left(\pi \frac{\Phi}{\Phi_0}\right) \sin\left(\varphi_1 + \pi \frac{\Phi}{\Phi_0}\right) \quad (2.30)$$

where  $\varphi_1$  and  $\varphi_2$  are the phase differences of the wavefunction of the superconducting electrodes at the respective junction. The magnetic flux inside the SQUID is not only given by the external magnetic flux but also from the self induced flux. The total flux inside the SQUID-loop is

$$\Phi = \Phi_{\text{ext}} + LI_{\text{cir}} \quad (2.31)$$

where  $I_{\text{cir}}$  is the circular current inside the SQUID-loop and  $L$  the inductance of the SQUID-loop. According to Kirchhoff's law, the circular current  $I_{\text{cir}} = (I_{s1} - I_{s2})/2$

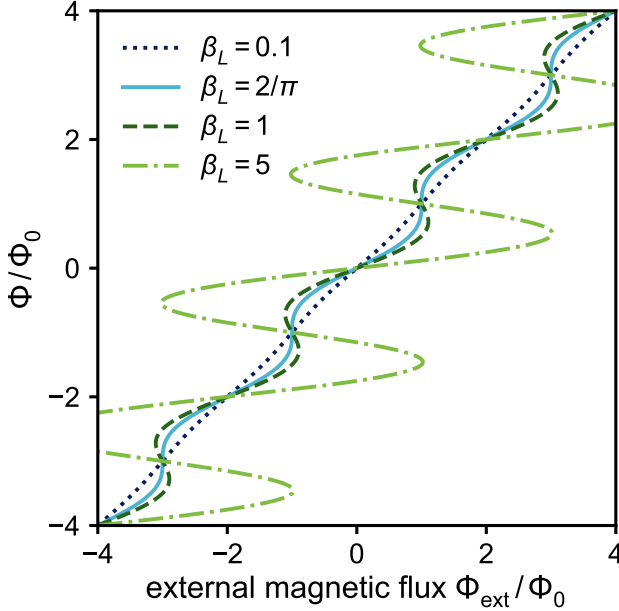


**Figure 2.6:** Total magnetic flux  $\Phi$  threading the SQUID loop plotted against the externally applied flux  $\Phi_{\text{ext}}$  for different values of the screening parameter  $\beta_L$ . Hysteretic behaviour appears for  $\beta_L > 2/\pi$ .

is given by half of the difference between the currents in the two superconducting branches. Inserting the first Josephson equation (2.18), the expression for the circular current gives:

$$I_{\text{cir}} = I_c \sin\left(\pi \frac{\Phi}{\Phi_0}\right) \cos\left(\varphi_1 + \pi \frac{\Phi}{\Phi_0}\right) \quad (2.32)$$

For small currents  $I_s \ll I_c$ , or more precisely stated, if  $\sin(\varphi_1) \approx -\sin(\varphi_2)$  we can rewrite 2.31 into

$$\Phi = \Phi_{\text{ext}} - \frac{\Phi_0 \beta_L}{2} \sin\left(\pi \frac{\Phi}{\Phi_0}\right) \quad (2.33)$$

where we introduced the screening parameter

$$\beta_L = \frac{2LI_c}{\Phi_0} \quad . \quad (2.34)$$

In Fig. 2.6 the normalized magnetic flux  $\Phi/\Phi_0$  inside the loop is depicted as a function of the normalized external flux  $\Phi_{\text{ext}}/\Phi_0$ , whereby a set of functions, modeled after (2.33), is plotted for different screening parameters  $\beta_L$ . At the nodes of the graph, when the flux is a multiple of the flux quantum  $\Phi_{\text{ext}} = n\Phi_0$ , the circular current  $I_{\text{cir}}$  vanishes. One important observation is that if  $\beta_L > 2/\pi$ , the actual magnetic flux inside the loop is not unique with external flux. Therefore, it is apparent that the screening parameter should be small, as bigger screening parameters  $\beta_L \gg 1$  lead to ambiguity. In addition, bigger screening parameters will leave the SQUID insensitive to external flux as the self induced flux dominates inside the SQUID loop. However, as the SQUID-loop needs to inductively couple to an external magnetic

field it is beneficial to have an as high as possible loop self inductance to ensure a good magnetic coupling, which improves the signal to noise ratio. Therefore, the SQUID-loop inductance needs to be engineered for the upfront application.

### 2.3.2 dc-SQUID Equations of Motion

In the nonzero voltage stage the quasiparticle current contribution allows a flux dependent voltage measurement. Applying Kirchhoff's law to the dc-SQUID circuit and considering the RSCJ model for the junctions, we find the Langevin equations of motion for a shunted dc-SQUID:

$$\frac{I}{2} - I_{\text{cir}} = (1 - \alpha_C) \frac{\hbar C}{q_s} \frac{d^2\varphi_1}{dt^2} + (1 - \alpha_R) \frac{\hbar}{q_s R} \frac{d\varphi_1}{dt} + (1 - \alpha_I) I_c \sin \varphi_1 + I_{F1} \quad (2.35)$$

$$\frac{I}{2} + I_{\text{cir}} = (1 - \alpha_C) \frac{\hbar C}{q_s} \frac{d^2\varphi_2}{dt^2} + (1 - \alpha_R) \frac{\hbar}{q_s R} \frac{d\varphi_2}{dt} + (1 - \alpha_I) I_c \sin \varphi_2 + I_{F2} \quad (2.36)$$

and

$$\varphi_2 - \varphi_1 = 2\pi \left( \frac{\Phi_{\text{ext}}}{\Phi_0} + \frac{\beta_L I_{\text{cir}}}{2} \right) \quad (2.37)$$

Here,  $I$  is the applied current,  $\varphi_i$  is the phase difference at the respective junction,  $\alpha$  the asymmetry factor in respective quantity denoted by the index,  $R = R_S R_N / (R_S + R_N)$  the total resistance composed of the junction normal resistance  $R_N$  and shunt resistance  $R_S$  and  $I_{F1}, I_{F2}$  denoting the fluctuation current in each branch. For bias currents larger than  $2I_c$  and perfectly symmetric SQUIDs, we always obtain a flux to voltage characteristics periodic in  $\Phi_0$ . Following similar equations, the same behavior was deduced in [Tes77].

## Characteristic Curves of dc-SQUIDs

A dc-SQUID operated in current bias can be classified by just two different characteristics. One is the  $IV$ -characteristics describing the mean voltage dependence with the applied bias current for a constant external magnetic flux  $\Phi_{\text{ext}}$  threading the SQUID-loop. Usually two limiting curves corresponding to  $\Phi_{\text{ext}} = (n + 1/2)\Phi_0$  and  $\Phi_{\text{ext}} = n\Phi_0$ , with integer  $n$ , are obtained while all other curves for a different magnetic flux lie inbetween. The  $IV$ -characteristic in the case of  $\beta_L \ll 1$  and  $\beta_C \ll 1$  is shown in Fig. 2.7.

For dc-SQUID operation the external magnetic flux is not constant and for an input exceeding  $\Phi_0$  will result in periodic  $V\Phi$ -characteristics. In current bias operation the bias current is kept constant. The resulting periodic characteristics are shown in Fig. 2.7 b). The amplitude of the periodic signal is given by the voltage difference

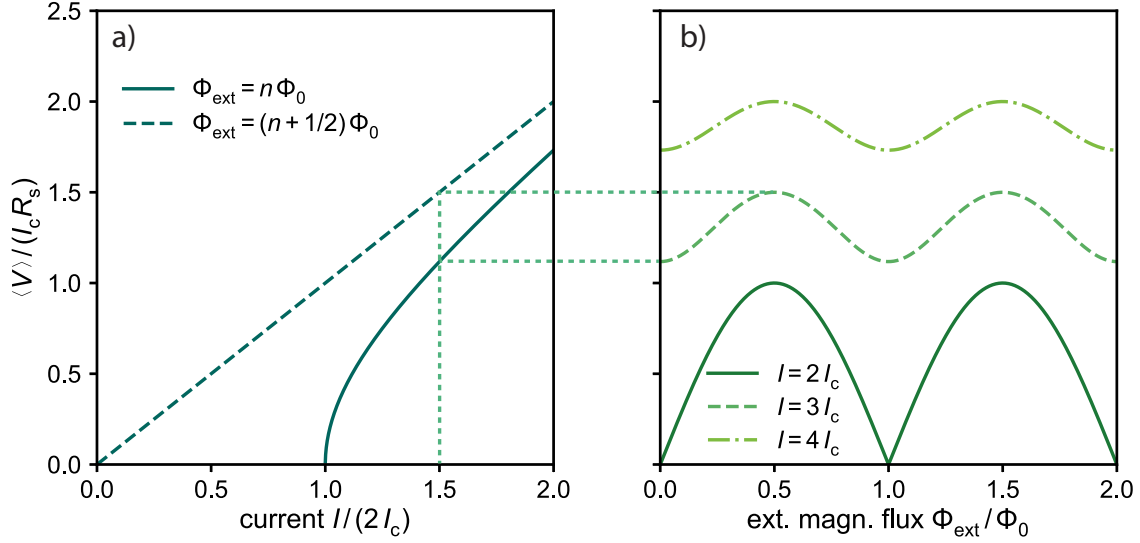


**Figure 2.7:** a)  $IV$ -characteristics of a dc-SQUID in the limiting case of  $\beta_L = 2LI_c/\Phi_0 \ll 1$  and  $\beta_C = 2\pi I_c R_N^2 C/\Phi_0 \ll 1$  for  $\Phi_{\text{ext}} = n\Phi_0$  and  $\Phi_{\text{ext}} = (n + 1/2)\Phi_0$ . b) Shows corresponding  $V\Phi$ -characteristics of the dc-SQUID.

between the two limiting curves of the  $IV$ -characteristic. It is apparent that for a sensor application the flux to voltage transfer coefficient  $V_\Phi = (\partial V / \partial \Phi)$ , describing the partial derivative of  $V$  with respect to  $\Phi$ , should be maximized. A SQUID in open loop application refers to a SQUID which is not biased at a particular working point of the  $V\Phi$ -characteristics. For such a operation the mean  $\langle V_\Phi \rangle$  should be maximized to enhance the sensitivity. After numerical simulations [Tes77] the mean flux to voltage transfer coefficient is approximated with

$$\langle V_\Phi \rangle \approx \frac{I_c R_s}{(1 + \beta_L)} . \quad (2.38)$$

Generally, the behavior of a SQUID must be modeled numerically to obtain a full insight into the expected  $V_\Phi$ . In some cases, the SQUID-loop is additionally shunted with a resistance  $R_L$  in parallel to the Josephson junctions to dampen resonances [Enp91, Enp92b, Enp92a]. Then the expected voltage swing  $V$  [Enp85], [Tar99] can be expressed as

$$\Delta V = \frac{7}{\pi^2} \frac{I_c R_s}{1 + \frac{\beta_L}{\sqrt{1 + (\frac{R_s}{R_L} \beta_L)^2}}} \left[ 1 - 3.57 \frac{\sqrt{k_B T L_s}}{\Phi_0} \right] . \quad (2.39)$$

### Asymmetric Bias Current Injection

The dc-SQUIDs produced within the framework of this thesis have a asymmetric bias current injection, meaning that the two parallel SQUID-halfflops have maximal

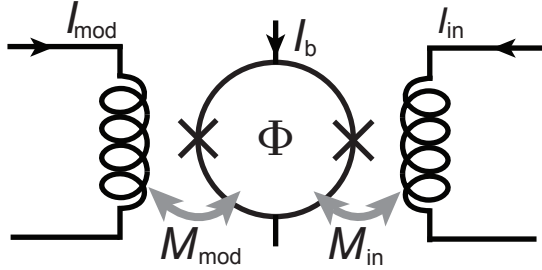


**Figure 2.8:** Schematic of a current sensing dc-SQUID with two coil configuration. One input coil with mutual inductance  $M_{\text{in}}$  and a modulation coil with mutual inductance  $M_{\text{mod}}$  to the SQUID-loop.

different inductances. In our equations of motions (2.37), (2.35) and (2.36) this is reflected by altering  $I_{\text{circ}}$  according to the inductance values of the two branches. As the current is asymmetrically distributed across the SQUID branches we expect the  $I\Phi$ -characteristic of one flank to be steeper while the other flattens. The advantage of asymmetric bias current injection is that there is a much smaller shift in the  $V\Phi$ -characteristic with fluctuations in the operating current [Ueh93]. This renders the voltage measurement more insensitive to fluctuations of the bias current. Further discussion of asymmetric bias current injection can be found in [Mul01].

### 2.3.3 Current Sensing dc-SQUIDs

For a MMC readout application, we use current sensing dc-SQUIDs with a two-coil configuration as shown in Fig. 2.8. To measure a current  $I_{\text{in}}$  with a dc-SQUID it needs to be converted to magnetic flux, wherefore an input coil couples inductively to the SQUID loop. In general, the mutual inductance between two coils is given by

$$M = k\sqrt{L_1 L_2} \quad (2.40)$$

where  $k$  is the coupling constant between the two coils with inductance  $L_1$ ,  $L_2$  respectively. An input coil couples to the SQUID-loop with mutual inductance  $M_{\text{in}}$  and the modulation coil with mutual inductance  $M_{\text{mod}}$ . The modulation coil is used to additionally apply a controlled magnetic flux into the SQUID-loop. This allows for a controlled manipulation of magnetic flux inside the SQUID-loop enabling e.g. a flux locked loop (FLL) operation where the flux inside the SQUID-loop is kept constant as the modulation coil exactly cancels the magnetic flux from the input coil. In this thesis we aim for an open loop application, whereby a current ramp signal is applied to the modulation coil, such that the magnetic flux inside the SQUID loop changes at a constant rate. Measuring the voltage across the SQUID over time, the periodic  $V\Phi$ -characteristics, as shown in the previous section, are obtained. As the two external coils couple to the same SQUID loop, we expect parasitic effects, like cross-talk. Cross-talk in general refers to the disturbance caused by electric or magnetic fields in a signal between separated current channels. The two coils do not only couple into the SQUID loop, but also couple with each other with an unwanted

parasitic mutual inductance  $\delta M_{\text{par}}$ . Further, for a practical SQUID we expect parasitic resonances, due to resistances, parasitic capacitances and inductances forming *RLC*-circuits. The resonances depend on the geometric realization and material of the coils, temperature and geometry of the junctions [Enp91, Enp92b, Enp92a]. In a real application, it can be necessary to damp or to shift the resonance frequencies to ensure a smooth operation of the devices. Therefore additional filter elements are included into a practical SQUID design. A more detailed discussion of our typical current sensing SQUID design including implemented filter is found in [Bau22] and [Kah24].

## 2.4 Flux Ramp Multiplexing dc-SQUID Readout

### 2.4.1 Multiplexing

Due to the continuous increase in complexity and requirements of various cryogenic experiments, an ever increasing number of SQUIDs is required. As a result, the cabling and readout electronics expense scale linearly with the number of SQUIDs if read out individually. In order to relax the cryogenic system complexity, multiplex techniques can be applied. These are common e.g. in telecommunications and other high-frequency electronics applications [Wei71]. Multiplexing describes an interleaving of the signals of individual carriers, so that the electronically interleaved information can be transmitted bundled within a single transmission line. There are several types of multiplex techniques where each has its own individual strength.

**Room Multiplexing** Each signal is transmitted individually.

**Time Multiplexing** The single channels are individually delayed and then transmitted through a common transmission line. For this purpose, the transmission channel of each signal source is provided exclusively for a time window  $\Delta t$  in turn.

**Frequency Multiplexing** Simultaneous transmission of all channels, where each channel has non-overlapping frequency ranges.

**Code Multiplexing** The individual signals are decoded with different bit patterns.

Based on our prior developments [Kem12], [Ric21b] and [Hoi21] of a frequency division dc-SQUID multiplexing technique we decided to work towards a full frequency division dc-SQUID multiplex readout for the maXs20-256-16 16×16 MMC detector array [Abe25]. In the past many different frequency multiplex techniques were developed for the readout of low temperature particle detectors using rf-SQUIDs [Cla04],

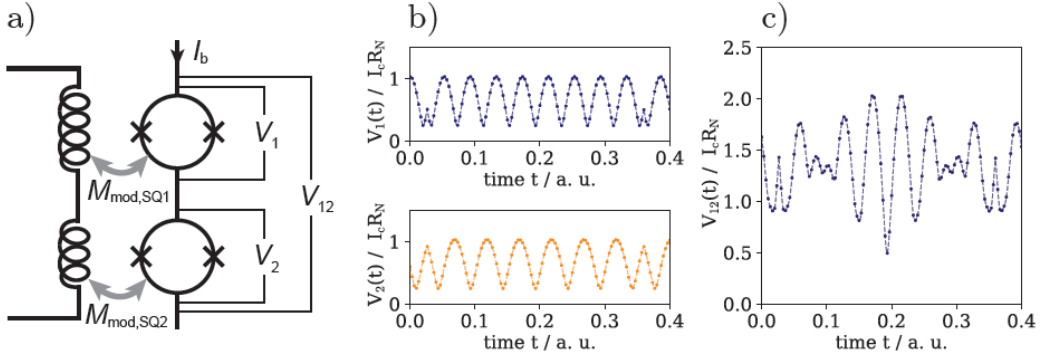


**Figure 2.9:** a) Schematic of 2 frequency modulated dc-SQUIDS read out with single channel readout  $V_1$ ,  $V_2$  and simultaneously readout  $V_{12}$ . Both SQUIDS are operated in open loop while a common flux ramp is applied through the modulation coils. Here the SQUIDS modulate with different frequency as the mutual inductances  $M_{\text{mod},\text{SQ}1}$  and  $M_{\text{mod},\text{SQ}2}$  differ and therefore a different flux  $\Phi_1$  and  $\Phi_2$  is enclosed. b)  $V_1$  and  $V_2$  are plotted against time in a time window between two flux ramp resets. c) The combined voltage signal  $V_{12}$  plotted against time. Figure adopted from [Hoi21].

which are coupled to superconducting resonators [Irw06], [Mat08], which were also extensively developed within our group [Kem15], [Weg18] and most recently [Ahr22]. Our frequency division dc-SQUID multiplexing approach allows for a simultaneous readout of the detector pixels. In contrast to rf-SQUIDS the more robust dc-SQUIDS do not require the same scale of complex and fast readout electronics. In our group we demonstrated high possible bandwidth [Ric21a] for dc-SQUIDS in multiplex application. This multiplexing approach bridges the gap between demanding multiplexing methods and simple FLL based individual channel readout of medium-scale cryogenic detector arrays. Whereas code-division multiplexing and time-division multiplexing techniques offer similar benefits, a frequency modulated approach additionally offers the possibility of a simultaneous readout of all detector channels, significantly increasing the readout efficiency in comparison to the other methods [Kem12]. In order to readout the SQUIDS with a frequency multiplexing technique we employ a flux ramp modulation readout technique based on the ideas described in [Mat12].

#### 2.4.2 Flux Ramp Modulation

With the use of the flux ramp modulation technique it is possible to read out multiple SQUIDS through a single voltage measurement. An illustrative flux ramp modulation circuit is presented in Fig. 2.9 a). With flux ramp modulation each SQUID is modulated by an individual current ramp signal with modulation frequency  $f_{\text{mod}}$  over a modulation coil, which is inductively coupled to the SQUID-loop. In the framework

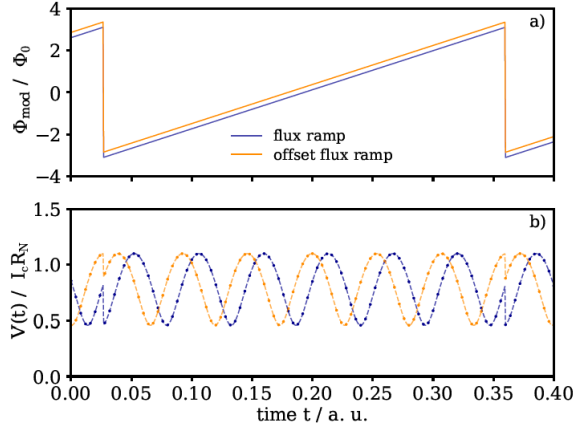


**Figure 2.10:** Depiction of the theoretically expected constant phase shift of the SQUID characteristics. a) The orange ramp possess a constant flux offset, which b) shifts the SQUID characteristics by a constant phase corresponding to the offset. Figure adopted from [Hoi21].

of this thesis a current ramp  $I_{\text{mod}}$  is provided by a periodic sawtooth shaped signal, generating consecutively linear ramp segments. The magnetic flux induced into a SQUID-loop through the modulation coil with mutual inductance  $M$  is given by

$$\Phi_{\text{mod}}(t) = MI_{\text{mod}}(t) \quad . \quad (2.41)$$

The ramp signal sweeps trough multiple flux quanta with a constant rate, resulting in a periodically modulated signal. This is depicted by the  $V\Phi$ -characteristics in 2.9 b) where the expected voltage response  $V_1$  and  $V_2$  after (2.19) over single SQUID is plotted against time of the single channels which lie inbetween two ramp resets. The combined signal  $V_{12}$  is shown in Fig. 2.9 c) from which, by means of a Fourier transformation, the frequency response from  $V_1$  and  $V_2$  can be obtained. Provided that the magnetic flux induced in the individual SQUID-loops differs from one another the response frequency  $f$  of the SQUID signals will differ as a consequence. Therefore it is possible to distinguish the response of the individual SQUIDs, which allows the readout through a single transmission line.

Given that the flux  $\Phi_{\text{mod}}$  provided through an input coil as schematically depicted in Fig. 2.8 changes slowly in comparison to  $\Phi_{\text{mod}}$  the external flux appears as a constant phase offset shifting the periodic  $V\Phi$ -characteristics by [Mat12]

$$\Delta\varphi = 2\pi \frac{\Phi}{\Phi_0} \quad . \quad (2.42)$$

In Fig. 2.10, the theoretically expected constant phase shift in the SQUID  $V\Phi$ -characteristics is shown, when an offset in the flux ramp is applied. By continuously measuring the SQUID characteristics and tracking the phase we are thus able to measure the external magnetic flux  $\Phi_{\text{in}}$ . The method of phase determination is discussed in [Hoi21]. Since the phase shift  $\Delta\varphi$  is a linear function of the applied magnetic flux according to (2.42), the SQUID readout is linearized. The sampling frequency of the SQUID readout corresponds to the frequency of the sawtooth flux ramp modulation

$f_{\text{mod}}$  signal. The carrier frequency of periodic SQUID  $V\Phi$ -characteristics is in turn given as

$$f_c = f_{\text{mod}} \frac{\Phi_{\text{mod,max}}}{\Phi_0} \quad (2.43)$$

where  $\Phi_{\text{mod,max}}$  is the total flux enclosed in the SQUID-loop corresponding to one ramp period.

## 2.5 SQUID Noise

The noise of a SQUID device is usually denoted with a power spectral density  $S$ , which derivation we will shortly discuss, for reference see e.g. [Mot93]. The frequency components of a signal  $x(t)$  can be obtained via a Fourier transformation

$$\tilde{x}(f) = \int_0^T x(t) e^{-i2\pi t f} dt \quad (2.44)$$

where  $T$  denotes the total measurement time of the signal. The average power  $P$  of the signal is given according to Parseval's theorem with

$$P = \lim_{T \rightarrow \infty} \frac{1}{T} \int_{-T/2}^{T/2} |\tilde{x}(f)|^2 df \quad . \quad (2.45)$$

For a more simple mathematical procedure an alternative representation of the average power, where  $x_T(t) = x(t)\omega_T(t)$  and  $\omega_T(t)$  is unity within the measurement period and zero elsewhere, is introduced

$$P = \lim_{T \rightarrow \infty} \frac{1}{T} \int_{-\infty}^{\infty} |\tilde{x}_T(f)|^2 df \quad . \quad (2.46)$$

The power spectral density of the signal  $x$  is defined as the integrant above

$$S_x(f) = \lim_{T \rightarrow \infty} \frac{1}{T} |\tilde{x}_T(f)|^2 \quad . \quad (2.47)$$

In practice, we replace the limit in time  $T \rightarrow \infty$  with a limit in number of measurements  $N \rightarrow \infty$ , each with a finite measurement time  $T$ , so that

$$S_x(f) = \lim_{N \rightarrow \infty} \frac{1}{NT} \sum_j^N |\tilde{x}_{T,j}(f)|^2 \quad (2.48)$$

where we assumed our time traces to be ergodic. For a SQUID, the common representation of noise is given by the square root of the power spectral density flux noise

$$\sqrt{S_\Phi} = \frac{\sqrt{S_V}}{V_\Phi^2} \quad (2.49)$$

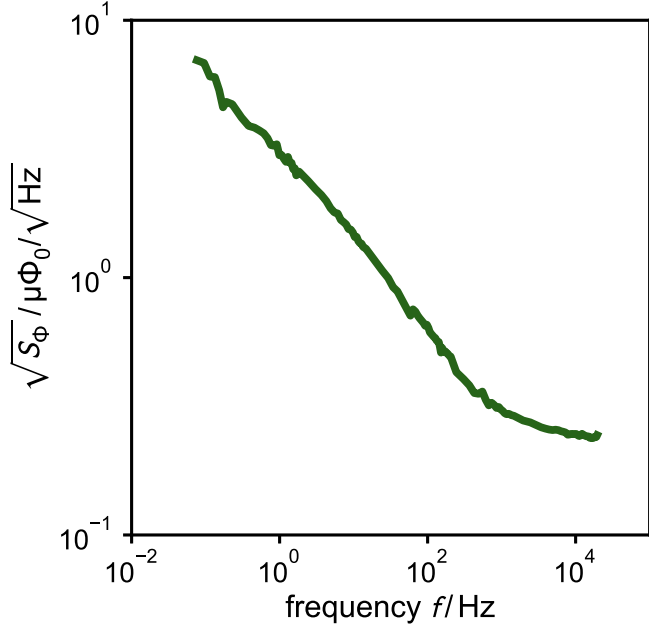


**Figure 2.11:** Square root power spectral density  $\sqrt{S_\Phi}$  against frequency with double logarithmic axes. Example data from a dc-SQUID fabricated within this thesis.

where  $S_V$  is the power spectral density of the voltage signal and  $V_\Phi$  the flux to voltage transfer coefficient. In Fig. 5.3 a typical power spectral density of our dc-SQUIDs operated in flux locked loop configuration is shown. We can describe the noise spectrum by summing up two contributions. For low frequencies up to  $f \approx 1 \text{ kHz}$  the noise is dominated by a  $1/f$  shaped contribution

$$S_{V, 1/f} = S_{V, 1/f} \left( \frac{1}{f} \right)^\alpha \quad (2.50)$$

where  $S_{V, 1/f}$  is the noise level at 1 Hz and  $\alpha$  denotes the noise exponent. For the most part, the physical origin of this noise component is still unclear. It has been found that in systems with two-level fluctuators, this kind of noise contribution is expected [Lan14], [Wu12]. Also experimental evidence was found that suggest superconducting vortex structures and  $I_c(\Phi)$  fluctuations contribute to this noise [Wel87]. For our SQUIDS we find an  $\alpha$  between 0.6 and 1 [Kem16].

Except the  $1/f$ -noise, all other noise contributions can be taken as independent of frequency allowing a compact representation with a white noise power spectral density contribution

$$S_V = S_{V,SQ} + S_{V,X} \quad (2.51)$$

$$= S_I^{\text{par}} R_{\text{dyn}} + S_I^{\text{cir}} L^2 V_\Phi^2 + S_{V,X} \quad (2.52)$$

where  $S_{V,SQ}$  describes the main voltage noise source of a SQUID. Here, the spectral density of the current noise results from the temperature dependent Johnson-Nyquist noise [Nyq28], [Joh28]. The parallel connection of the shunt resistances in the

SQUID-loop introduce the contribution  $S_I^{\text{par}} = 4k_B T / (R_s/2)$  and  $S_I^{\text{cir}} = 4k_B T / (2R_s)$  is introduced by the serial connection contribution due to the circular current, where  $R_{\text{dyn}} = (\delta I / \delta U)$  is the dynamic resistance of the SQUID [Tes77] with  $(\delta I / \delta U)$  the differential change of current with voltage.  $S_{V,x}$  denotes the noise produced by the other electronic components of the readout setup and other noise coupled into the system from external sources. Note that in some cases, noise produced by other electronic parts can contain some kind of frequency dependence, which has to be considered separately.

To compare SQUIDs with different loop inductances a more appropriate quantity is the energy sensitivity

$$\varepsilon(f) = \frac{S_\Phi}{2L} . \quad (2.53)$$

Hence, for optimal noise performance,  $V_\Phi$  and  $L$  need to be optimized. Note that one is limited on the SQUID loop inductance  $L$  due to increasing thermal noise fluctuations [Lik86]. Numerical computations have shown that

$$L < \frac{\Phi_0^2}{2\pi k_B T} \quad (2.54)$$

which yields an upper limit of roughly 1 nH at  $T = 4.2$  K. By means of numerical simulations [Bru82] found an optimal noise performance for a SQUID for  $\beta_L \approx 1$  and  $\beta_c \approx 1$ , in which case the frequency independent component of the energy sensitivity can be estimated with [Tes77]

$$\varepsilon \approx 16k_B T / \sqrt{LC} . \quad (2.55)$$

We cannot reduce the noise energy to zero just by reducing the cryostat temperature to zero, as we still have to consider the quantum noise limit and the excess heat produced by the shunt resistors.

## 2.6 Thermal Considerations for a Shunted SQUID at mK-Temperatures

Current sensing dc-SQUIDs offer an energy sensitive readout of an MMC detector [Fle05]. A rise in temperature of the detector and SQUIDs significantly effects the energy resolution, wherefore temperature should be lowered as much as possible in application. To boost the performance of dc-SQUIDs produced within the framework of this thesis a thermal model for a shunted SQUID at mK-temperatures is suggested based on [Wel94].

### 2.6.1 Thermal Conduction at mK-Temperatures

For a dielectric solid body the heat conductivity at low temperatures

$$\Lambda = \frac{1}{3} C v l \quad (2.56)$$

is proportional to the specific heat  $C$  per unit volume of the particles carrying the heat, their mean velocity  $v$  and their mean free path  $l$ . For the temperature approaching zero the phononic heat capacity can be described by the Debye Model. For a normal conductor we get an additional heat transport channel due to the free electrons. At very low temperatures the electronic heat conductivity

$$\Lambda_{\text{el}} = \frac{1}{3} C_{\text{el}} v_F l \quad (2.57)$$

is proportional to the electronic specific heat  $C_{\text{el}}$  per unit volume as described by the Sommerfeld model [Som27], the Fermi velocity  $v_F$  since only the electrons at the Fermi surface contribute and the mean free path  $l$ , which is at this temperature range dominated by defect scattering [Ens05]. We can eliminate the electron mean free path  $l$  by dividing (2.57) by the electrical conductivity  $\sigma$  assuming that both transport properties have the same physical origin, which at low temperatures is the defect scattering, leading to the Wiedemann-Franz law

$$\frac{\Lambda_{\text{el}}}{\sigma} = \mathcal{L} T \quad (2.58)$$

with  $\mathcal{L} = 2.45 \times 10^{-8} \text{ V}^2 \text{ K}^{-2}$  the Lorenz number [Kum93]. With above equations derived from simple solid state models we get a rough idea of the thermal transport and properties of dielectrics and metals at mK-temperatures.

For a bulk superconductor below the first critical magnetic field we find that the thermal transport in phonon and electron channel is suppressed compared to other solids [DG18]. Therefore we do not consider superconductors as parts of the thermodynamic.

### 2.6.2 Hot-electron Effect

In the mK-temperature regime it was found, that the phonon and electron system are not in thermal equilibrium. The electron temperature is decoupled from the phononic system, leading to a splitting of phonon and electron temperature  $T_E$  and  $T_P$  respectively, called hot electron effect [Wel94]. One has to note that the exact behavior of such systems is not very well described by existing theories. Assuming a smooth Fermi surface and considering only normal scattering processes between

electrons and phonons, the power transfer between the electron and phonon system can be described as

$$P = \Sigma \Omega (T_E^n - T_P^n) \quad (2.59)$$

where  $\Sigma$  is a material dependent factor,  $\Omega$  the volume and  $T_E, T_P$  the respective temperatures of electron and phonon system. In general the exponent of the temperature, which we shall call  $n$ , is material dependent and is found to range between 4 to 6, whereby for many system  $n = 5$  is assumed [Ple06]. It can be approximated by the energy relaxation rate between the electron and the phonon system

$$\tau_{E/P}^{-1} = \frac{n\Sigma}{\gamma} T_E^{n-2} \quad (2.60)$$

where  $\gamma$  is the Sommerfeld constant. This time constant lies in the range of a few microseconds [Ger01] and it, therefore, describes a slow process, associated with the slow energy exchange between electron and phonon system. The characteristic length  $l_{\text{hot}}$  an electron travels before thermalizing and emitting a phonon is given by [Wel94]

$$l_{\text{hot}} = \sqrt{D\tau_{E/P}} \quad (2.61)$$

where  $D$  is the diffusion constant. Considering a macroscopic model, the electronic thermal transport can be described by the Wiedemann-Franz law introduced in equation (2.58). The total heat balance is then [Gia06]:

$$\frac{P}{\Omega} - \Sigma(T_E^5 - T_P^5) = -\nabla \left( \frac{\mathcal{L}}{\rho} T_E \nabla T_E \right) \quad (2.62)$$

Here the first term  $P/\Omega$  represents the dissipated power in a volume element,  $\nabla$  is the Nabla operator and  $\rho$  the specific electronic resistivity of the material. This equation is analytically solvable for a one dimensional model where we extend the volume to infinity and apply the heat only at the beginning point  $x = 0$  with negligible phonon temperature  $T_P = 0$ . The electron temperature at distance  $r$  to the origin is then found to be [Sav06]:

$$T_E(r) = T_1 \left( 1 + \frac{x}{l_T} \right)^{-2/3} \quad (2.63)$$

$$l_T = \sqrt{\frac{14 L}{9\rho \Sigma} \frac{1}{T_1^3}} \quad (2.64)$$

where  $T_1$  denotes the temperature at  $x = 0$  and  $l_T$  acts as a measure for the thermal mean free path. To approximate  $l_{\text{hot}}$  one can use  $l_T$ , which is in reasonable agreement at mK-temperatures [Ple06].



**Figure 2.12:** A simplified thermal model for shunted SQUIDs in a cryostat. The SQUID temperature  $T_{SQ}$ , defined by the hot electrons in the shunt resistor, is thermally linked to the cooling fin via provided thermal link with coupling described by  $G_{Link}$ . The hot electron temperature in the cooling fin  $T_E$  is coupled to the phononic temperature of the cooling fin via the hot electron effect described by  $G_{hot}$ . The phononic temperature of the silicon chip  $T_S$  is coupled to the phonon temperature  $T_P$  of the cooling fins via the Kapitza resistance described by  $G_{Kapitza}$ . The cryostat acts as thermal bath at temperature  $T_0$ . It is thermally linked to the Silicon chip on which the SQUID sits by a thermal coupling described by  $G_{cryo}$ .

### 2.6.3 Thermal System of a Shunted SQUID with Cooling Fin

The main heating of a SQUID occurs at the shunt resistors, which dissipate the power

$$P = R_s I^2 \quad (2.65)$$

proportional to the shunt resistance  $R_s$  and current  $I$  which runs though the resistors. Another candidate for power dissipation are the junction itself or radiation losses, but the associated power dissipation is typically several orders of magnitude smaller in comparison to the power dissipated at a shunt resistor [Cla04]. With no other notable contributions to power dissipation the SQUID thermal system can be reduced to that of the shunt resistor itself.

A schematic of our thermal model describing a shunted SQUID in a cryostat is depicted in Fig. 2.12. It contains several thermal boundaries we will discuss in the following. In order to cool the shunt resistor and suppress the hot electron effect, it can be connected to a cooling fin via a metallic thermal link. The cooling fin allows the thermal electrons to spread in a larger volume, which in of itself reduces the temperature of the shunt. In a simplified manner the thermal conduction of the metallic thermal link can be described using the Fourier law

$$\dot{Q} = \Lambda_{el} \cdot A \cdot \frac{T_E - T_{SQ}}{d} \quad (2.66)$$

where  $\dot{Q}$  describes the heat transfer between the two systems with  $T_{SQ}$  the SQUID temperature and  $T_E$  the electron temperature of the cooling fin,  $\Lambda_{el}$  the electrical heat conductivity of the metal described by the Wiedemann-Franz law,  $A$  the cross section area and  $d$  the length of the link. Hot electrons couple to phonons of the

cooling fins. Ideally the phononic temperature  $T_P$  should be as close as possible to the bath temperature defined by the cryostat temperature  $T_0$  to boost the efficiency of the cooling fin. In order to do so, the phononic system needs to be in good thermal contact with the cryostat. Between the here used silicon chip and the metallic cooling fin, there is a phonon thermal boundary due to acoustic mismatch. A description of the phononic boundary between two materials can be given by the Kapitza resistance model [Lit59], [Pol69] derived from Snell's law. The power transferred between the thermal subsystems

$$P = KA_K \left( T_P^4 - T_S^4 \right) \quad (2.67)$$

is proportional to the kapitza resistance  $K$ , the surface area  $A_K$  and the phonon temperature  $T_S$  of the chip.

Overall, the proposed thermal model can be described in terms of thermal coupling factors  $G$  as

$$\dot{Q} = G (T_1 - T_2) \quad (2.68)$$

where  $\dot{Q}$  describes the heat transfer between the two systems with respective temperature  $T_1$  and  $T_2$ . A set of differential equation can be established to represent the heat flow between the thermal components as

$$C_{\text{shunt, el}} \dot{T}_{\text{SQ}} = -G_{\text{link}} (T_{\text{SQ}} - T_E) + P_{\text{in}} t \quad (2.69)$$

$$C_{\text{fin, el}} \dot{T}_E = G_{\text{link}} (T_{\text{SQ}} - T_E) - G_{\text{Hot}} (T_E - T_P) \quad (2.70)$$

$$C_{\text{fin, p}} \dot{T}_P = G_{\text{Hot}} (T_E - T_P) - G_{\text{Kapitza}} (T_P - T_S) \quad (2.71)$$

$$C_{\text{chip}} \dot{T}_S = G_{\text{Kapitza}} (T_P - T_S) - G_{\text{Cryo}} (T_S - T_0) \quad (2.72)$$

$$0 = G_{\text{Cryo}} (T_S - T_0) \quad (2.73)$$

Here each temperature represent the mean temperature of the components neglecting the spatial variations in the subsystems. Furthermore  $C_{\text{shunt,el}}$  the electronic heat capacity of the shunt resistors,  $C_{\text{fin,el}}$  the electronic heat capacity of the cooling fin,  $C_{\text{fin,p}}$  the phononic heat capacity of the cooling fin,  $C_{\text{chip}}$  the heat capacity of the chip.

As the power influx  $P_{\text{in}}$  is constant in time the system is expected to reach a steady state. This results in fixed temperatures of the subsystems. In consequence it is enough to solve a power balance equation of the form:

$$P_{\text{in}} = P_{\text{link}} = P_{\text{hot}} = P_{\text{kapitza}} = P_{\text{cryo}} . \quad (2.74)$$

The thermal bottle neck of the system defines the resulting power balance as it imposes the greatest restriction of thermal exchange between the subsystems. Assuming that the bottle neck does not change in the investigated temperature range

when measuring the white noise power spectral density  $S_\Phi$  of a single SQUID versus the cryostat temperature  $T_{\text{cryo}}$  the data can be fitted with

$$S_\Phi = A(T_{\text{min}}^{n+1} - T_{\text{cryo}}^{n+1})^{\frac{1}{n+1}} + c \quad (2.75)$$

where  $A$  is the conversion of temperature to the power spectral density, which will depend on the SQUID resistance and the readout method employed,  $c$  as an offset for the temperature independent noise,  $T_{\text{min}}$  the minimal reached temperature and the exponent  $n$  denotes the characteristic exponent of the type of thermal transport process corresponding to the bottleneck of the system.

### 3. dc-SQUID Multiplexer Method, Design and Fabrication

In this chapter, the new dc-SQUID multiplexer chips are presented and the underlying optimizations as well as their fabrication are discussed. Prior to this work, in [Ric21b] and [Hoi21], a dc-SQUID multiplexer chip with 4 dc-SQUIDs connected in series and corresponding readout scheme were developed. For simplicity we will refer to these in series connected dc-SQUIDs as an array. The 4-array was modulated with only one flux ramp generator signal connecting all modulation coils through a single line, whereby for each SQUID in the array the mutual inductance of the modulation coils differs. The first results of the successful proof-of-principle measurements were published in [Ric21a]. Although this method works well, in this thesis we add an additional degree of freedom within the operation of the multiplexer. For the previous approach the on chip fabricated modulation coils fix the ratios of the SQUIDS response frequency. Additionally if one of the modulation coils does not match the targeted mutual inductance, it negatively affects the operation of the multiplexer. Deviations between simulated inductance values with the state-of-the-art program InductEX<sup>1</sup> [Fou11] to the measured values can lie in a range of up to 10 % [Bau22]. Therefore, in this thesis, each SQUID in the array is provided with an individual flux ramp signal while all modulation coils possess the same mutual inductance.

The flux ramp method with one generator signal and different modulation coils is schematically depicted in Fig. 3.1 a). In comparison, the method with different generator signals and the same mutual inductances for all modulation coils is depicted in Fig. 3.1 b). The two SQUIDS SQ1 and SQ2 are connected in series and the voltage of the single SQUIDS  $V_1$  and  $V_2$  add up to  $V_{12}$ . The method developed within this thesis enables a change in the individual flux ramps. Therefore, it is possible to change the modulation frequency for each dc-SQUID as desired, by altering the amplitude or the modulation frequency. This adds a new freedom of operation to the dc-SQUID multiplexer, as each flux ramp can be individually configured as the setup is no longer bound by a rigid coil configuration. As a consequence the new method requires additional cables. However, connecting  $M$  different arrays to each other via  $N$  common flux ramp current lines, the number of cables required for readout is still reduced by  $2MN - N - M$  compared to a single stage flux locked loop readout. Such a configuration can be referred to as an  $N \times M$  multiplexer array [Ric21a]. For large  $N$  and  $M$ , the flux ramp multiplexing method introduced within

---

<sup>1</sup>SUNMagnetics, 15 De Beer Street, Stellenbosch, 7600, South Africa

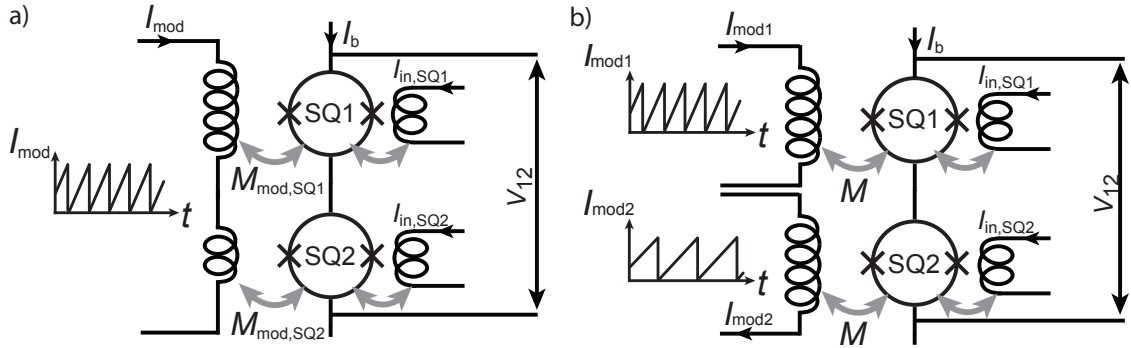


**Figure 3.1:** Schematic circuit diagrams of the two flux ramp modulation methods. a) Previous method: The mutual inductances  $M_{\text{mod}}$  of the modulation coils, depicted on the left side, differs for each SQUID, while the flux ramp generator signal, indicated by  $I_{\text{mod}}$ , is transmitted through a common line. The two depicted SQUIDs SQ1 and SQ2 a bias with  $I_b$ , get an input signal  $I_{\text{in}}$ . The added up voltage response  $V_{12}$  from the SQUIDS is measured through a single readout line .  
b) New method: The mutual inductance  $M$  of the modulation coils for each SQUID in the array is the same, but the generator signal is transmitted individually for each modulation coil in a SQUID array.

this thesis provides an effective way of reducing the number of cables. Therefore, the implementation of a  $N \times M$  multiplexer array, which is based on the new method, still reduces the cryogenic system complexity severalfold. In order to read out the  $16 \times 16$  MMC [Abe25] with 128 individual channels, a specifically customized multiplexer dc-SQUID chip was designed and fabricated. The intended readout system of the detector utilizes a  $4 \times 32$  multiplexer array. This reduces the number of cables by 220 compared to a single stage flux locked loop readout and by even 476 compared to a two-stage flux locked loop readout.

### 3.1 dc-SQUID Design

The heart of our device is the dc-SQUID. It has been shown in [Fle05] that current sensing dc-SQUIDs offer the best combination of energy resolution and bandwidth in comparison to other magnetic flux sensors for MMC detectors. In this thesis the dc-SQUID design presented in [Bau22] was adopted with some minor alterations. The already highly optimized dc-SQUID design represents the current high-end device produced by our research group.

One prominent change lies in the cooling fin design, which substitutes the former material AuPd with cooling fins made out of pure Au. In Fig. 3.2 an optical microscope picture of a dc-SQUID produced within the framework of this thesis is shown. The SQUIDs are mostly made out of Nb, which has the highest critical tempera-

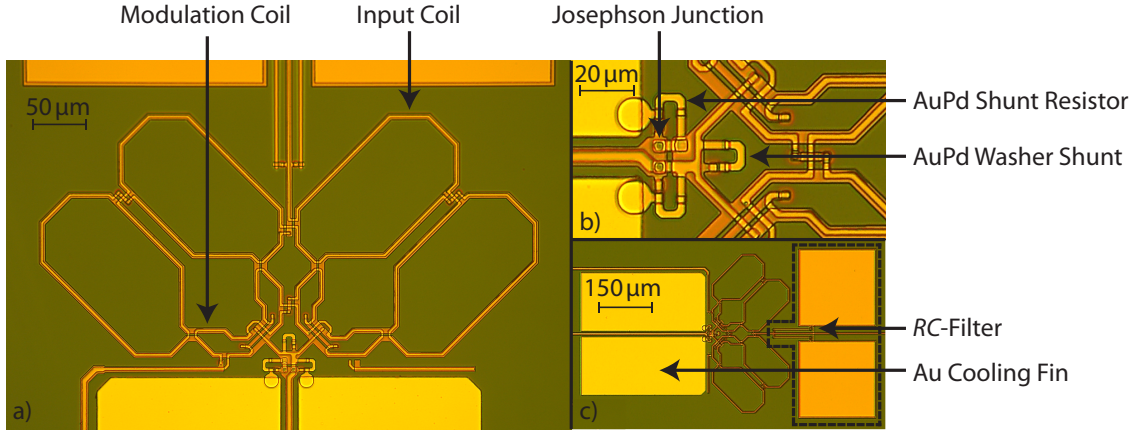


**Figure 3.2:** a) Optical microscope picture of a dc-SQUID produced within the framework of this thesis. The larger input and smaller modulation coil both rest on the underlying SQUID-loop forming a micro strip line configuration. b) Zoom-In into the junction area where the junctions and resistors are indicated. The round structure connecting the shunt resistor with the cooling fin are AuPd thermal links. c) Zoom-Out showing the Au cooling fins and the *RC*-filter unit.

tures  $T_c = 9.25$  K [Poo95] of all pure elements. It is a robust, non-poisonous material with a long history in superconducting applications. In the case of current-sensing dc-SQUIDs with a flux transformer, the detector signal is coupled into the SQUID via an input coil. It has been shown that in such an application the best energy sensitivity can be achieved if the detector coil, has the same inductance as the input coil of the SQUID, as this provides an impedance match which maximizes the signal-carrying current in the coupling coil of the SQUID [Knu88]. The detector coils of the maXs256 have a designed inductance of  $L_{in} = 1.6$  nH [Abe25]. In our recent designs the SQUID-loop is structured as a strip line configuration formed by the input and modulation coil to ensure a good magnetic coupling. To optimize the energy sensitivity of the SQUID small inductance values of the SQUID-loop are advantageous, according to (2.55). In our realization of the strip line configuration the shape of the input coil and SQUID-loop mates, in order to maximize the magnetic coupling. As an inductance value of 1.6 nH would be too large for the SQUID-loop in our application, we separate both coils into 4 individual loops with the same inductance value  $L$ . In the case of the input coil they are connected in series, therefore, the total input inductance is given as the sum of the four loop inductances  $L_{in} = 4L$ . For the SQUID-loop the separation into 4 loops allows to connect them in parallel, effectively reducing the inductance. The part of the SQUID-loop underneath the input coil can be estimated with  $L/4$ . Analogously, we separate the modulation coil and SQUID-loop underneath into 4 loops. The modulation coil inductance is not as restricted to a specific value as the input coil. On the one hand, to minimize the inductance of

**Table 3.1:** Overview of design target values for properties of the dc-SQUIDs produced within the framework of this thesis. In order to obtain the inductance and mutual inductances values the simulation programm InductEX was used.  $I_c$  and  $R_s$  follow from the requirements imposed on  $\beta_L$  and  $\beta_C$ .

	$L_{\text{in}}$	$L_{\text{mod}}$	$L_s$	$M_{\text{in}}^{-1}$	$M_{\text{mod}}^{-1}$	$I_c$	$R_s$
Design Values	1.64 nH	336 pH	147 pH	$6 \mu\text{A}/\Phi_0$	$42 \mu\text{A}/\Phi_0$	$6.0 \mu\text{A}$	$6 \Omega$

the SQUID-loop, the modulation coil is selected to be geometrically smaller than the input coil, which also reduces the coupling of the current noise from the generator. On the other hand, if the magnetic coupling of the modulation coil is too weak, large input currents are required for the operation, which is undesirable due to a resulting increase of the wire cross-talk and excess noise. Note that the cross-talk between the input coil and modulation coil is reduced, as they are geometrically separated from each other. This is important for the flux ramp readout approach, as the modulation coil is constantly supplied with a flux ramp signal. An overview of our SQUID design values can be found in Tab. 3.1. To obtain the values for the inductances of the input coil  $L_{\text{in}}$ , the modulation coil  $L_{\text{mod}}$ , the SQUID-loop  $L_s$  and the mutual inductances  $M_{\text{in}}$  between input coil and SQUID-loop,  $M_{\text{mod}}$  between modulation coil and SQUID-loop, we used the simulation program InductEX [Fou11].

At a fixed SQUID-loop inductance the value for the junction critical current is determined from the optimization requirement given by  $\beta_L \approx 1$  according to [Tes77]. Our Josephson junctions are made out of a Nb/Al-AlO<sub>x</sub>/Nb tri-layer. In the framework of this thesis the junctions were defined by a window-type fabrication process, see section 3.3.1. Although it is not easy to describe the relation between junction geometry and critical currents from a theoretical point of view, we can use the empirical relation  $I_c = A_{\text{eff}} J_c$  to calculate the required junction dimensions to fit the optimization demands. Here,  $A_{\text{eff}}$  denotes the effective junction area and  $J_c$  the critical current density, which is determined within the fabrication process through the  $p_{\text{ox}} t_{\text{ox}}$  oxidation parameters [Sto23]. For a SQUID-loop inductance of  $L_s = 147 \text{ pH}$  we aim for a targeted critical current of  $I_c = 6 \mu\text{A}$  at zero temperature. The oxidation parameters are chosen such that the targeted critical current density is  $J_c = 0.26 \mu\text{A}/\mu\text{m}^2$ , leading to an effective area of  $A_{\text{eff}} = 23 \mu\text{m}^2$ . From past experience, see e.g. [Kem13], the real junction area should be chosen somewhat smaller. Therefore, a junction area of  $A = 20.25 \mu\text{m}^2$  was chosen. To suppress the hysteresis of the junction characteristic and to ensure optimal SQUID performance, the requirement for the Steward Mc-Cumber parameter is  $\beta_C \approx 1$ . As a consequence, the target value of the shunt resistance is  $R_s = 6 \Omega$ . For an open loop application, as intended in this work, a maximization of the voltage swing is desirable. As the SQUID-loop is shunted by a washer shunt with resistance  $R_L$ , to dampen resonances, the relation between the

voltage swing and SQUID parameters is given according to (2.39). Inserting our design values we predict a voltage swing of  $\Delta V \approx 29 \mu\text{V}$  at zero temperature. The filter units including the SQUID-loop interruption shunt and the  $RC$ -filter of the input coil are intended to suppress resonances. They are described in detail in [Bau22].

The AuPd shunt resistors are connected to Au cooling fins through a thermal link made out of AuPd. Compared to the previous design the material of the cooling fin has been changed from AuPd to Au and the volume was significantly increased. A full description of the thermal behavior of this dc-SQUID discussing the influence of this change is given in section 3.2.2.

## 3.2 dc-SQUID Multiplexer Chip Designs

Within the scope of this work, two different multiplexer chips have been designed and fabricated. Both feature the same bondpad layout and electrical circuit. The main difference between them lies in the realization of the flux ramp transmission line configuration. For the chips of type I we implemented a large Au bondpad to allow for thermal anchoring via Au bond wires. Here, the transmission lines are densely packed in order to maximize the size of the Au bondpad. For the chip of type II the Au pad was omitted in order to spread out the densely packed transmission lines. First, the general layout and the electrical circuit of these two designs is discussed. Afterwards, the operating temperature of the chip of type I is examined based on the thermal model introduced in section 2.6.3. Finally, the changes in the transmission line configuration of the type II design are discussed.

### 3.2.1 General layout and electrical circuit

The general layout of the multiplexer chips is custom fit for the readout of the maXs256 [Abe25]. This detector requires 128 SQUID channels for its full readout. The SQUID chips are placed next to the detector, such that it is possible to directly connect them via Al bond wires. Consequently, the parasitic inductance between the detector coil and the SQUIDs input coil is reduced. To adapt to the detector, the outer dimensions of the multiplexer chips are  $4500 \mu\text{m} \times 4500 \mu\text{m}$ . Each chip is equipped with 8 SQUIDs which are divided into two separate arrays containing 4 SQUIDs each, based on the previous work [Hoi21] where dc-SQUID multiplexing with an array of length 4 was already successfully demonstrated.

The shared electrical circuit of both multiplexer chips is schematically depicted in Fig. 3.3. The input coils can be connected via Al bond wires at the IN bond pads. The IN-bondpad layout, as can be seen in e.g. Fig. 3.4, matches with the maXs256 bondpad layout. The voltage readout and bias current feed of a 4-array are connected

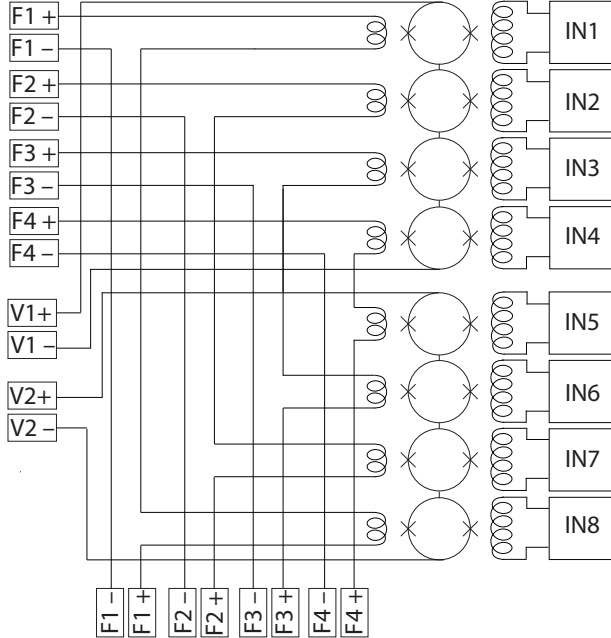


**Figure 3.3:** Circuit diagram of the FRM Multiplexer dc-SQUID chips. The 4 flux ramp bond pads are indicated by F1 to F4. Note that two additional groups of flux ramp bond pads found in the real design are not shown for simplification. The voltage measurement and bias current input is connected with the V pads. Each SQUID has its own input coil connection indicated by IN.

via the V bond pads. When measuring the voltage we always measure the voltage signal sum of 4 dc-SQUIDs. The 4 flux ramp lines are connected via the F1 to F4 bondpads. Each of the 4 individual flux ramp signals reaches a corresponding single SQUID of a 4-array, while both SQUID arrays on the chip share the same current ramp signal line. Note that, for the sake of simplicity, fewer F bondpads are shown in the circuit diagram compared to the real design. The additional F bondpads allow for more connection flexibility, which is needed due to the dimensional limitations provided by the detector setup. As can be seen in Fig. 3.3, the corresponding F+ and F- bondpads are not connected with each other and, therefore, additional on-chip bonds are required in order to connect the flux ramp lines. This is intentional as with this flux ramp line configuration it is possible to connect several chips such that they share the flux ramp lines. Therefore, in total only 4 current ramps are required for a complete detector readout. Due to the many crossovers in the circuit, both designs require a large number of vias connecting the upper and lower niobium layers with each other. As fabrication-related errors can often occur on such crossovers, the size of the vias has been significantly increased compared to previous designs in order to achieve an overall more fault-tolerant fabrication process.

### 3.2.2 Type I design with thermal anchoring possibility

The dc-SQUID multiplexer chip shown in Fig. 3.4 not only realizes the new flexible multiplexer approach, but also allows for thermal anchoring. In practice, this can reduce the operating temperature of the detector setup depending on the realization.

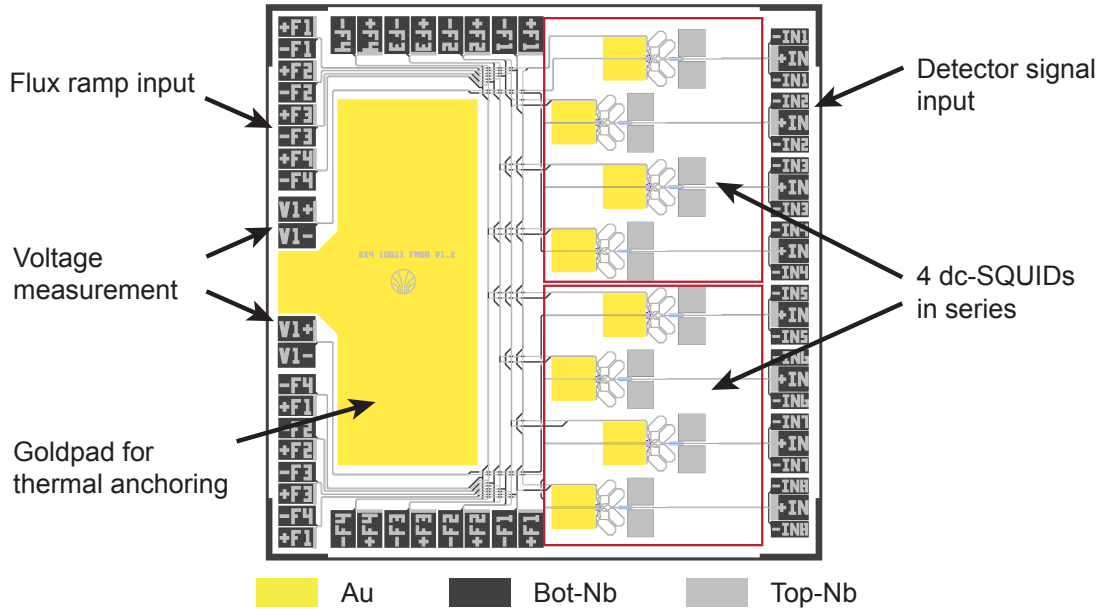


**Figure 3.4:** FRM multiplex dc-SQUID chip design featuring a large gold bondpad for thermal anchoring to the cryostat.

While operating the SQUIDs, the chip is heated due to the heat dissipation in the shunt resistors. This affects the energy sensitivity of the SQUIDs and it can cause excessive heating of the entire detector setup. In the following, the expected operating temperature of the single SQUID is investigated based on the thermal model 3.1 and subsequently the operating temperature of the whole multiplexer chip.

The power dissipated in the resistive shunts which heat the SQUIDs can be calculated with (2.65). With a shunt resistance value of  $R_s = 6\Omega$  and a current of  $I = 14\mu\text{A}$  transversing through the resistors, the expected heating power of a single shunt results to roughly  $P_{\text{in}} = 300\text{ pW}$ . As in our multiplexer application the SQUIDs are intended to operate continuously, the system will reach a steady state. Then the input power is equal to the power outflow  $P_{\text{in}} = P_{\text{out}}$  determining the operating temperature of our system. In the model the power flow of the system is determined by the thermal coupling of five subsystems described by the thermal link heat conduction, the hot-electron effect, the Kapitza resistance and the thermal coupling to the cryostat. At mK-temperatures, Wellstood et al. [Wel94] determined that the hot-electron effect is the major thermal bottleneck for small resistors. They demonstrated that with an attachment of a metal cooling fin to the resistor a cooling effect is achieved, even fully suppressing the hot-electron bottleneck to the point where the thermal bottleneck is shifted to other thermal subsystems. To check if the maximum cooling effect due to the cooling fin is reached for our SQUID design, the material of the cooling fin is changed from AuPd to Au. In addition to changing the material, the volume of the

cooling fin was considerably increased.

First, our realization of the thermal link shown in Fig. 3.2 b), which is situated between the shunt resistor and the cooling fin, is discussed. The AuPd resistor is connected via superconducting Nb contact pads, therefore, the AuPd region covered by superconducting Nb does not contribute to the electrical resistance. The AuPd thermal link extends from the AuPd structure at a point where it is covered with Nb. As the cooling fin is not electrically connected, the thermal link does not change the resistance value. For our sputter deposited AuPd a specific electrical resistance of  $\rho_{\text{AuPd}} = 27 \mu\Omega\text{cm}$  at low temperatures was measured. After the Wiedemann-Franz law (2.58), this results in an electrical heat conductivity of  $\Lambda_{\text{AuPd}}(T = 10 \text{ mK}) = 9.4 \times 10^{-4} \text{ WK}^{-1}\text{m}^{-1}$ . The targeted cross-section area  $A_{\text{link}} = 0.9 \mu\text{m}^2$  and length  $d_{\text{link}} = 8 \mu\text{m}$  of the thermal link. Inserting these values into the Fourier law (2.66) for a temperature difference of  $\Delta T = 1 \text{ mK}$ , the power flow between the two ends of the thermal link results to only  $P_{\text{link}} \approx 1 \text{ pW}$ . This is already below the expected heat power influx  $P_{\text{in}}$ , indicating that the thermal link is a likely candidate for a thermal bottleneck.

A cooling fin increases the effective volume where the heat can spread. In addition, it suppresses the hot-electron effect, because the power flow between the electronic and phononic subsystem is proportional to the volume  $\Omega$ . The change in material from AuPd to Au was motivated by the better expected cooling behavior of Au. The specific electrical resistance of sputtered Au can be estimated with  $\rho_{\text{Au}} = 1.8 \mu\Omega\text{cm}$  [Ple06] and is lower compared to  $\rho_{\text{AuPd}}$ , enhancing the thermal transport in the cooling fin. Subsequently according to (2.64) the hot-electron mean free path is larger. Calculating the path for our material values we obtain  $l_{T,\text{Au}} = 30 \mu\text{mK}^{3/2}T^{-3/2}$  for Au and  $l_{T,\text{AuPd}} = 14 \mu\text{mK}^{3/2}T^{-3/2}$  for AuPd. For an Au cooling fin at  $T = 10 \text{ mK}$  the effective cooling range is 3 mm, quickly reducing to 30  $\mu\text{m}$  at  $T = 1 \text{ K}$ . When the cooling fin dimensions exceed the effective cooling range additional shot noise [Gia06], [Ste96] [Nag95] is expected, therefore, one should opt to appropriately dimension the cooling fins. The single SQUIDs fabricated within the scope of this thesis have cooling fins of length 350  $\mu\text{m}$ . This allows for an effective operation without a significant addition of shot noise up to a cooling fin temperature of approximately  $T = 200 \text{ mK}$ . Below this temperature, the entire volume of the fin is expected to contribute to cooling, which according to the design is  $\Omega = 57750 \mu\text{m}^2 \cdot h$  with thickness  $h$ . In addition to increasing the hot-electron mean free path by changing the material, the measured value of the hot electron material-dependent constant for Au  $\Sigma_{\text{Au}} \approx 2.4 \times 10^9 \text{ WK}^{-5}\text{m}^{-3}$  is larger in comparison to AuPd with  $\Sigma_{\text{AuPd}} \approx 0.8 \times 10^9 \text{ WK}^{-5}\text{m}^{-3}$  [Ple06]. According to (2.62) the power flow restricted by the hot-electron effect a minimum electron temperature in the cooling fin of  $T_E = 88 \text{ mK}$  is obtained, when assuming a thickness of  $h = 0.4 \mu\text{m}$  the total volume becomes  $\Omega = 23100 \mu\text{m}^3$ .

and setting the temperature of the phononic system to zero  $T_P = 0\text{ K}$  and using  $P_{\text{hot}} = P_{\text{in}}$ .

Next, the Kapitza resistance thermal boundary between the Au cooling fin and Si is investigated. The Kapitza resistance value between a Au and Si surface has to be measured for upfront structure, but from similar interfaces, we expect a Kapitza resistance in the regime of  $K \approx 10 \times 10^3 \text{ WK}^{-4}\text{m}^{-2}$  [Ple06]. According to (2.67) the power flow between the two phonon systems results in  $T_P = 28\text{ mK}$ , when adopting the interface area of  $A_K = 57750\text{ }\mu\text{m}^2$ , setting the chip temperature equal to zero and  $P_{\text{Kapitza}} = P_{\text{in}}$ .

The chip is glued e.g. with GE-varnish onto a copper platform at a bath temperature  $T_0$ . Due to the often poor thermal contact given by the temperature gradient between cryostat and chip can be expected. For the thermal boundary produced by the glue a Kapitza heating model can be used. In order to estimate the temperature of the chip, a Kapitza resistance of  $K = 20 \text{ WK}^{-4}\text{m}^{-2}$  is adopted from [Wel94]. Calculating the chip temperature with the Kapitza heating model (2.67) with our chip interface area of  $A = 20.25\text{ mm}^2$  and the total heat load  $P = 16P_{\text{in}} = 4.8\text{ nW}$  of 8 SQUIDs results roughly to  $T_S = 60\text{ mK}$ . Adding a Au bondpad of large volume and area the thermal coupling to the cryostat can be significantly improved. With an appropriate number and distribution of Au bonds the on-chip temperature is expected to match the temperature of the cryostat  $T_0$ . As due to its large volume of  $V = 1.3 \times 10^{-3}\text{ mm}^3$  and surface area  $A = 3.3\text{ mm}^2$  the hot-electron effect and Kapitza boundary resistance to the substrate are negligible. Overall the Au bond pad represents an upgrade to the thermal setup, as there is practically no thermal boundary resistance between chip and cryostat. More importantly it allows to remove the heat more efficiently to dedicated heat sink channels away from the MMC.

Not considering the thermal boundary given by the thermal link the SQUID operating temperature the power balance equation (2.75) is solved by

$$T_{\text{SQ}} = \left[ \frac{P_{\text{in}}}{\Sigma\Omega} + \left( \frac{P_{\text{in}}}{KA_K} + T_S^4 \right)^{(5/4)} \right]^{(1/5)} . \quad (3.1)$$

When considering  $P_{\text{in}} = 300\text{ pW}$  and  $T_S = 60\text{ mK}$  the roughly estimated operating temperature is  $T_{\text{SQ}} = 90\text{ mK}$ . Compared to the old design with AuPd cooling fins, where after inserting the design parameters found in [Bau22], the operating temperature results to roughly  $T_{\text{SQ}} = 150\text{ mK}$ .

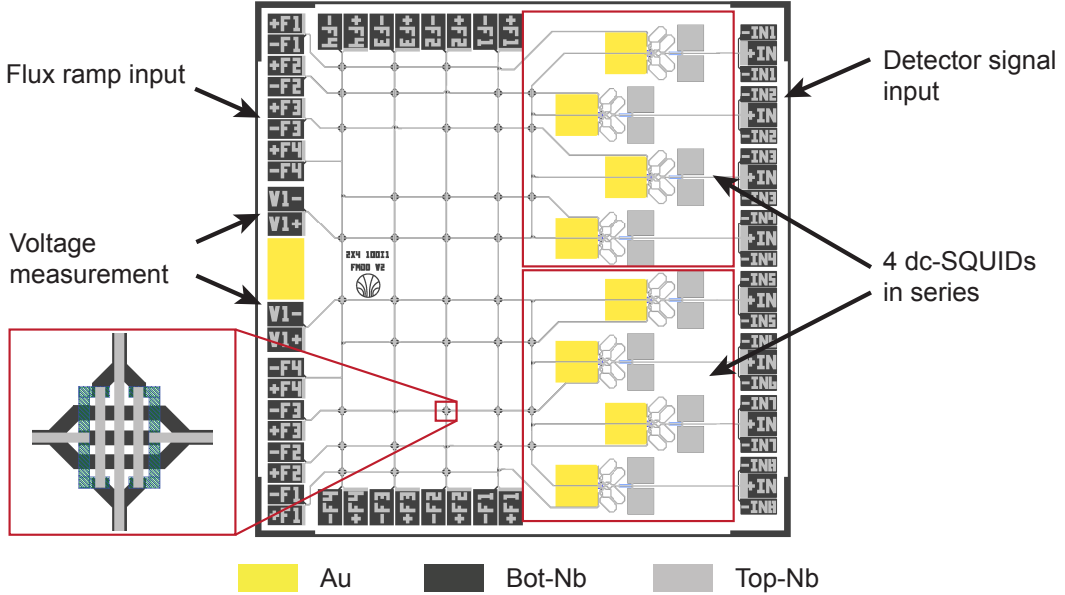


**Figure 3.5:** FRM multiplex dc-SQUID chip design of type II. The inset shows the top to bottom Nb crossover configuration.

### 3.2.3 Type II design with emphasis on a more spread out transmission line schema

On both multiplexer chips, the transmission lines are arranged in a stripline configuration, which has several upsides. The current in the upper and the lower lines runs in opposite directions, which results in a significant reduction of the magnetic field around a transmission line [Kai04].

For an ac-current the length of the path between two meeting points in the stripline, the transmission velocity and the frequency (and signal shape) have to be considered, in order to validate the assumption of a reduced magnetic field. For our FRM application, which uses sawtooth generator signals, this assumption holds, except at the ramp rests. This results in a ringing effect, which distorts the readout signal around the ramp reset and must therefore be discarded in readout.

Even though the stripline configuration suppresses the magnetic field around a transmission line, an increased distance between the individual conductors can further reduce the cross-talk.

The dc-SQUID multiplexer chip design shown in Fig. 3.5 omits the large Au bond pad in favor of an overall more spread out transmission line configuration. Due to the more spread-out transmission lines, the design allows for a different type of crossover configuration in between the Nb layers, shown in the inset of Fig. 3.5. For

the multiplexer chip of type I the stripline configuration is broken at the crossover points. The new crossover configuration reduces the amount of single vias by a factor of 3. As vias are more fragile structures from a fabrication point of view, this structure is expected to enhance the yield. Further, it features a coplanar waveguide geometry, where the ground wire encloses the signal-carrying conductor from both sides.

### 3.3 HDSQ18-Wafer series

Within the scope of this thesis two SQUID wafers have been fabricated, HDSQ18a and HDSQ18b, both containing five different chip types. Each wafer is composed of the two multiplexer chips shown in Fig. 3.4 and 3.5 and a chip containing 4 single SQUIDs, as well as two different kinds of test chips. The chip containing single SQUIDs can be used to fully characterize our single SQUIDs discussed in section 3.1. In turn the expected behavior of the multiplexer array can be inferred. Below, the fabrication steps will be discussed in detail.

#### 3.3.1 Fabrication

The SQUID wafers developed and characterized within the scope of this work were produced in the institute's clean room using thin-film technology. Our Josephson tunnel contacts were produced according to the window-type process discussed in [Bau22]. For the first time, a Nb/Al-AlO<sub>x</sub>/Nb trilayer [Sto23] from the sputter deposition system PREVAC<sup>2</sup> was used to construct high-resolution window type dc-SQUIDs successfully. The entire fabrication process is briefly described below. The schematic depiction in Fig. 3.6 gives an overview of the process steps involved. In the first step of the process, depicted in Fig. 3.6 a) the Nb/AlO/Nb trilayer is in-situ deposited onto the surface of a 3 inch Si-wafer substrate. The 18 nm thick Al layer, which was deposited onto a previously deposited 250 nm thick Nb layer, is oxidized in a pure oxygen atmosphere with pressure  $p_{\text{ox}}$  over a defined period of time  $t_{\text{ox}}$ . Here, the product  $p_{\text{ox}}t_{\text{ox}}$  was chosen to obtain a critical current density of  $J_c = 0.26 \mu\text{A}/\mu\text{m}^2$  [Sto23]. After oxidation a second Nb layer of thickness 120 nm was deposited.

The structure of the top electrode of the Josephson junction is defined using UV-photolithography, wherefore a photoresist mask of the positive photoresist AZ MIR 701<sup>3</sup> is structured by an MLA<sup>4</sup> laser lithograph. Afterwards the uncovered top Nb

<sup>2</sup>PREVAC sp. z o.o., Raciborska 61, PL-44362 Rogów, Polska

<sup>3</sup>Merck KGaA, Frankfurter Straße 250, 64293 Darmstadt, Deutschland

<sup>4</sup>Heidelberg Instruments Mikrotechnik GmbH, Mittelgewannweg 27, 69123 Heidelberg, Deutschland

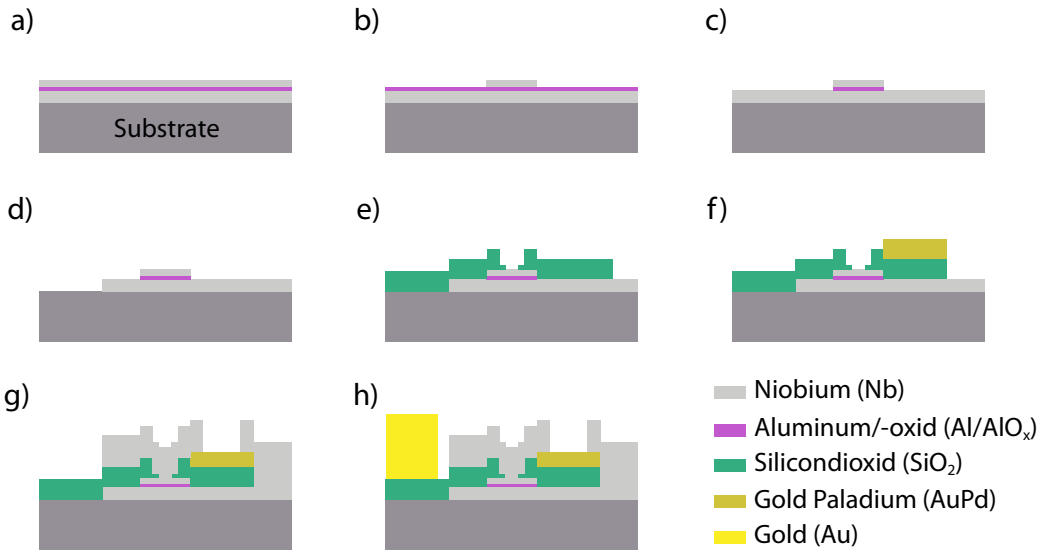


**Figure 3.6:** Schematic depiction of the dc-SQUID fabrication process. a) After Nb/Al-AlO<sub>x</sub>/Nb tri-layer deposition, b) after structuring the top electrode using a dry etch process, c) after structuring the Al-AlO<sub>x</sub>-layer with a chemical etching process, d) after structuring the base electrode using a dry etch process, e) after SiO<sub>2</sub> layer deposition and lift-off, f) after shunt resistor AuPd-layer deposition and lift-off, g) after top Nb-layer deposition and lift-off, h) after Au-layer deposition and lift-off.

layer is dry etched in an Oxford PlasmaPro 100 Cobra<sup>5</sup> with an ICP-RIE dry etch process using an SF<sub>6</sub>/Ar atmosphere. The resulting structure is depicted in Fig. 3.6 b). This determines the size of the junction area contacting the top electrode. As a next step the Al layer is wet chemically etched with an acid solution consisting of 16 parts phosphoric acid H<sub>3</sub>PO<sub>4</sub>, 1 part nitric acid HNO<sub>3</sub>, 1 part acetic acid CH<sub>3</sub>COOH and 2 parts water H<sub>2</sub>O. Once this step has been completed the top electrode structure as depicted in Fig. 3.6 c) is defined. Analogously to the top Nb layer the bottom Nb structure, shown in Fig. 3.6 d), is defined. In order to galvanically insulate the bottom Nb electrode two insulating SiO<sub>2</sub> layers of thickness of 125nm respectively are rf-sputter deposited, shown in Fig. 3.6 e). These insulating layers are structured via a lift-off process using a negative photoresist.

We usually sputter SiO<sub>2</sub> with a process gas mixture of Ar and O<sub>2</sub> in a ratio of 60:40. When SiO<sub>2</sub> sputtering in the Alcatel<sup>6</sup> sputter system without the addition of oxygen, the sputtering rate is significantly increased. On top we found that the magnetic signal of the SiO<sub>2</sub> can be reduced this way. Herefore we compared the mag-

<sup>5</sup>Oxford Instruments Plasma Technologies, North End, BS49 4AP Yatton, Bristol, United Kingdom

<sup>6</sup>CIT Alcatel, Departement industries, Division Technologie du Vide, Etablissement d'Annecy, Boite postale 2069, 98, avenue de Brogny 74009 Annecy, France

netization, measured with the MPMS-XL5<sup>7</sup>, of several thin foils containing 300 nm SiO<sub>2</sub> sandwiched between 500 nm thick Au layers. As this might be a step towards a new development of low flux noise SQUIDs within our group the first wafer in the series HDSQ18a w1 was fabricated using the SiO<sub>2</sub> with no additional oxygen inlet. However, the production of the wafer failed, as the brittle-looking SiO<sub>2</sub> broke off the Nb layer underneath during the following lift-off processes. Other test wafers using a 100:0 ratio showed similar brittle SiO<sub>2</sub>, although a break-off did not occur on wafer scale. It was shown that the insulating properties still hold. A more detailed discussion will be found in future publication of our group. The second wafer in the series HDSQ18b was fabricated using the standard 60:40 ratio.

In the next step, see Fig. 3.6 f), the shunt resistor layer made from dc-sputtered AuPd with a number ratio of 37.5:62.5 is deposited using the DCA<sup>8</sup> sputter system. The thickness of the AuPd layer is 260 nm. From the resistance measurement of the test structures, we expect a sheet resistance of  $R_{\square} = 1.9 \Omega/\square$ . Analogous to the insulating layers it is structured via a lift-off process using a negative photoresist. Afterward, a 600 nm thick Nb layer is dc-sputter deposited in the DCA sputtering system connecting the bottom Nb through the window-type Josephson junction, see Fig. 3.6 g). Again the structure is defined via a lift-off process using a negative photoresist. In the last step, a Au seed layer of 100 nm thickness is dc-sputter deposited in the DCA sputtering system. However, a small piece of the HDSQ18b wafer broke off and the subsequently planned electroplating up to a total Au layer thickness of 1  $\mu\text{m}$  was not possible with our setup. Instead an additional Au layer was sputter deposited, such that the total thickness of the Au layer is approximately 400 nm. On the wafer HDSQ18b an overall yield of roughly 70% was achieved.

---

<sup>7</sup>Quantum Design GmbH, Breitwieserweg 9, 64319 Pfungstadt, Deutschland

<sup>8</sup>DCA Instruments Oy, Aerotie 6, FIN 20360 Turku, Suomi



## 4. dc-SQUID Flux Ramp Modulation Setups

In this chapter the experimental setups developed within this work concerning the readout of the FRM dc-SQUID multiplexer are presented. First the properties of the transmission cables, which are shared by all experimental setups developed within this work, are discussed with regards to their implementation for the readout of the FRM multiplexer. Afterwards the shared room temperature electronics components for the flux ramp multiplexing are showcased. For a fully automated readout we intend to use a field-programmable gate array (FPGA) whose firmware modules are being developed at the Institute for Data Processing and Electronicss<sup>1</sup>. This array controls a digital-to-analog converter (DAC), which provides the flux ramp, and an analog-to-digital converter (ADC). The ADC in turn digitizes the SQUID voltage response after amplification at room temperature. As the FPGA units are currently under a reconfiguration process, a provisional setup was used in this work. It emulates the functions of the boards to a certain degree, such that the functionality of the FRM multiplexer chips was demonstrated successfully. The first showcased setup allows the testing of the FRM multiplexer dc-SQUID chips in a liquid helium dewar or in a cryostat. Finally, the setup for the  $16 \times 16$  pixel MMC array readout with the FRM dc-SQUID multiplexer is presented.

### 4.1 Transmission Lines

A transmission line can be described by an *RLC*-model [Kai04], where  $R$  stands for the resistance,  $L$  for the inductance and  $C$  for the capacitance of the line. Within this model a perfect coaxial cable is able to transmit high frequency signals without loss. A straight coaxial cable can be seen as a homogeneous conductor, meaning that the *LC*-components are spread out evenly across the cable without irregularities. The transmission speed and impedance of a homogeneous conductor is independent of the signal current frequency. Typically a coaxial cable consists of an inner wire surrounded by a thin outer braided metal sheath where the space in between is filled with a flexible insulating material. In addition the cable is surrounded by an outer insulating sheath made of flexible plastic. This cable structure provides excellent shielding, as the outer metal sheath acts as a Faraday-cage and thus shields the inner signal-carrying wire from electromagnetic field disturbances. As the metal sheath of the coaxial cable is the return conductor for the signal, it provides a magnetic shield-

---

<sup>1</sup>Institut für Prozessdatenverarbeitung und Elektronik KIT Campus Nord, Geb. 242, 76344 Eggenstein-Leopoldshafen

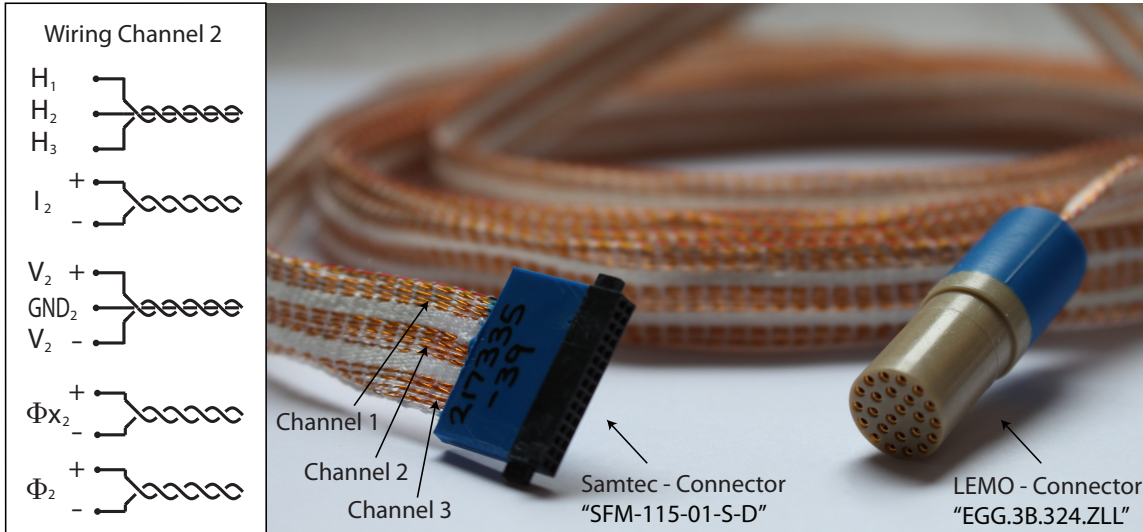


**Figure 4.1:** Picture of a Tekdata cable [All17] with wiring schematic. The Tekdata cable consists of twisted pair and twisted triple CuNi<sub>2</sub> wires of wire thickness 0.2 mm. At one end it is connected with a 30-pin Samtec-Connector SFM-115-01-S-D on the other end with a 24-pin LEMO-Connector EGG.3B.324.ZLL. It consists of three separate channels each containing three twisted pairs, which we call I,  $\Phi_x$ ,  $\Phi$  respectively and a twisted triple V+,V-,GND. Additionally a twisted triple H1,H2,H3 exists in the cable. This makes a total of 9 twisted pairs and 4 twisted triples.

ing to the outside. All together coaxial cables with their conduction and shielding properties are an excellent choice for high frequency signal transmission. In our setup the room temperature electronics are connected via  $50\Omega$  input impedance coaxial cables. The  $^3\text{He}/^4\text{He}$  dilution refrigerator used within the scope of this thesis however does not have enough coaxial cables installed for a full  $16 \times 16$  pixel MMC array detector readout, which is why we opt to readout our multiplexer via the installed cables built by Tekdata<sup>2</sup> described in [All17]. The Tekdata cables mainly consist of unshielded twisted pairs and triples of Cu<sub>9</sub>8Ni<sub>2</sub> with a diameter of 0.2 mm and have a length of 2.2 m. In Fig. 4.1 a photo of a Tekdata cable with a schematic description of the wiring, consisting of 4 triples and 9 pairs, is shown. A twisted pair or triple copper wire gives rise to an inhomogeneous LC-chain, which is associated with a frequency dependent transmission and subsequent signal loss. Therefore it was tested, whether the Tekdata cables are compatible with the planned readout scheme. In our multiplexer application a sawtooth flux ramp signals of about 100 kHz and an amplitude of a few  $\mu\text{A}$  and as well as the response signals of a multiplexed SQUID array with a frequency of about 10 MHz and an amplitude of a few  $\mu\text{A}$  are to be transmitted. In order to determine the suitability a few basic measurements were

<sup>2</sup>Tekdata Interconnections Limited, Innovation House, The Glades, Festival Way, Etruria, Stoke-on-Trent, Staffordshire, ST1 5SQ, UK, <http://www.tekdata-interconnect.com/>

conducted, which specify the cross talk and conduction properties for relevant frequency ranges and signal shapes. For a dc-current transmission of a few  $\mu\text{A}$  it was shown [All17] that the cables have a negligible cross talk compared to the noise of a Magnicon XXF-1 SQUID electronics<sup>3</sup>. In similar fashion to [All17] the signal degradation for relevant ac-current signals were tested. A sawtooth signal with 100 kHz or a 10 MHz sine shaped signal were generated with a frequency generator HEWLETT PACKARD 33120A<sup>4</sup> and the direct signal output was compared to the signal obtained through a flux ramp transmission line of the experimental setup including the FRM multiplexer SQUID-chip. The sine shaped signal showed no visible deterioration, which demonstrates the compatibility of the multiplex setup readout through a Tekdata cable. For the sawtooth signal the sharp peak is smeared out and after the ramp reset a ringing effect appears. This coincides with expectations, as a sawtooth signal consists of a Fourier-series with frequency components above the termination frequency of the twisted wire cables.

## 4.2 Room Temperature Readout Electronics

For the full readout of a flux ramp multiplexer it is necessary to generate a flux ramp signal and to demodulate the phase of the carrier of each multiplexer channel. In [Hoi21] a single digital processing unit was used to fulfill these two demands. A detailed description of the FPGA firmware modules for the flux ramp generation and the data processing developed at IPE is found in [Wol20]. For the readout of the maXs20-256-16 we want to use these electronics, which is why all setups developed within this work are intended to run with the FPGA-based electronics. However our boards are currently under a configuration process and could not be used to obtain data within this thesis.

### 4.2.1 FPGA-based dc-SQUID Flux Ramp Multiplexing

The FPGA-based electronics allows to digitally generate flux ramp signals, which are converted into a voltage signal by a digital to analog converter evaluation module. Furthermore the FPGA electronics demodulates the phase of the multiplexer signal with a commercial high-speed analog to digital converter evaluation module to digitize the voltage output of the multiplexer. In Fig. 4.2 a picture of the digital processing unit is shown. It consists of the XilinxZCU102 evaluation board<sup>5</sup> connected to

---

<sup>3</sup>Magnicon GmbH, Barkhausenweg 11, 22339 Hamburg, Deutschland

<sup>4</sup>HP Inc. 1501 Page Mill Road, Palo Alto, California, CA 94304

<sup>5</sup>Xilinx, Inc.2100 Logic Drive, San Jose, CA 95124 United States

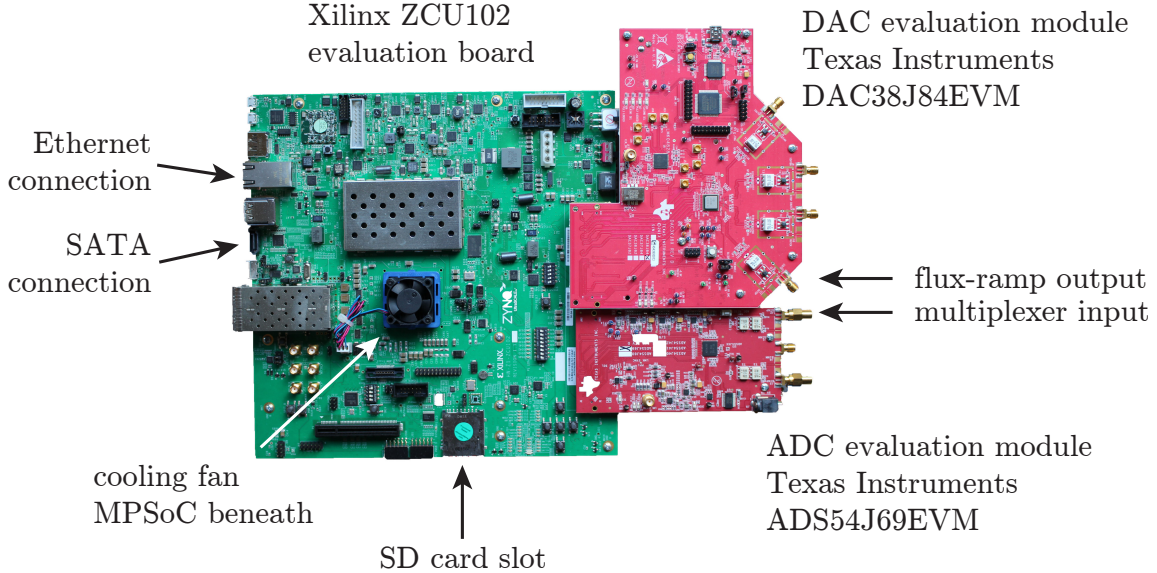


**Figure 4.2:** Photograph of the Xilinx ZCU102 evaluation board connected with DAC and ADC evaluation modules. The multiprocessor system on a chip is located below the cooling fan in the middle of the board. Illustration adopted from [Hoi21].

a DAC38J84EVM (DAC) from Texas Instruments<sup>6</sup> and an ADS54J69EVM (ADC) from Texas Instruments.

The readout electronics are based on a multiprocessor system on a chip (MPSoC) that combines a powerful quad-core ARM Cortex-A53 with a Xilinx Zynq Ultra-Scale+ FPGA. The latter performs all signal processing steps and the generation of the flux ramp signal shape simultaneously. The ARM Cortex-A53 performs slow control such as calibration procedures and data transmission to the storage backend. A Linux system runs on the ARM Cortex-A53 of the evaluation board to allow for remote control via Ethernet. The DAC and ADC evaluation modules are each connected via a FPGA Mezzanine Card (FMC) interface to the MPSoC of the Xilinx ZCU102. The flux ramp voltage signal is generated on the DAC. It offers 16 bit resolution with a sample rate of 2.5 GHz on each of the four output channels, which are connected via SMA connections. The differential current signal generated by the DAC is transformed into a voltage signal by two transformers on the evaluation board. The factory transformers on the module are primarily designed for frequencies in the range of some hundred megahertz, whereas frequencies below 10 MHz are attenuated. However, in our flux ramp multiplexing approach we require repetition rates in the range of 1 MHz. Therefore we have to replace the on chip transformers JTX-2-10TA+ and MABA-007159 by e.g. two ADTT1-6+ with a frequency range of 15 kHz to 100 MHz. In our dc-SQUID flux ramp approach we aim for a multi-

<sup>6</sup>Texas Instruments, Inc. 12500 TI Blvd. M/S 8656 Dallas, TX 75243. (214) 567-6450.

plexer carrier frequency in the range of several MHz, therefore the sampling rates of commercial high-speed ADC evaluation modules are sufficient to digitize the voltage output of the multiplexer. The ADC samples the multiplexer output voltage via the input SMA connections. The ADS54J69EVM supports sampling frequencies up to 500 MHz with a 16 bit resolution. Both onboard clocks of the DAC and ADC evaluation module can be synchronized by an external 10 MHz reference clock signal.

### 4.3 Signal Processing and Data Analysis

An essential part in the application of flux ramp modulation is the accurate determination of the phase factors. For each flux ramp segment one phase value is determined from the corresponding SQUID voltage signal. A straight forward way to determine the phase is to perform a Fourier transform for each segment of the SQUID response and evaluate the Fourier coefficients at the corresponding carrier frequency. Together with the SQUID voltage time trace and the sync signal of the signal generator we are able to locate the beginning of each flux ramp in the time trace. Beforehand the carrier frequencies  $f_c$  of each SQUID in the array are manually adjusted to a target value. This is possible due to the newly developed method, which allows to freely adjust the carrier frequency of single SQUIDs in the multiplexer array. With a known carrier frequency, the phase of the associated sinusoidal periodic frequency signal can be determined even without a Fourier transformation, but rather with down mixing [Mat12].

In general, a periodic continuation of a finite data set is not given, since the measured signal does not a priori correspond to an integer number of periods. If a Fourier transformation of such data sets is carried out, additional frequency components can be obtained which were not contained within the original signal, smearing out the resulting spectrum. This spreading effect is called spectral leakage. Additionally in the operation of the FRM the aforementioned ringing effect after a flux ramp reset deteriorates the SQUID response. It is possible to counteract both issues by discarding a certain amount of the voltage time trace at the start and end of the flux ramp signals. To optimize the accuracy of the discrete Fourier transform all carrier frequencies should be chosen such that all SQUIDs responses are equal to an integer number of flux quanta over the chosen time trace window. The evaluated phase values are convert into units of magnetic flux  $\Phi_0$  according to (2.42). With the sampling rate given by the flux ramp repetition rate  $f_{\text{mod}}$ , the time trace of the SQUID signal can be reconstructed.

## 4.4 Amplifier Chain

In order to resolve the SQUID signal, which has a voltage amplitude of a few  $\mu\text{V}$ , amplification is needed. The voltage signal of the multiplexer is amplified by an amplifier chain consisting of room temperature amplifier ZFL-500LN+, a ZFL-500+ and a SX60-43-S+ in respective order. All amplifiers are manufactured by Mini-Circuits<sup>7</sup> and can be connected via SMA contacts. In Tab. 4.1 the technical specification of the amplifiers are summarized.

position	amplifier	gain at 20 MHz	noise figure	bandwidth
		[dB]	[dB]	[MHz]
1	ZFL-500LN+	28	2.9	0.10-500
2	ZFL-500+	25	4.2	0.05-500
3	SX60-43-S+	24	5.4	0.50- 4000

**Table 4.1:** Overview of the technical specifications of the used amplifiers. The gain was measured at 20 MHz, but the values for noise figure and bandwidth were taken from the corresponding data sheets.

The bandwidth of the amplifier chain has a frequency range from 0.5 MHz to 500 MHz and a total gain of about 77 dB at 20 MHz. To use the full input range of the connected ADC the last amplifier in the chain has to offer at least the corresponding output power. The total noise factor of the amplifier chain can be calculated with Friis equation [Fri44]. Using the noise figure values given in Tab. 4.1 the total noise factor results to  $F = 2.02$ . As expected the noise factor is only slightly larger compared to the noise factor of the first amplifier in the chain ZFL-500LN+ with  $F = 1.95$ . Therefore, it is particularly important to choose an amplifier with a low noise figure as first amplifier in the chain.

## 4.5 dc-SQUID Multiplexer Readout Setup

A schematic of the dipstick setup used for the flux ramp multiplexer readout is shown in Fig. 4.3. This setup is mainly used for testing the developed FRM multiplexer SQUID chips and to optimize the associated flux ramp modulation readout process. To test the multiplex setup efficiently the fast cool-down and warm-up times offered by a dipstick submerged in liquid helium stored in a transport dewar is utilized. The temperature of the liquid helium is constant at the helium boiling temperature  $T = 4.2 \text{ K}$  which lies well below the critical temperature of Nb  $T_c = 9.2 \text{ K}$ . The

<sup>7</sup>Mini-Circuits, P.O.Box 7128 Branson, MO 65615, USA

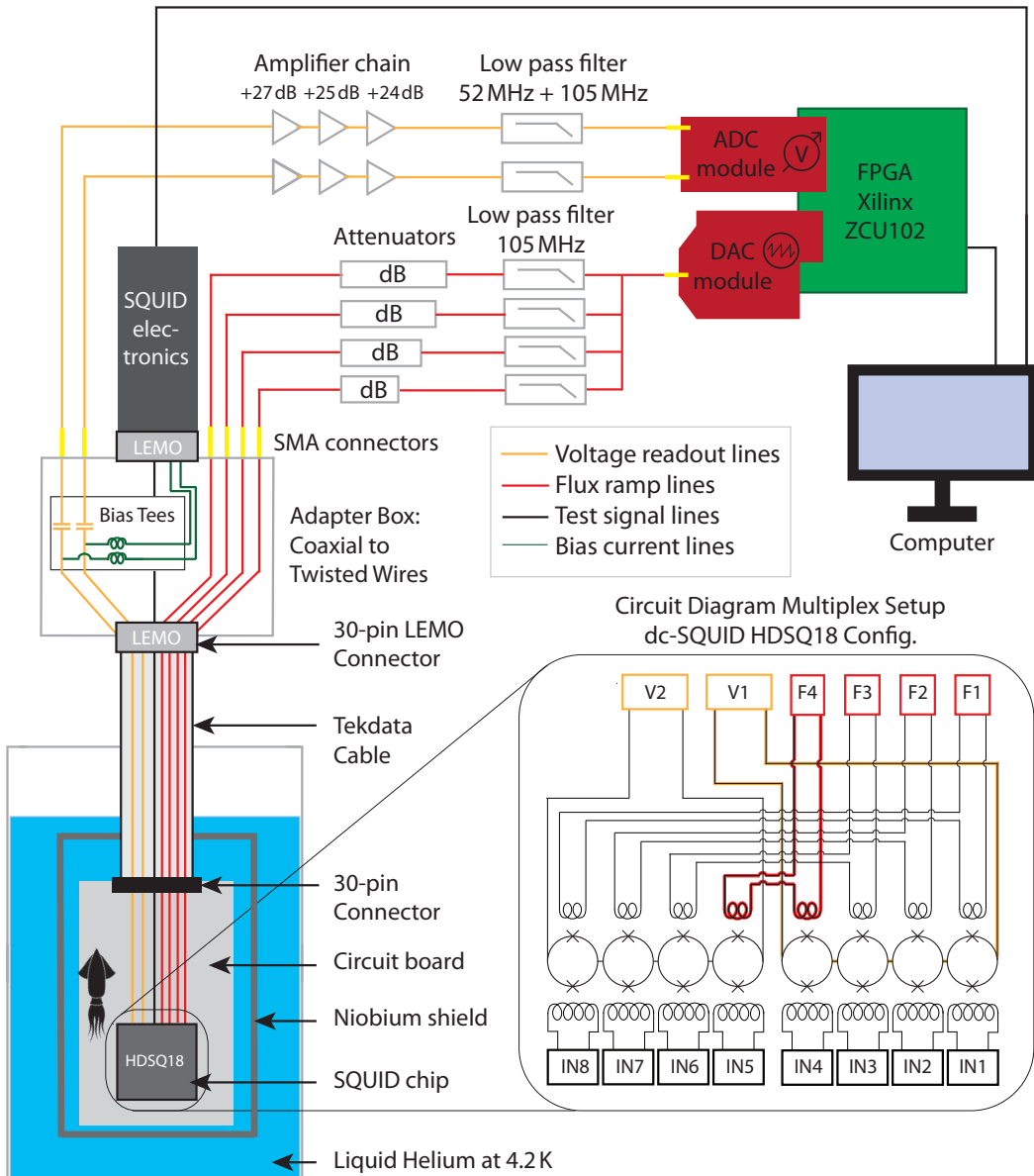


**Figure 4.3:** Schematic illustration of the readout setup, where all different signal paths are color coded. The FRM multiplexer HDSQ18 chip is cooled by liquid helium in a helium transport vessel. The chip is glued to a custom fit circuit board and connected with a SFM-115-01-S-D 30 pin connector to a Tekdata cable implemented in a dipstick. At room temperature the adapter connects the SQUID electronics, FPGA, DAC and ADC for a full operation of the multiplex chip. The electronics are controlled from one computer. In the inset the circuit of the FRM HDSQ18 multiplexer SQUID chip is depicted.

FRM multiplexer dc-SQUID chip is glued to a custom designed circuit board where-to it is connected with aluminum bonding wires. The circuit board is screwed to the dipstick, which has a niobium shield attached for magnetic shielding. One Tekdata cable, which transverses through the dipstick ending in a LEMO connector at the room temperature end of the dipstick, can be connected to the circuit board. To connect the room temperature electronics an rf-shielded custom all in one adapter box was built, which allows for a connection of all room temperature electronic components to the experiment. To apply a bias current to the SQUIDs and to apply test signals to the input coils a commercially available XXF-1 SQUID electronics from Magnicon is used. The flux ramps are generated digitally with a customized Xilinx ZCU102 FPGA and converted to a analog signal with the attached DAC38J84EVM. Overall one generator signal is fed into four separate flux ramp lines, whereby each line contains different attenuators to control the current amplitude of individual flux ramps and a 105 MHz low pass filter VLFX-105+ from Mini-Circuits. The SQUID response of the multiplexer is amplified with the amplifier chain described in section 4.4. Before the signal is converted to a digital signal by the ADS54J69EVM, it passes two low pass filters attached to the ADC module input. These suppress signals above the Nyquist frequency, preventing aliasing during signal sampling by the ADC. The first filter VLF-52+ from Mini-Circuits has a lower cutoff frequency of 52 MHz, but offers only a limited stop band. Therefore, a second low pass filter VLFX-105+ with a lower cutoff frequency of 105 MHz and an upper cutoff frequency greater than 20 GHz is used to extend the stop band into the gigahertz range. The voltage of the multiplexer dc-SQUID is measured via a three wire measurement method. Hereby the ground line is split into two separate wires building a 3-line configuration across the Tekdata cable and circuit board. Both the DAC and ADC evaluation modules are controlled with the FPGAs custom firmware written in Python, where the measurement signals can be read out in real time [Wol20].

The setup can be used without the adapter box by connecting the Tekdata cable directly to the SQUID electronics. This enables to test the functionality of the SQUID chip itself. However it does not allow for high frequency tests as the ac- generator signal frequency limit of the SQUID electronics is 260 Hz. In this work a provisional readout electronics setup was used, as our FPGA boards are currently under reconfiguration. A sawtooth flux ramp signal is generated with a HEWLETT PACKARD 33120A frequency generator and voltage signal is digitized with either a Keysight Infinity Vision Oscilloscope<sup>8</sup> or a SIS3316-DT ADC<sup>9</sup>, which has a maximum sampling rate of about 100 MHz. Although with this setup a contentious readout of the multiplexer is not possible, the functionality new FRM multiplexer chips can still be

---

<sup>8</sup>Keysight Technologies Deutschland GmbH, Herrenberger Straße 130, 71034 Böblingen, Germany

<sup>9</sup>Struck Innovative Systeme GmbH Harksheider Str. 102 22399 Hamburg, Germany

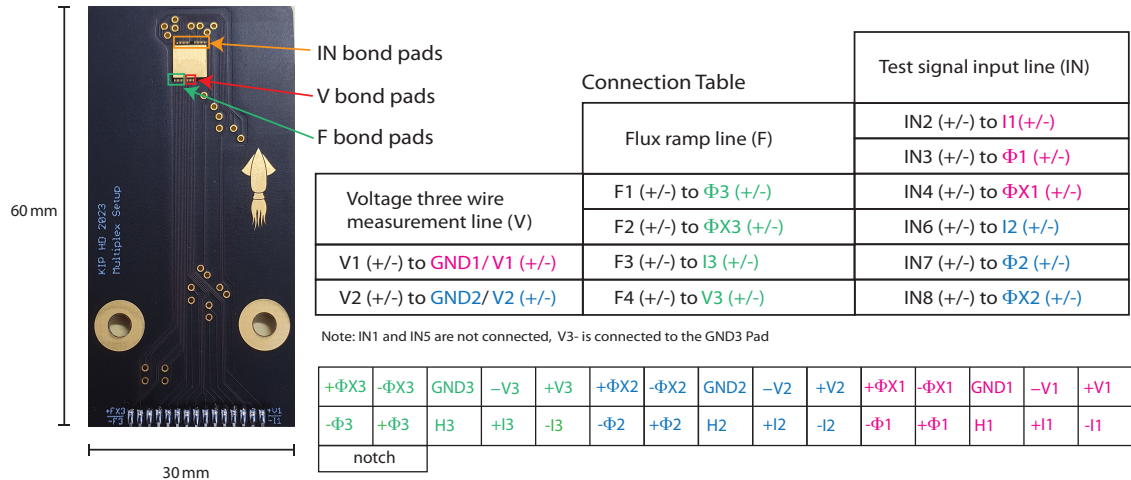


**Figure 4.4:** Multiplexer circuit board for the HDSQ18 2x4 dc-SQUID configuration with 4 flux ramp signals. All connections are to be made with aluminum bonding wires. The three wire voltage measurement connects the two bond pads  $\pm V$  on the chip to three lines on the circuit board corresponding to the voltage lines of channel 1 and channel 2. The IN bond pads are used to connect the input coils of the SQUIDs to apply test signals. Note that IN1 and IN5 are unused, as there is no available transmission line left. The Flux ramp bond pads F are connected to channel 3 of the Tekdata cable. Note that the V3- pad is directly connected to the GND3 pad to allow for a two wire transmission.

demonstrated. In the flowing the circuit board and the adapter box are described in more detail.

### Multiplexer Circuit Board and Adapter Box

The circuit board including the wiring diagram is shown in Fig. 4.4, whereby the naming refers to our standard Tekdata scheme as shown in [All17]. This board is specially adapted for the HDSQ18 design and allows a 1:1 bonding from the bond pads to the board. It is a 2-layer board with a total thickness of 1 mm containing a top and bottom layer of copper, solder resist and a chemical gold finish for open surfaces. As the circuit board consists mostly of large connected copper areas it is thermally well coupled to the environment provided that metal screws are used to fix it onto a metal surface. This provides a proper cooling of the SQUIDs in a cryogenic environment and the board is therefore compatible for usage in a cryostat. The circuit board allows a three-wire measurement for the voltage readout of two SQUID channels. All other lines are routed with only two wires. The board can be connected via a 30 pin connector with a Tekdata cable with SFM-115-01-S-D 30 pin connectors. The wiring plan is chosen such that the SQUID electronics can be connected directly to the Tekdata cable which allows testing of the functionality of

the SQUID chips and quick sanity checks. Note that on the circuit board no special high frequency transmission line configuration is chosen. The reason being that the measurements conducted with this circuit board allows a better comparison with the planned detector readout setup.

The adapter connects the SMA coaxial cables to twisted wires of the Tekdata cable and the SQUID electronics. Most connections are direct and realized by self made twisted pairs with a pitch of 2 mm out of CuNi<sub>2</sub> with thickness 0.2 mm, which matches the Tekdata cables. The voltage transmission lines connection include a ZX85-12G-S+ BIAS-TEE from Microcircuits. The BIAS-TEE allows a dc-current injection to bias the SQUIDs through the voltage transmission line. Therefore, a dc-current source from the SQUID electronics is used. Hereby the BIAS-TEE completely blocks the dc-current in readout direction, such that the dc-bias current does not influence the voltage measurement. The bandwidth of the BIAS TEE reaches from 0.2 to 12 000 MHz.

## 4.6 Cryostat Setup for the Readout of the maXs20-256-16

The main goal of this thesis was to conceptualize a setup for the readout of the maXs20-256-16 16 × 16 pixel MMC array [Abe25] (maXs256). In this section the components of the novel readout scheme are discussed. The schematic illustration in Fig. 4.5 shows the components for the here conceptualized readout scheme utilizing a 4 × 32 dc-SQUID multiplexer array. Overall the setup is similar to the above presented dipstick setup. In order to readout 32 voltage lines at least 8 ADCs are required in combination with 8 Xilinx ZCU102 FPGA boards, as one of these ADCs can maximally host 4 voltage measurement lines and each FPGA can only be connected to one ADC of this type. The flux ramp signal is generated by a single DAC connected to one of the FPGA boards. For a correct readout, an additional master synchronization line connecting all boards is needed, such that the flux ramp signal is triggered correctly.

For the cryostat 8 (V)-adapters, as visualized in Fig. 4.5, connecting the voltage lines are needed. These allow to connect the SMA room temperature wiring to the TEC-DATA cables of the cryostat and a SQUID electronics for bias current injection via BIAS TEEs, as described in section 4.5. In Fig. 4.5 not all of them are explicitly shown, but they are indicated by the three dots inbetween two (V)-adapters. The multiplexed SQUID responses are amplified with the amplifier chain described in section 4.4. In total the setup contains 32 of these amplifier chains. All amplifiers are connected to a low noise current source device able to connect all 96 devices. The amplifiers are placed and connected on a large copper block, whereby the cables are additionally shielded. A clean current source for the amplifiers is especially im-

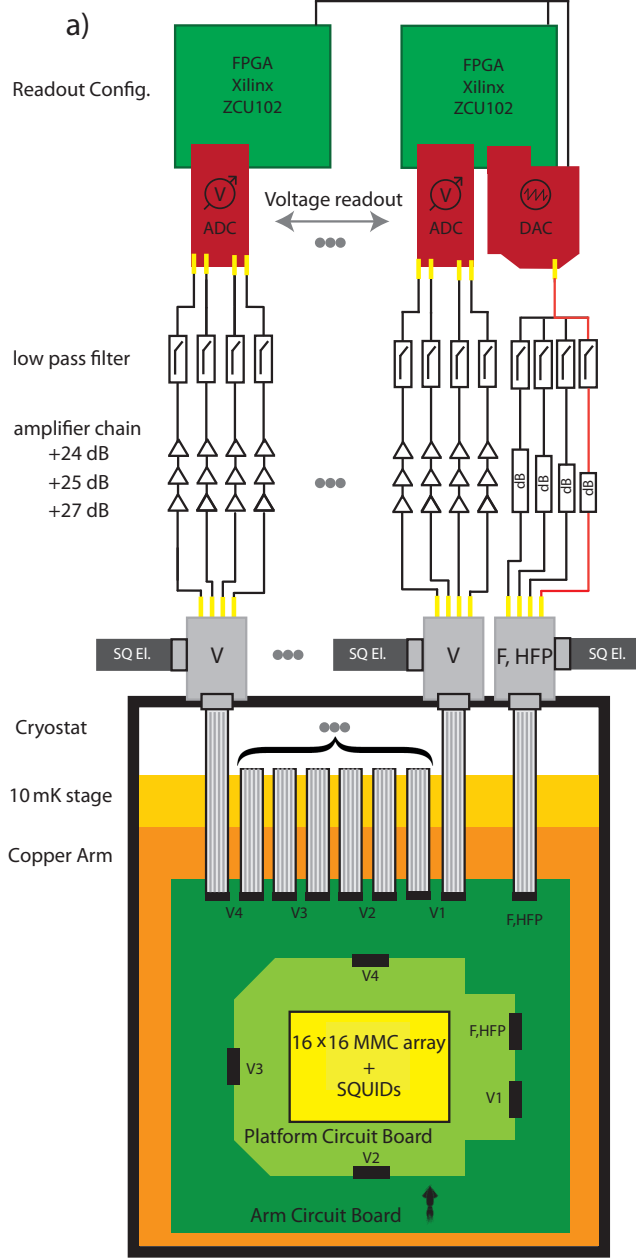


**Figure 4.5:** Schematic illustration of the readout setup for the maXs256 in the Cryostat. The maXs256 is installed on a copper holder [Abe25]. The SQUIDS are placed on a separate adjacent copper platform and the SQUIDS are surrounded by the platform circuit board. The copper holder of the arm is mounted to the mixing chamber platform of the cryostat. For the readout of the full 4x32 multiplexer 9 TEC-DATA cables are connected to the arm circuit board. Here 1 TEC-DATA cable transmits the flux ramps (F) and the detector feed lines (HFP) and the other 8 the SQUID readout lines (V). Adapter boxes are required to connect an SQUID electronics for the power supply of the SQUID and the room temperature coaxial cables via SMA connections. Some of the 32 voltage lines are abbreviated with three large dots in the illustration. A total of 8 FPGA boards with 8 ADCs and 1 DAC are required for the complete readout.

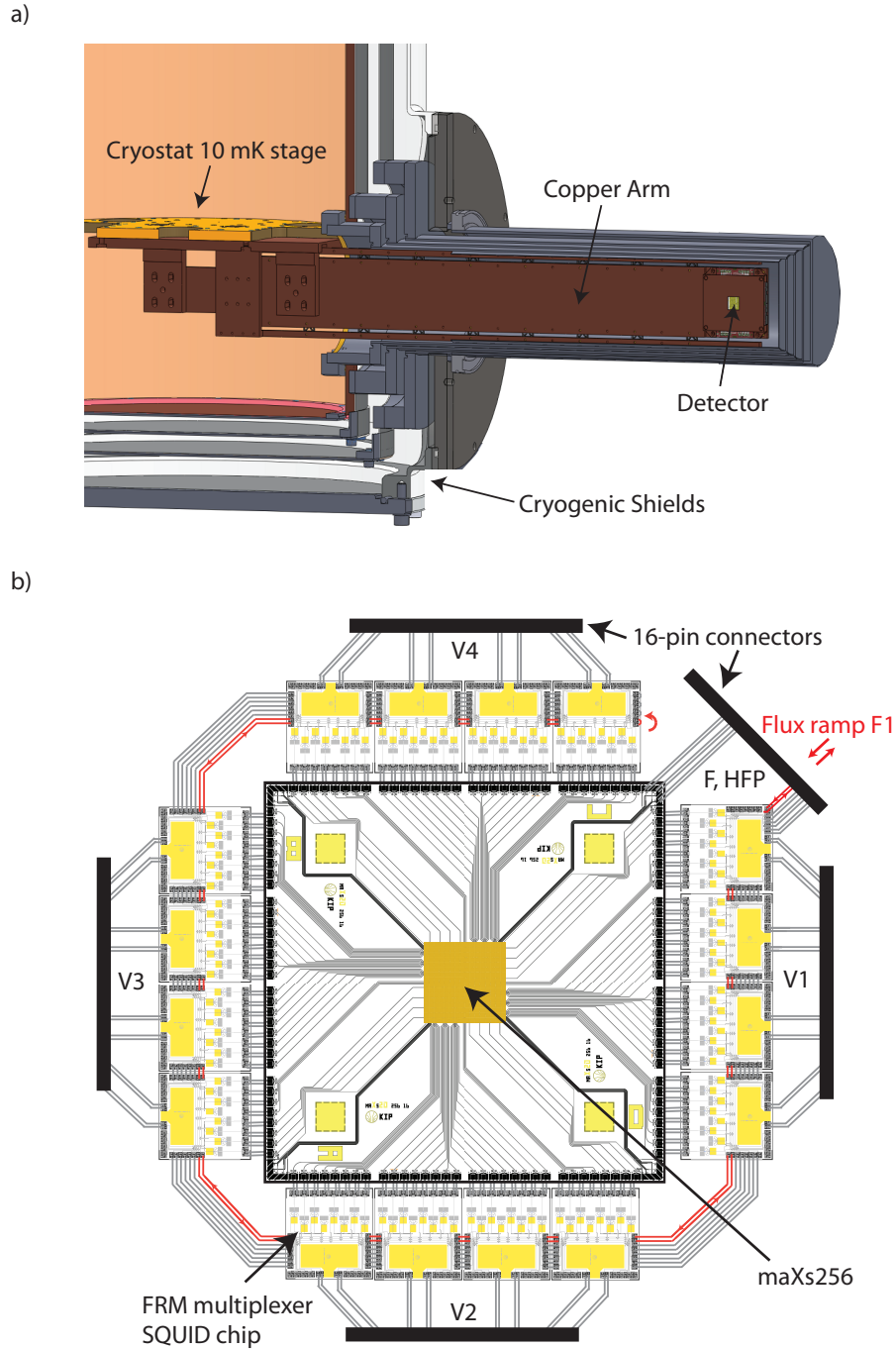


**Figure 4.6:** Schematic illustration of the 4x32 dc-SQUID multiplexer readout setup for the maXs256 in the cryostat. a) Shows our arm construction mounted at the side of the cryostat. The arm is attached to the mixing chamber platform with a copper mounting. The detector is located at the end of the arm. Illustration by Daniel Hengstler. b) Shows the layout of the maXs256 detector chip together with 16 dc-SQUID multiplexer chips arranged around it. The F1 flux ramp line in red, highlights the connection of the flux ramps.

portant as the entire noise of the multiplexer can be dominated by noise introduced from the current source. The additional shielding of the current source lines reduces the cross-talk to the signal lines. Again a low pass filter is used to suppress high frequency noise. The additional adapter, which is indicated in Fig. 4.5 as (F, HFP) connects the 4 flux ramps and the detector. Here the single F abbreviates flux ramps and HFP is an abbreviation for heater (H), field (F) and pulser (P) needed for the maXs256 detector operation [Abe25]. The current signals for the HFP are provided by the SQUID electronics. In the same fashion as before, the flux ramp line is split into four separate lines where each line is attenuated by a different factor and low pass filters are applied.

In order to provide the maXs256 detector with a radiation source a special arm setup mounted to the 10 mK stage of a BlueFors cryostat<sup>10</sup> as shown in Fig. 4.6 a) is used. Here the detector is placed on a copper block on the end of the arm. Our 2x4 multiplexer dc-SQUID chips are placed on the same copper block in the direct vicinity of the detector chip from where they are directly bonded to the detector platform circuit board and to the maXs256 detector via aluminum bonding wires. In Fig. 4.6 b) the readout configuration of the maXs256 detector bonded to 16 multiplexer dc-SQUID chips connected in a 4x32 multiplex array configuration is shown. The detector is connected with the HFP lines. The four flux ramp lines are connected to one of the SQUID chips. As can be seen more clearly in the full circuit diagram in Fig. 4.7, all flux ramp lines are connected from chip to chip. On the last chip in line the F+ and F- bondpads are connected and the current runs again trough all chips completing the on-chip strip lines. One flux ramp path is colored in red to visualize how these chips are connected. Note that in Fig. 4.6 and Fig. 4.5 the corresponding flux ramp line is colored in red as well. The detector platform circuit board is connected to the arm circuit board which acts as a cable extension to fit in all lines in the arm of a cryostat. Onto this board the Tekdata cables are connected.

---

<sup>10</sup>Bluefors, Oy Arinatie 10 00370, Helsinki, Finland

#### 4. dc-SQUID Flux Ramp Modulation Setups

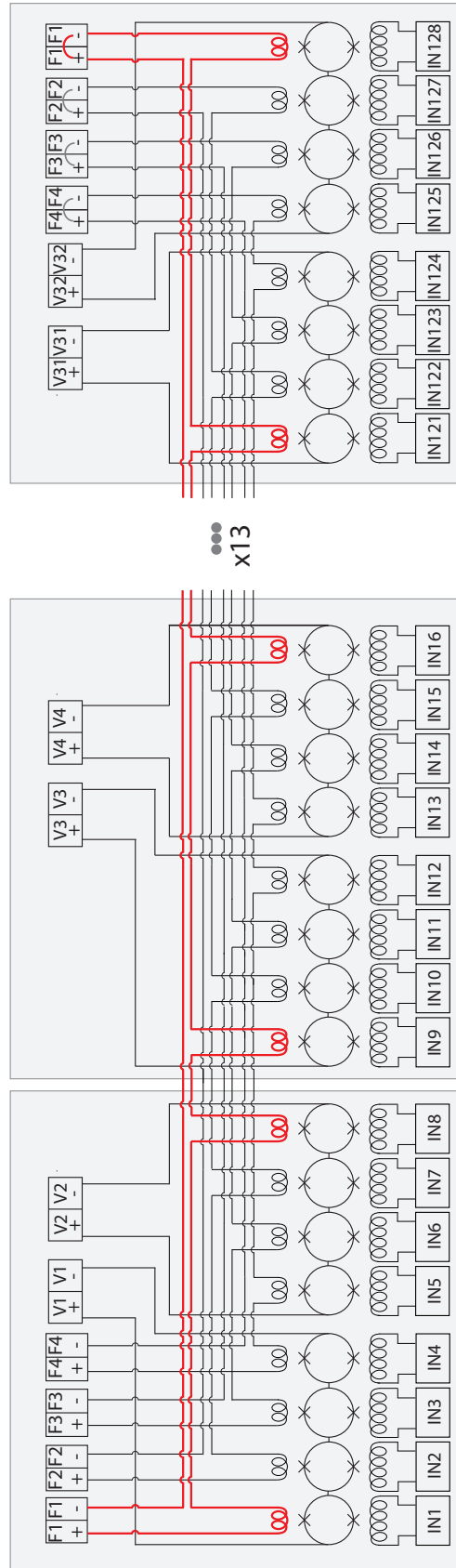


**Figure 4.7:** Schematic of the 4x32 multiplexer flux ramp modulation circuit. The light gray areas indicate one 2x4 multiplexer dc-SQUID chip. The numbered IN bondpads from 1 to 128 correspond to the detector channels, the numbered V bondpads from 1 to 32 correspond to the voltage measurement and bias current injection of one dc-SQUID array of length 4 and the number of F bondpads from 1 to 4 correspond to the flux ramp lines. The F1 flux ramp line is marked in red to indicate a full path of the flux ramp line. All chips share the same flux ramp line, as they are connected together. At the end of the path the bondpads F1+ and F1- have to be connected and the ground line transverses back a similar path such that the on chip transmission line builds at all parts a strip line configuration.

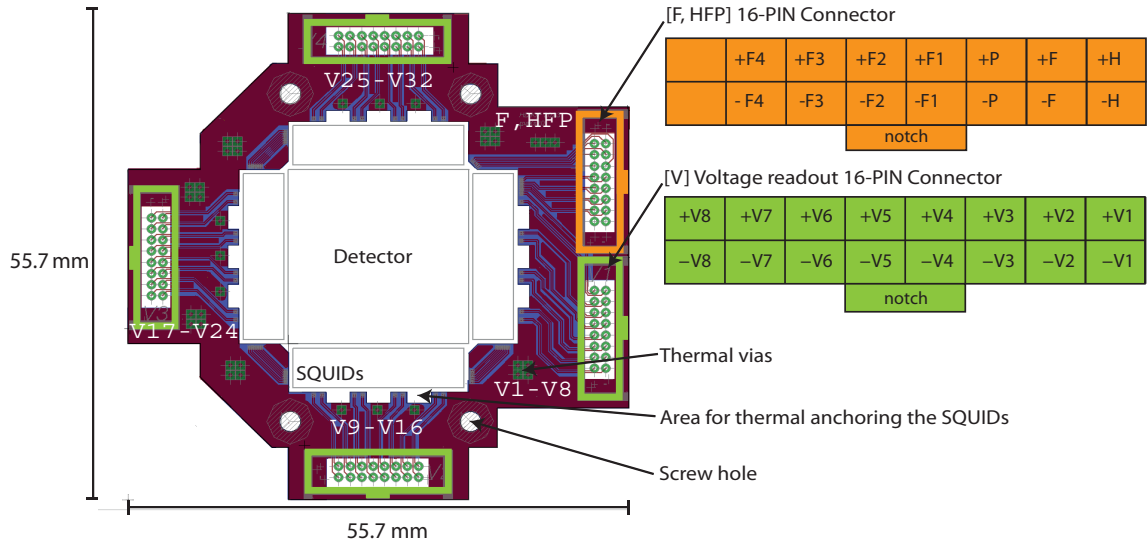


**Figure 4.8:** Layout of the detector platform circuit board and the 16-pin connector schemata. The box in the middle indicates the detector position and the four boxes around indicate the SQUID positions. The free areas around the SQUIDs can be used for a gold bond connection to the copper platform beneath for thermal anchoring the SQUID chips. All voltage lines are in a two wire configuration directly connected to a 16-pin connector [V]. There are in total four 16-pin connectors for the voltage measurements. The four flux ramp lines and detector heater H, field F and pulser P are connected with a two wire parallel line configuration to the [F,HFP] 16-pin connector. The outer dimensions of the platform are specified by our arm configuration [Abe25] of the cryostat.

## Detector Platform and Detector Arm Circuit Boards

In Fig. 4.8 a) the layout of the detector platform circuit board is depicted. It includes 2 copper layers on the top and backside, with a chemical gold finish for the solder stop resist free areas. It has a total thickness of 1 mm and both copper layers are connected with thermal vias at several points. Therefore it is expected to be thermally well anchored to the cryostat. The board has a total of four 16 pin connectors to connect the voltage lines of the 32 SQUID arrays. All lines are in a two pair configuration, such that the three wire measurement starts only after this board. The additional 16 pin connector F, HFP carries the 4 flux ramp lines for the SQUID modulation as well as the heater H, field F and pulser P lines for the operation of the MMC detector. The corresponding diagram of the F, HFP 16 pin connector is shown in Fig. 4.8 b). Here we are limited by the outer dimension specified by our arm configuration [Abe25] of the cryostat. Thus a completely new arm design would be required to gain additional space. Since the detector and the SQUID chips also have larger dimensions than previous detector setups of our research group, there is no space on this board for an elaborated wiring scheme or special types of transmission line routing. Especially due

to the lack of space no vias can be used for a line crossing as to technical limitations in board manufacturing. However, the three-wire measurement starts directly on the arm circuit board, which is connected modularly to this board.

The detector arm circuit board connects the detector platform to the 30 pin Tekdata cables. As of the writing of this thesis three different versions of this circuit board are conceptualized. First a very short version, which is intended for testing purposes to function as an adapter to the detector platform, such that we can experiment with a smaller setup taking up less space in the cryostat allowing other experiments to be conducted in parallel. The other 2 arm circuit boards are full scale and compatible with the whole detector setup. In one version a 2-layer circuit board was designed, whereby all transmission lines are in a parallel configuration. In the other version a 4-layer circuit with an elaborate line scheme combining a large ground plane and a coplanar waveguide was designed. In Fig. 4.9 the 2-layer version featuring a simple line configuration is shown. All lines are directly connected as indicated in the connection scheme, e.g. the entire voltage line connection scheme can be taken out of the green tables marked with [V] where to all 32 SQUID channels are mapped. All voltage lines are connected to a triple twisted pair wire of the Tekdata cable. As one Tekdata cable features 4 triples as shown previously in Fig. 4.1 we need a total of 8 Tekdata cables for the full voltage measurement readout of the  $4 \times 32$  multiplexer. The F, HFP lines are connected to a separate Tekdata cable. The HFP lines are connected to twisted pairs whereas the 4 flux ramp lines are connected to twisted triples. Note that all transmission lines of the boards are superconducting, to avoid additional heating of the cryostat due to the electrical resistance.

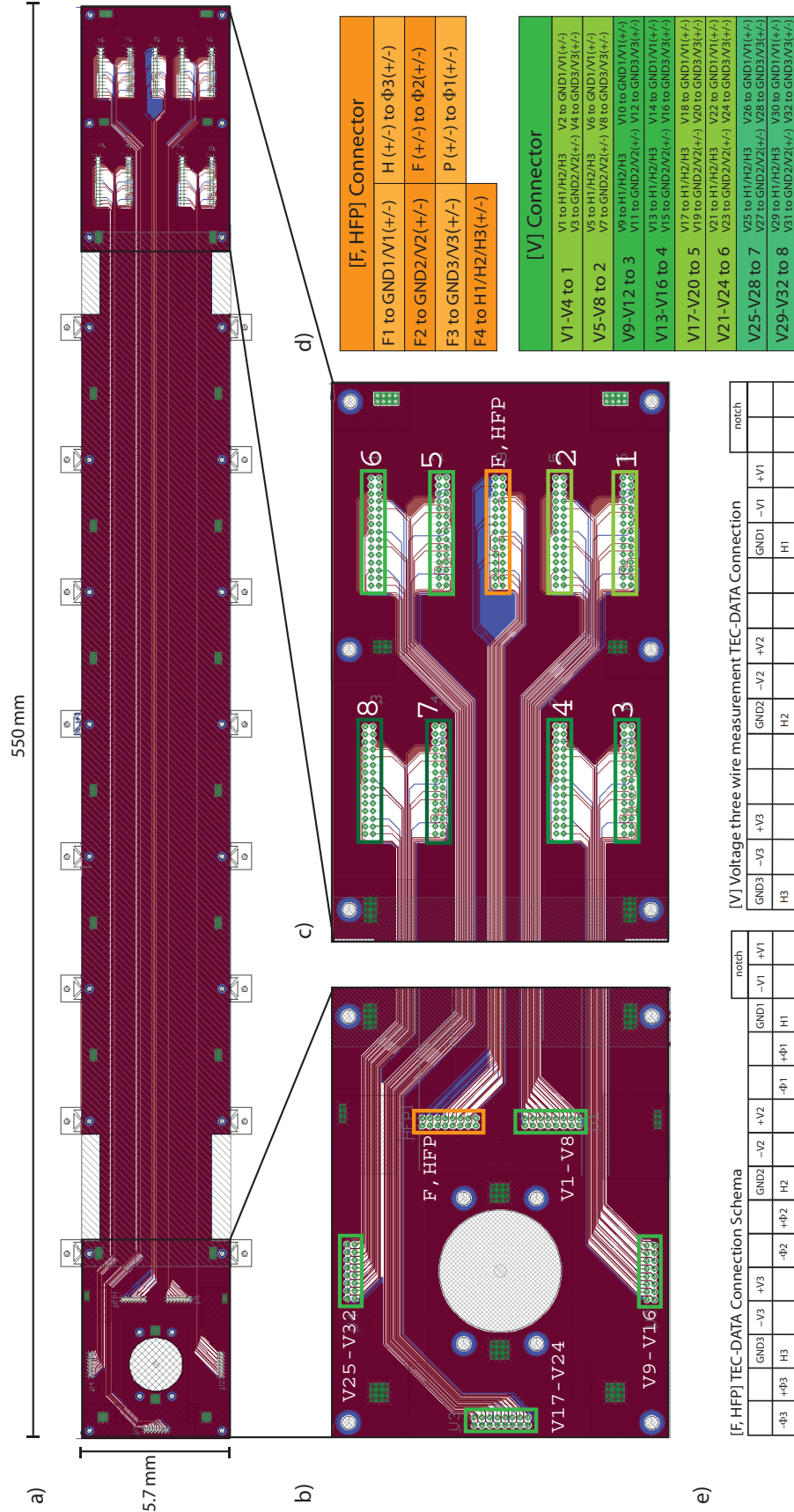


**Figure 4.9:** a) Layout of arm circuit board, b) zoom into detector side end, c) zoom into cryostat side end. The detector platform circuit board is mounted directly onto the arm circuit board, as the 16-pin connector position overlap. The dimensions are specified by our arm configuration of the cryostat. d) Orange table for the flux ramp line and detector connection and the green table for the voltage readout connection. e) [F,HFP] Tekdata connection schema and the [V] Tekdata connection schema the entire wiring of the detector in the cryostat can be inferred. The flux ramp lines and the voltage lines are in a three wire configuration, whereby the ground wire is split into two separate lines allowing a three wire measurement and heat input reduction.



## 5. Experimental Results

In this chapter experimental results obtained within this work are discussed. Mostly devices from the wafer with the internal name HDSQ18bw1 (HDSQ18b), which was fabricated within the framework of this thesis, are investigated. First, the results of the characterization of the single dc-SQUIDs are presented. This includes the *IV*-characteristics of the first window-type Josephson junctions produced with a tri-layer from our PREVAC sputtering systems. Furthermore the characterization of single dc-SQUIDs and the noise at mK-temperatures obtained using a cross-correlation method are discussed. Moreover the temperature dependent white noise behavior was investigated comparing the HDSQ18 dc-SQUID design with Au cooling fins to our previous SQUID design [Bau22] with AuPd cooling fins. Finally the functionality of the new FRM multiplexer dc-SQUIDs chips developed within this thesis is showcased and the results are discussed.

### 5.1 Characterization of the HDSQ18b single dc-SQUIDs

In order to fully characterize the FRM dc-SQUID multiplexer, a comprehensive investigation of the individual dc-SQUIDs used in it is required. Therefore in the following the characteristic properties of the single SQUIDs are discussed.

#### 5.1.1 PreVAC-Window Type Josephson Junction

The SQUIDs from the HDSQ18b wafer were fabricated according to the fabrication process described in section 3.3.1. In this process the in-situ sputtered tri-layer structure was deposited from our PREVAC sputtering system. As the PREVAC sputtering system is newly installed in our cleanroom, the process parameters for the sputter deposition have to be optimized, to obtain high quality Josephson junctions. To control the quality of the sputter deposited Nb-films during the optimization process, the critical temperature of the films was measured with the MPMS-XL5 SQUID-magnetometer. Here the film sample is slowly cooled down in a weak external magnetic field while the magnetization of the sample is monitored with a SQUID. Due to the Meißner-Ochsenfeld effect the superconducting phase transition is indicated by the sudden change in magnetization of the sample in a magnetic field. A high Nb film quality is indicated by a measured critical temperature close to the bulk critical temperature of  $T_c = 9.25\text{ K}$ . In total the critical temperature for over 10 different films was measured. The critical temperature obtained for the Nb-film sputtered with

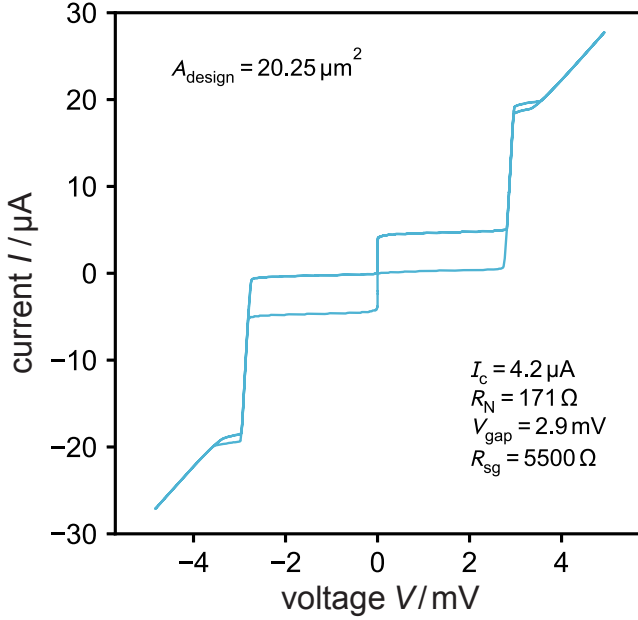


**Figure 5.1:** Chip 2A02 from the HDSQ18b wafer, unshunted window-type Josephson junction with designed area of  $A_{\text{design}} = 20.25 \mu\text{m}^2$ . The characteristic parameters determined from the data; critical current  $I_c = 4.2 \mu\text{A}$  normal resistance  $R_N = 171 \Omega$  subgap resistance  $R_{\text{sg}} = 5500 \Omega$  and gap voltage  $V_{\text{gap}} = 2.9 \text{ mV}$ .

the optimum parameters is  $T_c = (9.2 \pm 0.1) \text{ K}$ . In addition to the measurements of the critical temperature, wafer scale film stress tests were conducted and used for the optimization of the Nb-films [Sto23].

The oxidation parameters of the Al-film were inferred from the empirical relation between the critical current density  $J_c$  of the tri-layer and the oxygen exposure  $(t_{\text{ox}} p_{\text{ox}})^{-\kappa}$ . Here the exponent  $\kappa$  needs to be experimentally determined for the specific sputtering system used [Kem13]. Although the statistics of the tri-layer from the PREVAC system is small at the time of the window type tri-layer production, first test indicate that the parameters behave comparable to a different sputtering system of our cleanroom [Sto23]. Therefore, we expect that the critical current/oxidation parameter dependence reported in [Bau22] should yield promising junction also in the PREVAC system. Therefore, an oxygen exposure  $t_{\text{ox}} p_{\text{ox}} = 2.4 \times 10^8 \text{ Pa} \cdot \text{s}$  was used for the production of the window type junctions, which results in a designed critical current density of  $J_c = 0.26 \mu\text{A}/\mu\text{m}^2$  at zero temperature.

Within this work the  $IV$ -characteristics of unshunted window type Josephson junctions were measured using the experimental setup described in [Geh23]. In Fig. 5.1 the  $IV$ -characteristics of such a junction with a designed area of  $A_{\text{design}} = 20.25 \mu\text{m}^2$  from the test chip 2A02 of the HDSQ18b wafer is shown. The dimensions of the shown junction coincides with the junction dimensions used for the dc-SQUIDs of this wafer. For the critical current we measure  $I_c = (4.2 \pm 0.4) \mu\text{A}$  at  $T = 4.2 \text{ K}$ , whereby the uncertainty is calculated from the standard deviation obtained from three different junction measurements. With an expected critical current of  $I_c = 5.0 \mu\text{A}$  at  $T = 4.2 \text{ K}$  [Kah24]??, the measured  $I_c$  is slightly below targeted value. The gap

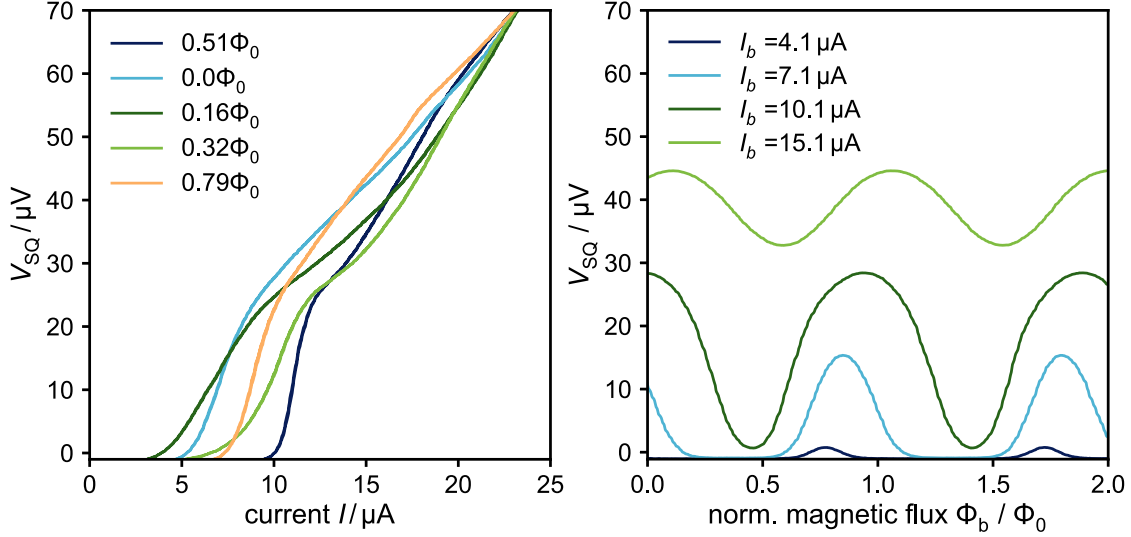


**Figure 5.2:** dc-SQUID characteristics of the chip 2C10 from HDSQ18b measured at  $T = 4.2\text{ K}$  a)  $IV$ -characteristics for different values of the magnetic flux b)  $V\Phi$ -characteristics for different bias currents  $I_b$ .

voltage  $V_{\text{gap}} = (2.9 \pm 0.1)\text{ mV}$  lies within the expected range of between  $2.83\text{ mV}$  to  $2.93\text{ mV}$  and the subgap resistance to normal resistance ratio  $R_{\text{sg}}/R_{\text{N}} \approx 32$  indicates the high quality of the junction. Also the expected proximity effect can be observed. Overall we succeeded in producing high quality window type junctions based on the tri-layer from the PREVAC, whereby the quality is comparable to the window type junctions from other sputter deposition systems [Bau22].

### 5.1.2 Characteristic quantities of the HDSQ18b dc-SQUIDs

Next the measured values of the characteristic quantities of the single dc-SQUIDs of the HDSQ18b wafer are discussed. In the framework of this thesis 9 single dc-SQUIDs across 6 different chips were characterized at a temperature of  $T = 4.2\text{ K}$ . Further the noise of a single SQUID on the chips 2C10 and 2D02 was investigated at mK-temperatures. The  $IV$ -characteristics of a single SQUID on the chip 2C10 is shown in Fig. 5.2 a) for different values of the magnetic flux. In Fig. 5.2 b) the  $V\Phi$ -characteristics of the same SQUID are shown for different bias currents. The maximum peak to peak voltage is found between the two limiting  $IV$ -curves at values of the magnetic flux  $\Phi = n\Phi_0$  and  $\Phi = (n+1/2)\Phi_0$ . Other curves of in-between magnetic flux can cross these two limiting cases, where a crossing indicates a resonance. Also, as expected for an asymmetric bias current injection, the  $V\Phi$ -characteristics shifts in  $\Phi$  direction for different bias currents [Ueh93]. The positive and negative slopes are not equivalent of the here not shown  $I\Phi$ -characteristics. Therefore, the quantities  $I_{\Phi+}$

**Table 5.1:** Overview of the mean values obtained from the characterization of 9 dc-SQUIDS of the HDSQ18b wafer. The uncertainty is calculated from the standard deviation.

$I_b$ [μA]	$V_{\max}$ [μV]	$M_{\text{in}}^{-1}$ [μA/Φ₀]	$M_{\text{mod}}^{-1}$ [μA/Φ₀]	$V_\Phi$ [μV/Φ₀]	$I_{\Phi-}$ [μA/Φ₀]	$I_{\Phi+}$ [μA/Φ₀]
$10.8 \pm 0.9$	$26.4 \pm 0.9$	$6.3 \pm 0.1$	$40.4 \pm 0.7$	$112 \pm 10$	$25 \pm 5$	$10 \pm 3$

and  $I_{\Phi-}$  describing the current to flux transfer coefficients at the steepest point of the positive and negative slope respectively. For all SQUIDS the optimal bias current  $I_b$  with corresponding maximal peak to peak voltage  $V_{\max}$ , the transfer coefficients, the mutual inductance between the input coil and SQUID-loop  $M_{\text{in}}$  and the mutual inductance between the modulation coil and SQUID-loop  $M_{\text{mod}}$  were determined. In Tab. 5.1 the mean values of the measured SQUID properties with corresponding uncertainties calculated from the standard deviation are summarized. The deviation between the different SQUIDS on the wafer is small, whereby the largest deviations occur from SQUIDS that originate from the edge area of the silicon wafer. As an example the SQUID from the chip 2D02 from the border area has an optimal bias current of  $I_b = 12.8 \mu\text{A}$ . All tested SQUIDS work as intended, which overall speaks for a high quality of the fabricated wafer.

### 5.1.3 Noise of the single dc-SQUIDS at mK-temperatures

To measure the noise of the dc-SQUIDS on the HDSQ18b-wafer a cross correlation setup, described in [FS24], was used. Hereby a single dc-SQUID is operated in a voltage bias with the use of a gain resistance of  $R_g = 300 \text{ m}\Omega$ , whereby the bias current stems from the generator abbreviated with  $I$  of a XXF-1 SQUID electronics. For all noise measurements within this thesis a fixed bias current of  $I_b = 22 \mu\text{A}$  was chosen. The working point from the single dc-SQUID, which is operated in the open loop mode, was chosen at a steep non ambiguous point of corresponding  $I\Phi$ -characteristics. Two 16 cell dc-SQUID arrays operated in a flux locked loop both obtain the signal from the single dc-SQUID. With known mutual inductances and feedback resistor of the arrays the current to flux transfer coefficient from the single SQUID to the respective array were determined in order to obtain the correct noise level of the single SQUID. The two voltage signal time traces from the arrays are measured, stored to disk and then cross correlated [Rub10] leaving only the correlated noise. In Fig. 5.3 the cross-correlated spectrum showing the square root of the magnetic flux noise power spectral density  $\sqrt{S_\Phi}$  plotted against the frequency  $f$  is presented for a single dc-SQUID on the chip 2C10 of the HDSQ18b wafer. The shown measurement was conducted at cryostat temperatures below 10 mK utilizing

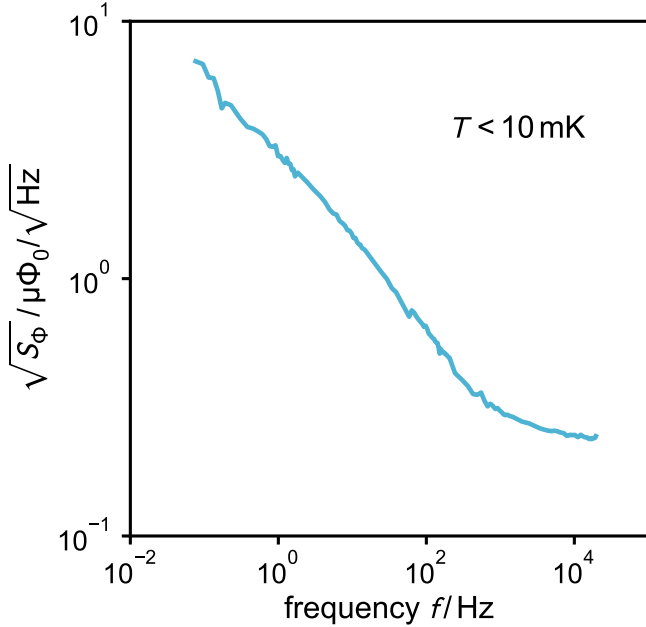


**Figure 5.3:** Square root of the magnetic flux noise power spectral density of a single dc-SQUID on the chip 2C10 of the HDSQ18b wafer. This spectrum was obtained at cryostat temperatures below 10 mK through a cross-correlation utilizing two dc-SQUID arrays with the internal name HDSQ15w3 4B22.

two dc-SQUID arrays with the internal name HDSQ15w3 4B22. A numerical fit of the noise spectrum was done utilizing a function of the form  $S_\Phi = S_{\Phi,w} + S_{\Phi,1/f}(1/f)^\alpha$ . The data gives for the white noise level  $\sqrt{S_{\Phi,w}} = 0.23 \mu\Phi_0/\sqrt{\text{Hz}}$  and for the  $1/f$ -noise  $\sqrt{S_{\Phi,1/f}} = 3.0 \mu\Phi_0/\sqrt{\text{Hz}}$  at 1 Hz with  $\alpha = 0.65$ . Additionally to the shown noise spectrum three other SQUIDs, HDSQ17w1 3C09 with AuPd cooling fins, HDSQ17w1 2A02 with Au cooling fins and lossy lines [Kah24] and HDSQ18b 2D02, were cross-correlated at mK-temperatures with the intent to investigate the single SQUID operating temperature. Overall the  $1/f$  and white noise of the other SQUIDs are very similar to the shown spectrum. As these SQUIDs are of the same type with similar design parameters this result is to be expected.

## 5.2 White Noise versus Temperature

In order to investigate the temperature dependent white noise of our SQUIDs and to investigate the impact of the change from AuPd to Au cooling fins, the white noise versus cryostat temperature behavior is investigated. In Fig. 5.4 the white noise magnetic flux power spectral density  $S_\Phi$  is applied against the cryostat temperature  $T$  for two representative data sets HDSQ17w1 3C09 with AuPd cooling fins and HDSQ18b 2C10 with Au cooling fins. The data points were obtained by cross correlating the measured voltage time traces of the two arrays and numerically fitting the flux noise  $\sqrt{S_\Phi}$ , utilizing the added noise function from the  $1/f$  noise contribution (2.50) and the white noise contribution, extracting the white noise level at each temperature.

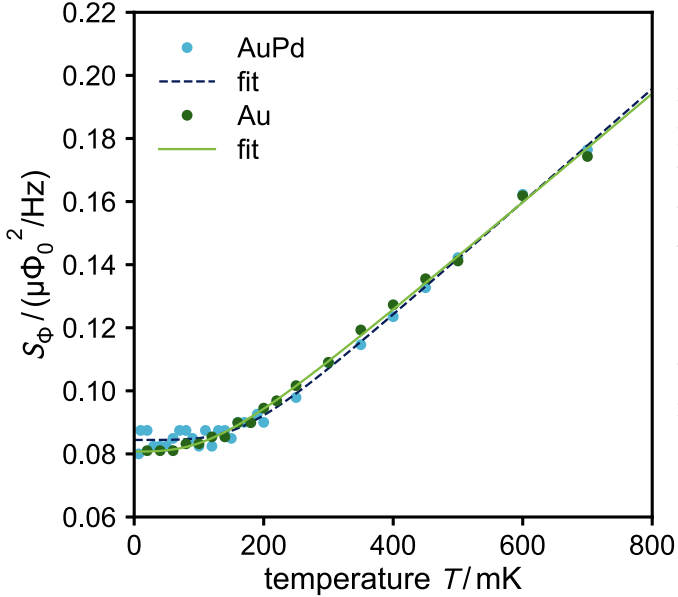


**Figure 5.4:** White noise magnetic flux power spectral density  $S_\Phi$  applied against the cryostat temperature  $T$ . Here two representative data sets are shown: HDSQ17w1 3C09 with AuPd cooling fins and HD-SQ18b 2C10 with Au cooling fins. The data was fitted with the function  $A(T_{\min}^{n+1} + T^{n+1})^{\frac{1}{n+1}} + c$  with the fit parameters  $A$ ,  $T_{\min}$ ,  $n$  and  $c$ .

To verify the fit values for the white noise for all obtained spectra the noise level at frequency  $f = 3 \times 10^4$  Hz was read out, whereby the values obtained from the fit coincided within a small margin of error. Overall the uncertainty on the data points shown can be estimated with the scattering of the data points in the plateau region from reaching from 10 mK to 100 mK, where a nearly constant white noise contribution is observed. From the standard deviation of the HDSQ17w1 3C09 data the uncertainty on the data points flows  $S_{\Phi,\text{err}} = 0.01 \mu\Phi_0^2/\text{Hz}$ . In addition a small unknown systematic error on the shown data can occur, resulting from the uncertainty of the measured mutual inductances and the current to flux transfer coefficient from the single SQUID to the array. As these factors are to be multiplied by the obtained  $\sqrt{S_\Phi}$  the data shown in  $S_\Phi$  is shifted influencing the overall distribution of data non linearly.

Looking at Fig. 5.4, it is eminent that both share a similar noise plateau indicating a similar operating temperature. As the noise level rises similarly for both SQUIDs with the cryostat temperature, it indicates that the thermal bottleneck for both systems coincides. To further analyze a function of the form  $A(T_{\min}^{n+1} + T^{n+1})^{\frac{1}{n+1}} + c$  was fitted, as discussed in section 2.6.3. Here  $A$  is a constant prefactor converting the temperature to the magnetic flux noise spectral density,  $c$  a constant for the offset of temperature independent flux noise, e.g. the noise of the current source,  $T_{\min}$  the minimal operating temperature of the dc-SQUID,  $n$  the exponent hinting at the nature of bottle necks thermal transfer process and  $T$  the cryostat temperature. The results from the fit on the investigated SQUID can be taken from Tab. 5.2. As both SQUIDs share the same specs besides the cooling fins we expect a similar  $A$  and  $c$ , which are both given. The minimal temperatures are also close to each other, whereas

**Table 5.2:** Overview of design target values for properties of the dc-SQUIDs produced within the framework of this thesis. In order to obtain the inductance and mutual inductances values the simulation programm InductEX were used.  $I_c$  and  $R_s$  follow from the requirements imposed on  $\beta_L$  and  $\beta_C$ .

Chip	Fin	$A$ [ $\mu\Phi_0^2/\text{Hz K}$ ]	$T_{\min}$ [mK]	$n$	$c$ [ $\mu\Phi_0^2/\text{Hz}$ ]
HDSQ17w1 3C09	AuPd	$0.179 \pm 0.009$	$184 \pm 19$	$3.1 \pm 1.2$	$0.050 \pm 0.005$
HDSQ18b 2C10	Au	$0.174 \pm 0.007$	$149 \pm 18$	$1.8 \pm 0.7$	$0.050 \pm 0.005$

the fit gives slightly lower values for the SQUID with the Au cooling fins. However due to the large scattering of the data points both temperatures are to be considered nearly equal. The  $n = 2$  indicates that a metallic link is the thermal bottleneck of the system, which would coincide with our expectations. From the calculations in section 3.2.1 a drastic change in operating temperature of the SQUIDs is not expected, as the thermal bottleneck is most likely to be attributed to the small thermal link. The slightly higher  $n = 3.1 \pm 1.1$  found for the SQUID with the AuPd cooling fins might indicate a small influence of higher order thermal transport processes, as e.g. the hot-electron effect. However due to the large uncertainty of the fit parameters the consensus cannot yet be taken as a definitive statement.

### 5.3 HDSQ18b FRM dc-SQUID Multiplexer

Finally the results from selected representative measurements of the FRM dc-SQUID multiplexer chips developed within this thesis are discussed. In total 6 chips, 3 of both multiplexer chip types, from the HDSQ18b wafer were characterized. As the results for both types and different chips are nearly identical, only the results from the HDSQ18b 4A05 Type I multiplexer chip from measurements in the cryostat at mK-temperatures are discussed in more detail.

Prior to operating the FRM chip at higher frequencies, they are characterized using only the SQUID electronics, as described in section 4.5. With the new experimental setup is it possible to characterize every single dc-SQUID in the multiplexer array within a single cool down process. While characterizing the SQUIDs in the multiplexer arrays we obtain the same results within the margin of uncertainty, as from the above discussed results from the single SQUID measurements. When all SQUIDs receive an input signal the single voltage responses of the SQUIDs in the array add up. For the readout of the multiplexer we can adjust each SQUID response frequency individually with a combination of the flux ramp generator output current and the interchangeable attenuators for each flux ramp line. In Fig. 5.5 a) the time trace of

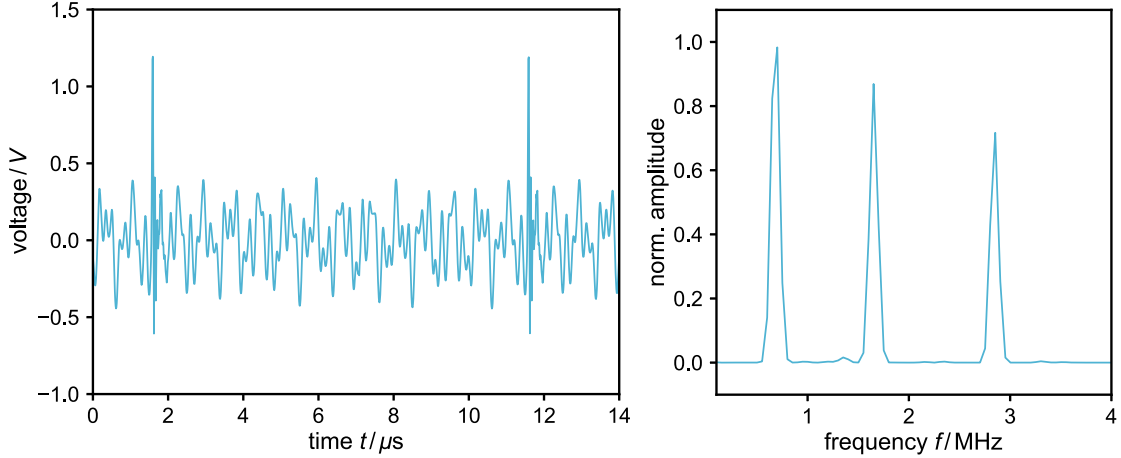


**Figure 5.5:** a) Voltage time trace of the HDSQ18b 4A05 Type I multiplexer chip at mK-temperatures with three applied flux ramp sawtooth shaped flux ramp signals with input frequency of 100 kHz b) Fourier transformation of the time trace.

the multiplexer response is shown connecting three flux ramps to one multiplexer array whereby the output peak to peak voltage of the HP 33120A generator is set to 200 mV of a 100 kHz sawtooth shape signal and with attenuators of 12 dB, 6 dB and 3 dB respectively. This of course is not a practical choice of attenuators for a practical readout due to fact that the first harmonics of the response frequencies overlap as they are multiple of each other. In the time trace the sharp ramp resets can be readily identified together with a ringing effect, which have to be discarded prior to Fourier transforming the signal time trace. The results of the Fourier transformation are shown in Fig. 5.5 b). There are three clearly distinguishable peaks corresponding to the SQUID response frequencies. The shown time trace was captured with a Keysight oscilloscope and the signal was Fourier transformed using a standard fast Fourier transform algorithm with a Blackman-Harris window function.

In order to readout an input signal with the multiplexer a SIS3316-DT ADC, which has a sample rate of 100 MHz, was used to continuously save the time trace data. Afterwards this data was Fourier transformed and the phase of each carrier frequency was extracted and with (2.42) converted to the magnetic flux input. As the sample rate of the ADC is small for our purposes a sawtooth shaped ramp frequency signal of 40 kHz was applied, from which 512 data points for each ramp segment have been used when Fourier transforming the signal discarding some points at the beginning and the end of the time trace to reduce the effects of the sharp ramp resets on our phase data. In Fig. 5.6 two simultaneously read out test input signals are shown where the magnetic flux is applied against time. Here the SQUID response frequencies were chosen to  $f_1 = 1.15$  MHz and  $f_2 = 2.6$  MHz. In Fig. 5.6 two simultaneously read out

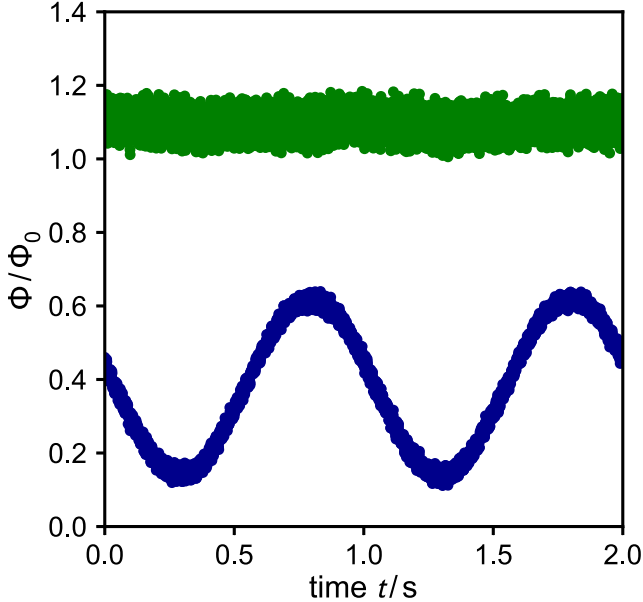


**Figure 5.6:** Multiplexed simultaneous readout of two input signals where the magnetic flux is determined by the phase of the carrier frequency of corresponding SQUID. One SQUID has a sine shaped signal applied with a  $f = 1 \text{ Hz}$  and a total flux input of approximately  $\Phi = 0.5 \Phi_0$  while the second SQUID has no input signal applied to it. To increase the visibility the signals were shifted by an arbitrary flux offset.

test input signals are shown. Here a sine shaped test input signal was provided by the SQUID electronics with a current of  $I = 3 \mu\text{A}$  corresponding to a flux input of roughly  $\Phi = 0.5 \Phi_0$  and a frequency of  $f = 1 \text{ Hz}$  for one SQUID, whereas the second SQUID had no input applied. To increase the visibility the signals were shifted by an arbitrary flux offset. It is eminent that the input signals are reconstructed successfully. The accuracy of the phase determination can be inferred from the scattering of the data points of the signal with where no input is applied. Calculating the standard deviation we obtain an error of  $\Phi_{\text{err}} = 0.06 \Phi_0$ . This does not change significantly for the readout of a higher frequency input signal. The uncertainty resulting from the scattering from the phase determination can be explained by the deterioration of the SQUID signal shape, stemming from different sources. The first is the added noise due to the room temperature amplifiers in combination with their current supply. Second the additional noise coupled into the readout line from external electromagnetic disturbances, especially at the adapter box, which has many unshielded cables. Most prominently deteriorating the signal shape is a pulse like signal in the order of  $f = 10 \text{ kHz}$ . In addition it was found that the position of the coaxial cables can change the signal and noise amplitude. Further the three wire measurement ends at the coaxial cables connecting the amplifiers to the adapter box, which further degrades the signal quality. Also one has to consider external flux coupling into the SQUIDs itself, which have only a provisional shielding of either superconducting lead in the cryostat in our instance. Further the flux ramp modulation signal is effected by the generator noise, the slight signal deterioration due to the twisted wires and the on chip transmission line configuration. As the FRM signal couples directly into the

SQUID, a stark degradation can lead to further loss in signal quality. On top a much higher number of samples in the signal time trace, in order to obtain a more accurate discrete Fourier transform.

## 6. Conclusion and Outlook

The ever-growing demand for improving the efficiency and energy resolution of the metallic magnetic calorimeters naturally leads to an increase in system size and complexity. In order to reduce the complexity of the cryogenic SQUID readout systems, multiplexing techniques can be utilized, allowing multiple SQUIDs to be read out through a single line. However, many existing multiplexing techniques require demanding and expensive electronics making the operation of medium-scale detector arrays challenging. Therefore, our research group developed a low-cost flux ramp modulation dc-SQUID multiplexing technique operating at MHz frequencies. In the framework of this thesis this multiplexing method was further developed to read out a  $16 \times 16$  MMC array at cryogenic temperatures. This includes the design and fabrication of new dc-SQUID FRM multiplexer chips containing two times four dc-SQUIDs in serial connection. These chips are tailored to specifically fit the  $16 \times 16$  maXs20-256-16 MMC array [Abe25] and its newly developed dedicated readout scheme. Compared to our previous FRM dc-SQUID multiplexer designs [Hoi21], the on-chip modulation coil configuration was changed in favor of a more flexible approach, where each SQUID in the serial array is provided with its own individual flux ramp, adding an additional degree of freedom in the operation.

The SQUID wafer produced within this thesis contains the first window-type Josephson junction from our PreVAC sputtering system. Therefore, un-shunted single junctions of this type were investigated, confirming their high quality and on top showcasing that the targeted critical current was reached. Furthermore the fabricated single dc-SQUIDs were fully characterized and their noise behavior at mK-temperatures was investigated. The white noise level versus the cryostat temperature was measured using a cross-correlation method to compare the performance of dc-SQUIDs with Au and AuPd cooling fins. As suggested by the thermal model no significant difference in performance was found, because the thermal bottleneck in our current design is most likely attributed to the thermal link between the cooling fin and shunt resistor. This is also supported by the data, which hints at a metallic thermal bottleneck. These investigations of the white noise were done with the intend to further optimize the noise performance of the single dc-SQUIDs, which are also used for the FRM multiplexer design. By significantly lowering the operational temperature, the performance of the multiplexer could also be improved substantially. For future improvements on the passive cooling structures, the thermal link could be placed in the middle of the resistor, in addition to increasing its cross-section area.

To test the single multiplexer chips, a dedicated setup was built. Hereby all signals are transmitted with twisted pair CuNi wires to the experiment. This setup can be used either in a liquid helium dewar where the experiment is mounted on a dipstick or in one of our  $^3\text{He}/^4\text{He}$  dilution refrigerator. Utilizing a simple room temperature electronics setup consisting of a low-budget state-of-the-art noise performance amplifier chain, function generator and analog-to-digital converter, the functionality of the new chips was successfully demonstrated. For the operation with the MMC we intend to readout the setup based on a programmable field arrays (FPGA) described in [Wol20]. The results from the demonstration of functionality are not directly comparable to our previous designs presented in [Hoi21], because the readout accuracy heavily depends on the involved electronics. However, we still find that the chips perform well up to a sampling frequency of 100 kHz.

For the detector readout, a separate dedicated setup was conceptualized and partially fabricated. in this setup, all 128 individual channels of the MMC array are read out only through a total of 36 SQUID signal transmission lines. This represents a substantial reduction in the number of wires compared to a single-stage readout with a flux-locked-loop method, reducing it by 220. Furthermore, compared to a two-stage flux-locked-loop readout, the number of wires is reduced by 476. This reduction in wiring simplifies the overall system complexity in the cryogenic environment and significantly decreases the total heat load stemming from the resistive cables into the cryostat. Utilizing the flexible chip design, the same 4 flux ramp modulation signals can be shared by 32 serial arrays, which we call a two dimensional  $4 \times 32$  multiplexer.

Future work includes the testing of the new FRM chips together with the FPGA board readout electronics to characterize the performance of the multiplexer setup. Further the next steps should involve testing of the two dimensional  $4 \times 32$  multiplexer array for the detector readout. Within the framework of this thesis, enough dc-SQUID FRM multiplexer chips have been fabricated for a potential initial run of the full configuration. Other challenges for the future operation of the detector, are the expected data stream, providing a substantial challenge when operating the detector in continuous read out mode over a long period of time. The successful implementation of the full  $4 \times 32$  low-budget multiplexer will provide high efficiency, a significant reduction of the cryogenic system complexity and grants the possibility of a continuous simultaneous readout with an adequate energy resolution.

Overall within this thesis, important advancements towards the full detector readout with a FRM dc-SQUID multiplexer have been realized including the development of the corresponding cryogenic readout scheme and the successful demonstration of the new multiplexer chips.

## Bibliography

- [Abe25] Andreas Abeln, *To be published: Developement of a 16x16 pixel MMC based high resolution X-ray detector system with multiplexed read-out based on flux ramp modulated dc SQUIDs*, Dissertation, Kirchhoff-Institut für Physik, Universität Heidelberg, 2025.
- [Ahr22] Felix Klaus Ahrens, *Cryogenic read-out system and resonator optimisation for the microwave SQUID multiplexer within the ECHo experiment*, Dissertation, Kirchhoff-Institut für Physik, Universität Heidelberg, 2022.
- [Ale03] Alexandre S Alexandrov, *Theory of superconductivity: from weak to strong coupling*, CRC Press, 2003.
- [All17] Steffen Allgeier, *Entwicklung einer modularen 36-Kanal-Auslesekette mit rauscharmen SQUID-basierten Vorverstärkern für die 4k-Pixel-Molekulkamera MOCCA*, Diplomarbeit, Kirchhoff-Institut für Physik, Universität Heidelberg, 2017.
- [Ann04] James F Annett, *Superconductivity, superfluids and condensates*, Volumen 5, Oxford University Press, 2004.
- [Bar57] J. Bardeen, L. N. Cooper, and J. R. Schrieffer, Theory of Superconductivity, *Phys. Rev.*, **108**(5), 1175–1204, 1957.
- [Bau22] Fabienne Bauer, *Rauscharme Stromsensor-dc-SQUIDs mit Impedanzanpassung für metallische magnetische Kalorimeter*, Dissertation, Kirchhoff-Institut für Physik, Universität Heidelberg, 2022.
- [Bog58] N. N. Bogoljubov, V. V. Tolmachov, and D. V. Širkov, A new method in the theory of superconductivity, *Fortschritte der Physik*, **6**(11-12), 605–682, 1958.
- [Bru82] J. J. P. Bruines, V. J. de Waal, and J. E. Mooij, Comment on: “DC SQUID: Noise and optimization” by Tesche and Clarke, *J. Low Temp. Phys.*, **46**, 383–386, 1982.
- [Cla04] J. Clarke and A. I. Braginski (Ed.), *The SQUID Handbook: Vol. I Fundamentals and Technology of SQUIDs and SQUID Systems*, Wiley-VCH, 2004.

- [Coo72] Leon N Cooper, Microscopic quantum interference effects in the theory of superconductivity, *Nobel Lect*, **11**, 73–93, 1972.
- [DG18] Pierre-Gilles De Gennes, *Superconductivity of metals and alloys*, CRC press, 2018.
- [Enp85] K Enpuku, K Sueoka, K Yoshida, and F Irie, Effect of damping resistance on voltage versus flux relation of a dc squid with large inductance and critical current, *Journal of applied physics*, **57**(5), 1691–1697, 1985.
- [Enp91] K. Enpuku and K. Yoshida, Modeling the dc superconducting quantum interference device coupled to the multturn input coil, *J. Appl. Phys.*, **69**(10), 7295–7300, 1991.
- [Enp92a] K. Enpuku, R. Cantor, and H. Koch, Modeling the dc superconducting quantum interference device coupled to the multturn input coil. III, *J. Appl. Phys.*, **72**(3), 1000–1006, 1992.
- [Enp92b] K. Enpuku, R. Cantor, and H. Koch, Modeling the direct current superconducting quantum interference device coupled to the multturn input coil. II, *J. Appl. Phys.*, **71**(5), 2338–2346, 1992.
- [Ens05] C. Enss and S. Hunklinger, *Low-temperature physics*, Springer-Verlag Berlin Heidelberg New York, 2005.
- [Fey64] R. P. Feynman, R. B. Leighton, and M. Sands, *The Feynman Lectures on Physics*, Addison-Wesley, 1964.
- [Fin66] DK Finnemore, TF Stromberg, and CA Swenson, Superconducting properties of high-purity niobium, *Physical Review*, **149**(1), 231, 1966.
- [Fle05] A. Fleischmann, C. Enss, and G. M. Seidel, *Cryogenic Particle Detection*, Volumen 99 in *Topics in applied physics*, Kapitel Metallic Magnetic Calorimeters, 151–216, Springer-Verlag Berlin Heidelberg, 2005.
- [Fou11] Coenrad J Fourie, Olaf Wetzstein, Thomas Ortlepp, and Jürgen Kunert, Three-dimensional multi-terminal superconductive integrated circuit inductance extraction, *Superconductor Science and Technology*, **24**(12), 125015, 2011.
- [Fri44] Harald T Friis, Noise figures of radio receivers, *Proceedings of the IRE*, **32**(7), 419–422, 1944.
- [FS24] Anna Ferring-Siebert, *Untersuchung des niederfrequenten Flussrauschens in dc-SQUIDs bei Temperaturen unter 1K*, Dissertation, Kirchhoff-Institut für Physik, Universität Heidelberg, 2024.

- [Geh23] T. Gehlhaar, *Characterization of the Properties of Cross-Type Nb/Al-AlO<sub>x</sub>/Nb Josephson Tunnel Junctions*, Bachelor's thesis, Kirchhoff-Institut für Physik, Universität Heidelberg, 2023.
- [Ger01] ME Gershenson, D Gong, T Sato, BS Karasik, and AV Sergeev, Millisecond electron–phonon relaxation in ultrathin disordered metal films at millikelvin temperatures, *Applied Physics Letters*, **79**(13), 2049–2051, 2001.
- [Gia06] Francesco Giazotto, Tero T Heikkilä, Arttu Luukanen, Alexander M Savin, and Jukka P Pekola, Opportunities for mesoscopics in thermometry and refrigeration: Physics and applications, *Reviews of Modern Physics*, **78**(1), 217, 2006.
- [Gin50] V. L. Ginzburg and L. Landau, On the theory of superconductivity, *Zh. Èksper. Teoret. Fiz.*, **20**, 1064–1082, 1950.
- [Goo71] William L Goodman, Wayne D Willis, Daniel A Vincent, and Bascom S Deaver Jr, Quantized flux states of superconducting cylinders, *Physical Review B*, **4**(5), 1530, 1971.
- [Gor58] LP Gor'Kov, On the energy spectrum of superconductors, *Sov. Phys. JETP*, **7**(505), 158, 1958.
- [Gub05] AI Gubin, KS Il'in, SA Vitusevich, M Siegel, and N Klein, Dependence of magnetic penetration depth on the thickness of superconducting nb thin films, *Physical Review B*, **72**(6), 064503, 2005.
- [Hoi21] Ludwig Hoibl, *Frequency-division dc-SQUID Multiplexing based on flux ramp modulation*, Diplomarbeit, Kirchhoff-Institut für Physik, Universität Heidelberg, 2021.
- [Irw06] Kent D Irwin, James A Beall, W Bertrand Doriese, WD Duncan, Gene C Hilton, JAB Mates, Carl D Reintsema, DR Schmidt, JN Ullom, Leila R Vale, et al., Microwave squid multiplexers for low-temperature detectors, *Nuclear Instruments and Methods in Physics Research Section A: Accelerators, Spectrometers, Detectors and Associated Equipment*, **559**(2), 802–804, 2006.
- [Joh28] J. B. Johnson, Thermal Agitation of Electricity in Conductors, *Phys. Rev.*, **32**(1), 97–109, 1928.
- [Jos62] B.D. Josephson, Possible new effects in superconductive tunnelling, *Physics Letters*, **1**(7), 251–253, 1962.

- [Jos64] B.D. Josephson, Coupled superconductors, *Rev. Mod. Phys.*, **36**, 216–220, 1964.
- [Jos74] BRIAN D Josephson, The discovery of tunnelling supercurrents, *Reviews of Modern Physics*, **46**(2), 251, 1974.
- [Kah24] Nicolas Robert Kahne, *Design, Fabrication and Characterization of Inductance-Matched Current Sensing dc-SQUIDs for Metallic Magnetic Calorimeter Readout*, Diplomarbeit, Kirchhoff-Institut für Physik, Universität Heidelberg, 2024.
- [Kai04] Kenneth L Kaiser, *Electromagnetic compatibility handbook*, CRC press, 2004.
- [Kem12] S. Kempf, *Entwicklung eines Mikrowellen-SQUID-Multiplexers auf der Grundlage nicht-hysteretischer rf-SQUIDs zur Auslesung metallischer magnetischer Kalorimeter*, Dissertation, Kirchhoff-Institut für Physik, Universität Heidelberg, 2012.
- [Kem13] S Kempf, A Ferring, A Fleischmann, L Gastaldo, and C Enss, Characterization of the reliability and uniformity of an anodization-free fabrication process for high-quality nb/al-alox/nb josephson junctions, *Superconductor Science and Technology*, **26**(6), 065012, 2013.
- [Kem15] S. Kempf, A. Ferring, A. Fleischmann, and C. Enss, Direct-current superconducting quantum interference devices for the readout of metallic magnetic calorimeters, *Supercond. Sci. Tech.*, **28**(4), 045008, 2015.
- [Kem16] Sebastian Kempf, Anna Ferring, and Christian Enss, Towards noise engineering: Recent insights in low-frequency excess flux noise of superconducting quantum devices, *Applied Physics Letters*, **109**(16), 2016.
- [Knu88] Jukka Knuutila, Matti Kajola, Heikki Seppä, Risto Mutikainen, and Jorma Salmi, Design, optimization, and construction of a dc squid with complete flux transformer circuits, *Journal of low temperature physics*, **71**, 369–392, 1988.
- [Kum93] GS Kumar, G Prasad, and RO Pohl, Experimental determinations of the lorenz number, *Journal of materials science*, **28**, 4261–4272, 1993.
- [Lan14] T Lanting, MH Amin, AJ Berkley, C Rich, S-F Chen, S LaForest, and Rogério de Sousa, Evidence for temperature-dependent spin diffusion as a mechanism of intrinsic flux noise in squids, *Physical Review B*, **89**(1), 014503, 2014.

- [Lik86] K. K. Likharev, *Dynamics of Josephson Junctions and Circuits*, Gordon and Breach, New York, 1986.
- [Lit59] WA Little, The transport of heat between dissimilar solids at low temperatures, *Canadian Journal of Physics*, **37**(3), 334–349, 1959.
- [Mat08] JAB Mates, Gene C Hilton, Kent D Irwin, Leila R Vale, and KW Lehnert, Demonstration of a multiplexer of dissipationless superconducting quantum interference devices, *Applied Physics Letters*, **92**(2), 2008.
- [Mat12] John AB Mates, KD Irwin, LR Vale, GC Hilton, J Gao, and KW Lehnert, Flux-ramp modulation for squid multiplexing, *Journal of Low Temperature Physics*, **167**, 707–712, 2012.
- [McM68] W. L. McMillan, Tunneling Model of the Superconducting Proximity Effect, *Phys. Rev.*, **175**, 537–542, 1968.
- [Mei33] W. Meissner and R. Ochsenfeld, Ein neuer Effekt bei Eintritt der Supraleitfähigkeit, *Naturwissenschaften*, **21**(44), 787–788, 1933.
- [Mot93] Curtis D Motchenbacher, Joseph Alvin Connelly, et al., *Low-noise electronic system design*, Volumen 269, Wiley New York, 1993.
- [Mul01] Jochen Muller, Stefan Weiss, Rudolf Gross, Reinhold Kleiner, and Dieter Koelle, Voltage-flux-characteristics of asymmetric dc squids, *IEEE transactions on applied superconductivity*, **11**(1), 912–915, 2001.
- [Nag95] KE Nagaev, Influence of electron-electron scattering on shot noise in diffusive contacts, *Physical Review B*, **52**(7), 4740, 1995.
- [Nyq28] H. Nyquist, Thermal Agitation of Electric Charge in Conductors, *Phys. Rev.*, **32**(1), 110–113, 1928.
- [Pen60] Roger Penrose, A spinor approach to general relativity, *Annals of Physics*, **10**(2), 171–201, 1960.
- [Ple06] J Pleikies, KH Kuit, J Flokstra, M Podt, L Gottardi, A de Waard, O Usenko, and G Frossati, Squid developments for high accuracy current measurements in the khz frequency range, in *7th International Workshop on Low Temperature Electronics, WOLTE 2006*, 159–164, Citeseer, 2006.
- [Pol69] Gerald L Pollack, Kapitza resistance, *Reviews of modern physics*, **41**(1), 48, 1969.
- [Poo95] Charles P. Poole, Jr., Horacia A. Farach, and Richard J. Creswick, *Superconductivity*, Academic Press San Diego New York, 1995.

- [Ric21a] Daniel Richter, Ludwig Hoibl, Thomas Wolber, Nick Karcher, Andreas Fleischmann, Christian Enss, Marc Weber, Oliver Sander, and Sebastian Kempf, Flux ramp modulation based mhz frequency-division dc-squid multiplexer, *Applied Physics Letters*, **118**(12), 2021.
- [Ric21b] Daniel Phil Richter, *Multikanal-Auslesung von metallischen magnetischen Kalorimetern mittels eines vollständigen Mikrowellen-SQUID-Multiplexer-Systems*, Dissertation, Kirchhoff-Institut für Physik, Universität Heidelberg, 2021.
- [Rob76] Benjamin Washington Roberts, Survey of superconductive materials and critical evaluation of selected properties, *Journal of Physical and Chemical Reference Data*, **5**(3), 581–822, 1976.
- [Rub10] Enrico Rubiola and François Vernotte, The cross-spectrum experimental method, *arXiv preprint arXiv:1003.0113*, 2010.
- [Sav06] AM Savin, Jukka P Pekola, DV Averin, and VK Semenov, Thermal budget of superconducting digital circuits at subkelvin temperatures, *Journal of applied physics*, **99**(8), 2006.
- [Som27] Arnold Sommerfeld, Zur elektronentheorie der metalle, *Naturwissenschaften*, **15**(41), 825–832, 1927.
- [Ste96] Andrew H Steinbach, John M Martinis, and Michel H Devoret, Observation of hot-electron shot noise in a metallic resistor, *Physical review letters*, **76**(20), 3806, 1996.
- [Sto23] Alexander Stoll, *Optimisation of Nb/Al-AlO/Nb Tri-Layer Deposition for Cross-Type Josephson Junction Fabrication in the PreVAC Sputtering System*, Diplomarbeit, Kirchhoff-Institut für Physik, Universität Heidelberg, 2023.
- [Tar99] EJ Tarte, DJ Kang, WE Booij, PD Coleman, A Moya, F Baudenbacher, SH Moon, and MG Blamire, Improvement of high t<sub>sub</sub> c/squid performance using an integrated resistor, *IEEE transactions on applied superconductivity*, **9**(2), 4432–4435, 1999.
- [Tes77] C. Tesche and J. Clarke, dc SQUID: Noise and Optimization, *J. Low Temp. Phys.*, **29**, 301–331, 1977.
- [Ueh93] G. Uehara, N. Matsuda, K. Kazami, Y. Takada, and H. Kado, Asymmetric Bias Injection Technique for Drung-Type Superconducting Quantum Interference Devices, *Jpn. J. Appl. Phys.*, **32**(12A), L1735, 1993.

- [Weg18] Mathias Wegner, *Entwicklung, Herstellung und Charakterisierung eines auf metallischen magnetischen Kalorimetern basierenden Detektorarrays mit 64 Pixeln und integriertem Mikrowellen-SQUID-Multiplexer*, Dissertation, Kirchhoff-Institut für Physik, Universität Heidelberg, 2018.
- [Wei69] M Weihnacht, Influence of film thickness on dc josephson current, *physica status solidi (b)*, **32**(2), K169–K172, 1969.
- [Wei71] Stephen Weinstein and Paul Ebert, Data transmission by frequency-division multiplexing using the discrete fourier transform, *IEEE transactions on Communication Technology*, **19**(5), 628–634, 1971.
- [Wel87] F. C. Wellstood, C. Urbina, and J. Clarke, Lowfrequency noise in dc superconducting quantum interference devices below 1 K, *Appl. Phys. Lett.*, **50**(12), 772–774, 1987.
- [Wel94] F. C. Wellstood, C. Urbina, and John Clarke, Hot-electron effects in metals, *Phys. Rev. B*, **49**, 5942–5955, 1994.
- [Wol20] Thomas Wolber, *Auslese von metallischen magnetischen Kalorimetern mittels Flussrampenmultiplex*, Diplomarbeit, IPE, Universität Karlsruhe, 2020.
- [Wu12] Jiansheng Wu and C Yu Clare, Modeling flux noise in squids due to hyperfine interactions, *Physical Review Letters*, **108**(24), 247001, 2012.



Ich versichere, dass ich diese Arbeit selbstständig verfasst und keine anderen als die angegebenen Quellen und Hilfsmittel benutzt habe.

Heidelberg, den 17. Februar 2024

.....  
(David Mazibrada)